IMPLICATIONS OF ATMOSPHERIC NEUTRINO DATA

By

Jesus Escamilla Roa

Dissertation

Submitted to the Faculty of the

Graduate School of Vanderbilt University

in partial fulfillment of the requirements

for the degree of

DOCTOR OF PHILOSOPHY

in

Physics

December, 2008

Nashville, Tennessee

Approved by:

Prof. David J. Ernst

Prof. Thomas J. Weiler

Prof. Thomas W. Kephart

Prof. Paul Sheldon

Prof. Sait Umar

To all my Family...

In particular I dedicate this work to the person that deserves the credit for all the good thing happening in my life, Mother all this has been done with your inspiration and love, to my sisters Tina, Liz, Lupita and my dear niece Marisol for their support and encouragement, to my son Hever and my two little babies Eliza and Milagros for all the joy and happiness that you have brought to my life.

A mi familia...

Quiero dedicar este trabajo a la única persona que merece todo el crédito por todos los logros de mi vida, Amada Madre Mía, este trabajo ha sido logrado con tu inspiración, bendiciones y amor, por esto te quedo eternamente agradecido. A mis queridas hermanas: Tina, Liz, Lupita y a mi querida sobrina Marisol, por su amor, apoyo y comprención. Y finalmente a mi hijo Hever y mis dos pequeñas bebes Eliza y Milagros por toda la alegría y felicidad que han traído a mi vida.

Jesus E. Roa

ACKNOWLEDGMENTS

I would like to thank to all people that have contributed somehow to this work, first of all to my advisor Dr. David Ernst for all the support and patience during the last 5 years, to my friend and former advisor Dr. Jorge Lopez whose help made this work possible, and my fried Dr. David Latimer for his contributions to this work. I would also like to thank Dr. Thomas Weiler for helping me to get this manuscript finished, and Professor Sait Umar for his help to solve all my computer problems.

TABLE OF CONTENTS

LIST OF TABLES

Table Page

LIST OF FIGURES

CHAPTER I

INTRODUCTION
HISTORY AND CURRENT STATUS OF NEUTRINO OSCILLATION

1.1 The Genesis of the Neutrino

Unlike the discovery of most of the elementary particles, neutrinos were postulated first and years later discovered. In 1914 when Chadwick discovered the continuous energy spectrum of beta rays, he immediately notes discrepancies between the observation and the theoretical interpretations. Was the continuous spectrum directly due to the primary electrons emitted from the radioactive nucleus or was it to be attributed to secondary processes? The first hypothesis, which proved to be the correct one, was advocated by C. D. Ellis [1], the second one by L. Meitner [2]. Meitner appealed to the fact that nuclei possess discrete energy states, as was known from alpha and gamma rays. She focused attention on the discrete energies of electrons, which had also been observed for many beta-radioactive nuclei. Ellis interpreted the observation to electrons being ejected from the outer shells by inner conversion of monochromatic nuclear gamma rays and assigned them to the observed X-ray lines. According to Meitner's theory, however, at least one of the electrons of discrete energy should be a genuine primary electron from the nucleus, which, in a secondary process, could then emit from the outer shells more electrons with smaller energies. However, this postulated primary electron of discrete energy was never detected. Moreover, there are beta-radioactive nuclei, that do not emit gamma rays and for which the electrons with discrete energies were missing altogether.

To explain this missing energy there seemed to be two possibilities: either a non-conservation of energy or an additional undetectable new particle was being emitted. On December 4 1930 in a famous letter, W. Pauli wrote:
Dear Radioactive Ladies and Gentlemen,
As the bearer of these lines, to whom I graciously ask you to listen, will explain to you in

more detail, how because of the wrong statistics of the N and ^{6}Li nuclei and the continuous beta spectrum, I have hit upon a desperate remedy to save the exchange theorem of statistics and the law of conservation of energy. Namely, the possibility that there could exist in the nuclei electrically neutral particles, that I wish to call neutrons , which have spin 1/2 and obey the exclusion principle and which further differ from light quanta in that they do not travel with the velocity of light. The mass of the neutrons should be of the same order of magnitude as the electron mass and in any event not larger than 0.01 proton masses. The continuous beta spectrum would then become understandable by the assumption that in beta decay a neutron is emitted in addition to the electron such that the sum of the energies of the neutron and the electron is constant... I agree that my remedy could seem incredible because one should have seen those neutrons very earlier if they really exist. But only the one who dare can win and the difficult situation, due to the continuous structure of the beta spectrum, is lighted by a remark of my honored predecessor, Mr Debye, who told me recently in Brussels: Oh, Its well better not to think to this at all, like new taxes. From now on, every solution to the issue must be discussed. Thus, dear radioactive people, look and judge. Unfortunately, I cannot appear in Tubingen personally since I am indispensable here in Zurich because of a ball on the night of 6/7 December. With my best regards to you, and also to Mr Back. Your humble servant. W. Pauli

In summary, his solution to the problem: a new spin 1/2 particle produced together with the electrons and or positron but undetectable. This explains the continuous spectrum; the positron and the neutrino share energy in a way that the sum of both corresponds to the total transition energy. A few years later the neutron was discovered. This led E. Fermi to develop a phenomenological theory of β decay [3], he would name Pauli's particle the NEUTRINO meaning little neutral object. About 20 years later, in 1953 the discovery of this undetectable particle occurred, at the Hanford reactor. Cowan and Reines [4] using a water tank surrounded by two liquid scintillators, detected a rather small signal. In 1956 the same experiment was repeated at the Savannah River reactor, finally providing sufficient evidence to clearly demonstrate the existence of neutrinos.

Years after the discovery of the electron neutrino, in 1959, Bruno Pontecorvo postulated the existence of muon neutrinos (ν_μ) different from the neutrinos emitted in the β-decay of nuclei (ν_e). Leon Lederman, Jack Steinberger and Melvin Schwartz [5] discovered muon neutrinos in 1962 by detecting muons from:

$$\nu_\mu + N \rightarrow \mu^- + X.$$

Their discovery was awarded the Nobel Prize in 1988. A third family of neutrinos was predicted when the tau lepton (τ) was discovered in 1975 [6]. This implied the existence of the tau neutrino (ν_τ). The discovery of the tau neutrino occurred at Fermi National Accelerator Laboratory in 2000 [7]. The discovery of the neutrinos from outer space followed the prediction of the three generations of neutrinos. In 1968, the neutrinos from the Sun were observed by Ray Davis and his collaboration [8]. Neutrinos from the supernova explosion SN1987a were observed by the Kamiokande [9, 10], IMB [11, 12] and Baksan [13] experiments in 1987. Raymond Davis Jr. and Masatoshi Koshiba were awarded the Nobel Prize in 2002 for their discovery of extra terrestrial neutrinos.

1.1.1 Some Neutrino Properties

The neutrino is now known to be one of the fundamental particles belonging to the lepton family. It has quantum spin number 1/2, negligible mass compared to the other elementary particles, hence negligible gravitational interactions, no electromagnetic charge, hence no Coulomb interactions, nor does it have any baryonic charge, hence no strong interactions. It couples with other particles only via the weak interaction. There are three known types, or flavors, of neutrinos that are each associated with a corresponding member of the lepton family: an electron neutrino, a muon neutrino, and a tau neutrino, each one having its own antiparticle. As a lepton, it has a particular lepton number that is conserved in weak interactions. Electrons (positrons) and electron (anti)neutrinos have electron flavor number $L_e = +1(-1)$. For all other leptons $L_e = 0$. Muons and taus and their neutrino counterparts have similar values for L_μ and L_τ . In addition to the lepton number conservation, experiments also demonstrate flavor conservation, a property that is built into the standard model of the electroweak interaction.

A very important property of the neutrino that has only recently been discovered is their mass. We now know neutrinos are massive particles. Of the three types of neutrinos, physicists now believe that at least two have non-zero masses, though there are still open questions to be answered regarding exactly what is the value of their mass. β-decay experiments that observe the distortion of the energy spectrum due to having a non-zero neutrino mass limit the electron neutrino mass to be less than 2.8 eV/c^2 [14]. Other decay-type experiments constrain the mass of a muon neutrino to less than 170 keV/c^2 [15] and the mass of the tau neutrino to be less than 15.5 MeV/c^2 [16] . Cosmological results also put a limit on the sum of the three neutrino masses. The effect of massive neutrinos on structure formation only applies to the scales below the free-streaming length. For neutrinos with masses of several eV the free-streaming scale is smaller than the scales which can be probed using present CMB data and therefore there is no observable suppression. On the other hand, neutrinos of sub-eV mass behave almost like a relativistic neutrino species for CMB considerations. The main effect of a small neutrino mass on the CMB is that it leads to an enhanced early ISW effect. The reason is that the ratio of radiation to matter at recombination becomes larger because a sub-eV neutrino is still relativistic or semi-relativistic at recombination. The Wilkinson Microwave Anisotropy Probe limits the sum of the masses at 95% CL. to $m_\nu < 0.42$ eV [17] .

1.1.2 Where do neutrinos come from?

On average, about ten trillion neutrinos per second pass through a cubic centimeter on Earth, These come from a number of different sources [18]. Local sources include nuclear accelerators that produce neutrinos for physics experiments. Nuclear reactors are another terrestrial source of neutrinos which are a product of the fission process. Some reactors produce over 10^{20} neutrinos per second. Nuclear bombs also produce neutrinos and were once considered for a detector experiment (but were never used as a source). At the surface of the Earth there is a flux of $6 \times 10^6 \mathrm{cm}^{-2}\mathrm{s}^{-1}$ geological neutrinos from natural radioactive sources, mainly ^{238}U and ^{232}Th decay chains [19]. Within the galaxy, a star (like the sun) produces a large number ($6.5 \times 10^{14} \mathrm{m}^{-2}\mathrm{s}^{-1}$) of neutrinos in fusion processes. The universe is believe to have relic neutrinos left over from the formation of the universe just after the

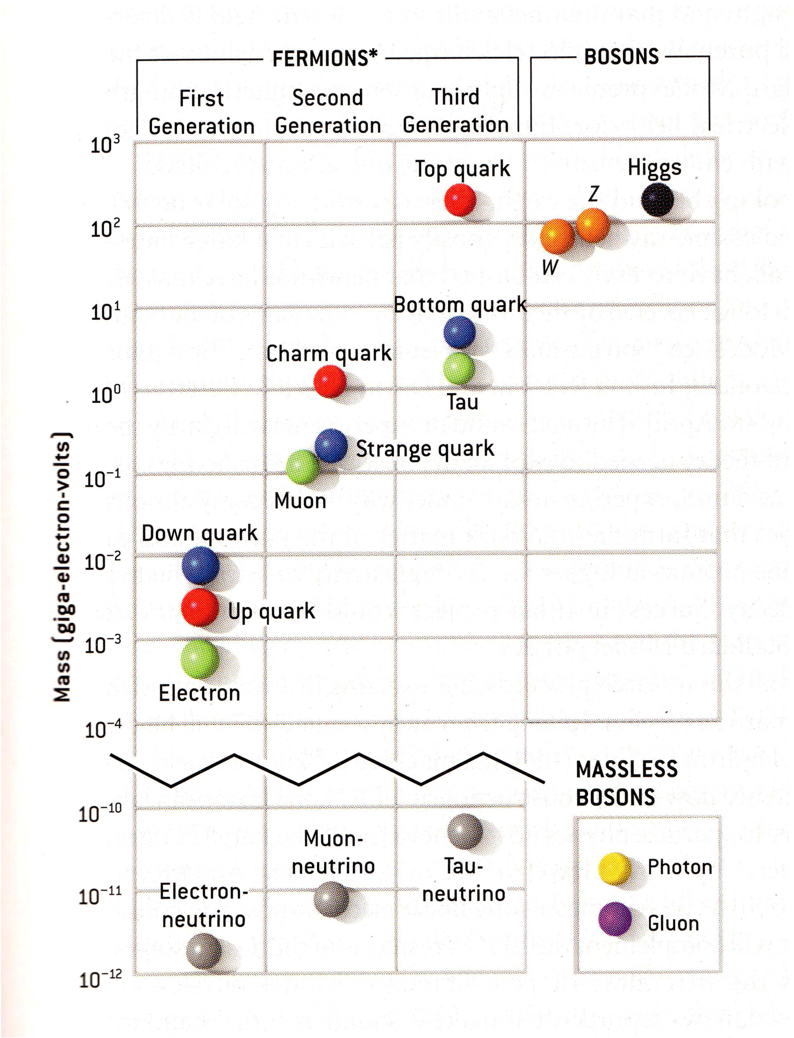

Figure 1: Elementary particles in the Standard model.

Big Bang.

1.2 Neutrino Properties and the Standard Model

Elementary particles are classified in two groups: fermions and bosons. Among fermions, we find quarks and leptons, which exist in different generations or flavors. Bosons act as mediators for the strong, electromagnetic, and weak interactions. Figure 1 shows a schematic view of the elementary particles in the Standard model. Neutrinos, as part of the fermion family, come in three flavors : ν_e, ν_μ and ν_τ and are paired with their corresponding charged

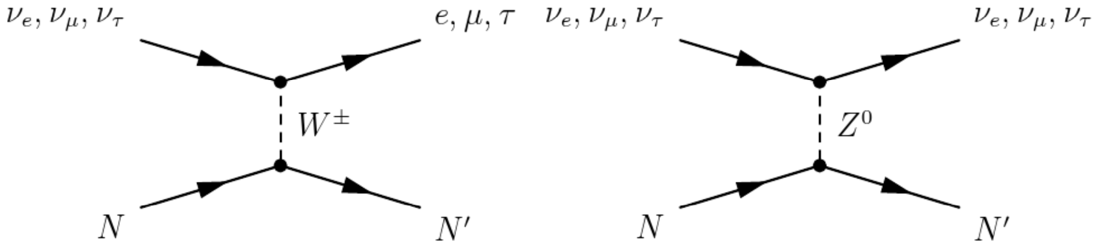

Figure 2: Feymam diagrams for weak interactions.

lepton, the electron, the muon, and the tau. Experiments measuring the decay of the Z boson [20] indicated the existence of three light neutrino flavors. Neutrinos are electrically neutral and colorless, no electric or magnetic dipole moments have yet been measured. This is important in astrophysics because neutrinos then travel in straight lines from the point of origin without bending by galactic magnetic fields. They interact only through the weak force. The weak interaction can occur in two different ways: charged current (CC) and neutral current (NC) interactions. The force mediators for CC and NC interactions are the charged W± and neutral Z bosons, respectively. Figure 2 shows example Feynman diagrams for the CC and NC interactions.

Neutrinos are spin half particles which may be described by a four component wave function $\Psi(x)$ which obeys the Dirac equation. The components of $\Psi(x)$ correspond to the two possible spin projections or two different helicities. Experimentally only left-handed neutrinos and right-handed anti neutrinos have been observed. In the theory of weak interactions, the weak force only couples to negative helicity (left-handed) neutrinos and positive helicity (right-handed) anti-neutrinos. The weak interaction was unified with the electromagnetic interaction into the minimal standard model by Weinberg, Glashow [21] and Salam [22]. Analogous to QED's exchange of photons, the weak interaction is mediated by the exchange of massive vector bosons, $W^\pm$ and Z^0. The large mass accounts for the short range of the force. The weak current takes the form of

$$\alpha\overline{\Psi}\gamma_\mu(1-\gamma_5)\Psi \ . \tag{1}$$

The $\frac{(1-\gamma_5)}{2}$ serves as a projection operator for the left handed chirality states of Ψ. The presence of the left handed projection in the weak Lagrangian means that right-handed neutrinos do not enter into the theory. This mirrors the state of the experimental reality in which a right handed neutrino has never been observed. Lepton number conservation and flavor conservation is assumed by the Standard Model as violations of these laws had not been observed, for example the reaction $\mu \to e\gamma$ has been searched for and not observed. This conservation law was a near article of faith for most physicists. This faith was misplaced. Lepton flavor number conservation is not demanded by a fundamental symmetry in the same way that, for example, electron charge conservation is. Many grand unified theories and extensions to the standard model naturally allow violation of lepton or flavor number. The assumption of lepton flavor conservation along with the lack of right handed neutrinos in the minimal standard model leads to a massless neutrino.

There is now, however, substantial experimental evidence to believe that neutrinos are not massless particles. This comes from the neutrino oscillation experiments. Oscillation is the changing of a neutrino type as it travels through space or matter. This can occur only if the neutrino possesses mass. This will be examined in the next section.

1.3 Neutrino Oscillations

In the case of non-zero neutrino mass and neutrino oscillation, the flavor eigenstates and the mass eigenstates are not the same. Actually, it is well known that in the quark sector both type of states are connected by a unitary matrix (the CKM matrix). Having the neutrinos produced in a state that is not a mass eigenstate leads to the phenomenon of neutrino oscillation. This oscillatory behavior is not present in any other group of particles. Neutrino oscillations are described by quantum mechanics; the oscillations occur among the different neutrino flavors and do not conserve individual lepton number. The flavor eigenstates ν_α are related to the mass eigenstates ν_i via a unitary matrix U:

$$|\nu_\alpha\rangle = U_{\alpha j}|\nu_j\rangle \ . \tag{2}$$

The mass eigenstates show a time dependence according to

$$|\nu_j(x,t)\rangle = e^{-iE_jt}|\nu_j(x,0)\rangle \ . \tag{3}$$

and assuming neutrinos emitted with momentum p at position $x = 0$

$$|\nu_j(x,0)\rangle = e^{ipx}|\nu_j\rangle \ . \tag{4}$$

In the ultra-relativistic limit, $v \sim c$ we may use

$$E_j = (p^2 + m_j^2)^{\frac{1}{2}} \simeq p + \frac{m_j^2}{2p} \ . \tag{5}$$

Therefore, a neutrino with flavor $|\nu_\alpha\rangle$, emitted at $t = 0$, develops with time into a state

$$|\nu_\alpha(x,t)\rangle = \sum_{j=1} U_{\alpha j}e^{-iE_jt}|\nu_j(x,0)\rangle = \sum_{j=1} U_{\alpha j}U^*_{\beta j}e^{ipx}e^{-iE_jt}|\nu_\beta\rangle \ . \tag{6}$$

The transition amplitude for flavor conversion is given by

$$A(\nu_\alpha \mapsto \nu_\beta) = \langle\nu_\alpha|\nu_\beta(x,t)\rangle = \sum_{j=1} U_{\alpha j}U^*_{\beta j}e^{ipx}e^{-iE_jt} \ . \tag{7}$$

Given the smallness of the mass of the neutrino $x = L = t$ in Eq. 6, which gives

$$A(\nu_\alpha \mapsto \nu_\beta) = \langle\nu_\alpha|\nu_\beta(x,t)\rangle = \sum_{j=1} U_{\alpha j}U^*_{\beta j}\exp\left(-i\frac{m_j^2L}{2E}\right) \ . \tag{8}$$

The transition probability can be obtained from the transition amplitude:

$$P(\nu_\alpha \mapsto \nu_\beta) = |A(\nu_\alpha \mapsto \nu_\beta)|^2 \tag{9}$$

$$= \sum_{j=1} |U_{\alpha j}U^*_{\beta j}|^2 + 2\sum_{i>j=1} \Re\left(U_{\alpha i}U^*_{\alpha j}U_{\beta i}U^*_{\beta j}\exp\left(-i\frac{\Delta m_{ij}^2L}{2E}\right)\right) \ . \tag{10}$$

with $\Delta m^2 = m_i^2 - m_j^2$. If CP invariance is assumed ($U_{\beta j}$ real) then Eq. 10 becomes

$$P(\nu_\alpha \mapsto \nu_\beta) = \delta_{\alpha,\beta} - 4\sum_{i>j} U_{\alpha i}U_{\alpha j}U_{\beta i}U_{\beta j}\sin^2\left(\frac{\Delta m_{ij}^2L}{4E}\right) \ . \tag{11}$$

As can be seen from this equation, oscillatory behavior exists as long as at least one neutrino mass eigenstate is different from the others. In addition, the observation of oscillations implies nothing about the absolute value of the masses; oscillations are only sensitive to Δm_{ij}^2. Note that the dependence of the oscillation probability is on L/E.

1.3.1 Two flavor neutrino oscillation

To simplify the algebra, we will restrict our description to 2 flavors. In this case the transformation between mass eigenstates and flavor eigenstates is given by (taking the two flavor states to be ν_e and ν_μ)

$$\begin{pmatrix} \nu_e \\ \nu_\mu \end{pmatrix} = \begin{pmatrix} \cos\theta & \sin\theta \\ -\sin\theta & \cos\theta \end{pmatrix} \begin{pmatrix} \nu_1 \\ \nu_2 \end{pmatrix} . \tag{12}$$

Using Eq. 11, the corresponding transition probability becomes

$$P(\nu_e \mapsto \nu_\mu) = \sin^2 2\theta \sin^2 \left(\frac{\Delta m^2 L}{4E} \right) . \tag{13}$$

This formula again explicitly shows that oscillations only occur if both θ and Δm^2 are non zero. The phase factor in Eq. 11 can be written as

$$\frac{\Delta m_{ij}^2 L}{2\hbar c E} = 2.534 \frac{\Delta m_{ij}^2 (eV^2) L(km)}{E(GeV)}. \tag{14}$$

Then the oscillatory term can be expressed as

$$\sin^2 \left(\frac{\Delta m^2 L}{4E} \right) = \sin^2 \pi \frac{L}{L_o}, \tag{15}$$

with

$$L_o = 4\pi\hbar \frac{E}{\Delta m^2}. \tag{16}$$

In the last equation, L_o represents the oscillation length corresponding to a full cycle. The mass square difference Δm^2 influences the oscillatory length while the mixing angle determines the amplitude of the oscillation. Both unknown parameters have to be determined experimentally.

1.3.2 Three flavor neutrino oscillation

The three flavor oscillation formulas corresponding to Eq. 13 are quite long and complicated. It is customary to approximate them, as we shall describe later. An important feature of this work is that we do not approximate these. Eq. 11 is exact and computationally simple, where now the sum on i and j runs from 1 to 3. For no CP violation, $U_{\alpha i}$ is real and given by,

$$U = \begin{bmatrix} 1 & 0 & 0 \\ 0 & c_{23} & s_{23} \\ 0 & -s_{23} & c_{23} \end{bmatrix} \begin{bmatrix} c_{13} & 0 & s_{13}\mathrm{e}^{-i\delta} \\ 0 & 1 & 0 \\ -s_{13}\mathrm{e}^{i\delta} & 0 & c_{13} \end{bmatrix} \begin{bmatrix} c_{12} & s_{12} & 0 \\ -s_{12} & c_{12} & 0 \\ 0 & 0 & 1 \end{bmatrix} \tag{17}$$

$$= \begin{bmatrix} c_{12}c_{13} & s_{12}c_{13} & s_{13}\mathrm{e}^{-i\delta} \\ -s_{12}c_{23} - c_{12}s_{23}s_{13}\mathrm{e}^{i\delta} & c_{12}c_{23} - s_{12}s_{23}s_{13}\mathrm{e}^{i\delta} & s_{23}c_{13} \\ s_{12}s_{23} - c_{12}c_{23}s_{13}\mathrm{e}^{i\delta} & -c_{12}s_{23} - s_{12}c_{23}s_{13}\mathrm{e}^{i\delta} & c_{23}c_{13} \end{bmatrix} \tag{18}$$

where $c_{ij} \equiv \cos\theta_{ij}$, $s_{ij} \equiv \sin\theta_{ij}$. Notice there are now three mixing angles, θ_{12}, θ_{23} and θ_{13}. In general, for N neutrino flavors the number of mixing angles is determined by the number of different plane rotations that exist in N dimensions which is given by $N(N-1)/2$. For the mass square differences, Δm^2_{ij} only the magnitude enters in vacuum and there are only two independent differences. In matter the sign of Δm^2_{ij} makes a difference, as we will explain later.

1.3.3 Some experimental aspects

Neutrino oscillation experiments can be performed in two different ways; appearance or disappearance mode. In the first case, one searches for possible new flavors which do not exist in the original beam. In the latter case, one explores whether less than the expected number of neutrinos produced with a given flavor arrive at the detector.

1.3.4 Neutrino Oscillations in Matter

Neutrinos can experience interactions when they propagate through matter. This effect was first proposed by S. P. Mikheyev, A. Yu. Smirnov [23]and L.Wolfenstein [24]; it is often called the MSW effect. Electron neutrinos propagating through matter receive a potential energy of V_e through the charged current interaction with electrons in matter:

$$V_e = \sqrt{2}G_F N_e \tag{19}$$

, where G_F is the Fermi coupling constant, N_e is the electron density in matter. Here, some of the most important aspects of the propagation of neutrinos in matter, will be shown. For simplicity only two flavor oscillations will be discussed. The mass eigenstates in vacuum are no longer eigenstates in matter. This brings the necessity of defining a new set of oscillation parameters in matter, for example θ_m, Δm_m^2 and L_m. These new parameters are related to those in vacuum by the following expressions.

$$\sin^2 2\theta_m = \frac{\sin^2 2\theta_v}{\sin^2 2\theta_v + (\frac{A}{\Delta m^2} - \cos 2\theta_v)^2} \; . \tag{20}$$

$$\Delta m_m^2 = \Delta m^2 \sqrt{\sin^2 2\theta_v + (\frac{A}{\Delta m^2} - \cos 2\theta_v)^2} \; . \tag{21}$$

We can write the oscillation probability in matter analogously to the vacuum case

$$P_m(\nu_e \mapsto \nu_\mu) = \sin^2 2\theta_m \sin^2 \left(\frac{\Delta m_m^2 L}{4E} \right) \; . \tag{22}$$

and the corresponding oscillation length in matter

$$L_m = \frac{L_o}{\sqrt{\sin^2 2\theta_v + (\frac{A}{\Delta m^2} - \cos 2\theta_v)^2}} \; . \tag{23}$$

where θ_v is the mixing angle in vacuum and $A = 2\sqrt{2} G_F E N_e$. In Eqs 20, 21 and 23 we can observe that for $A \rightarrow 0$, it follows that $\theta_m \rightarrow \theta_v$, $\Delta m_m^2 \rightarrow \Delta m^2$ and $L_m \rightarrow L_o$. It is important to mention that the sing of the parameter A is different for neutrinos and anti-neutrinos, this difference could have more implications if we account for the sign of Δm^2, which is the term sensitive to the mass hierarchy. From these expressions we observe that the probability of flavor transitions may be either enhanced or suppressed in a way which depends on the density of matter traversed (and on the vacuum oscillation parameters). This will be of high relevance when studying neutrinos propagating through the Sun. Moreover this effect will be relevant in very long baseline neutrino experiments on Earth.

1.4 Neutrino Experiments

Neutrino oscillations experiments can be performed with various neutrino sources which can include man made sources or natural sources:

- Man made sources:

   1. Neutrinos from nuclear reactors

ν source	$E_\nu(MeV)$	L (m)	$\Delta m^2(eV^2)$
Reactor	1	10^2	10^{-5}
Meson Factory	40	10^2	10^{-1}-1
Accelerator	10^3	10^2	10^{-2}
Solar	0.1 - 10	10^{11}	$10^{-10} - 10^{-4}$
Atmospheric	$10^3 - 10^6$	$10^4 - 10^7$	10^{-4} - 1

Table 1: Sensitivity of various neutrino experiments to neutrino oscillations

2. Low energy neutrinos from accelerators at meson factories
3. High energy neutrinos from accelerators

- Natural sources:
    1. Neutrinos generated inside the sun by nuclear fusion.
    2. Neutrinos generated from interactions of cosmic-rays with the atmosphere.

These neutrino sources are summarized qualitatively in Table 1, where the range of energy and the typical observation distances L are given along with the typical mass squared difference Δm^2 to which they are sensitive.

1.4.1 Reactor Experiments

Nuclear reactors produce electron anti-neutrinos by nuclear fission of ^{235}U, ^{238}U, ^{239}Pu and ^{241}Pu with an average energy of 3 MeV. Reactor neutrino experiments measure electron anti-neutrinos produced in the core of nuclear reactors. The signal for $\overline{\nu_e}$ is the reaction $\overline{\nu_e} + p \longrightarrow e^+ + n$. Experiments that have produced results are Gosgen [25], Bugey [26], CHOOZ [27] and Kamland [28]. The positron spectrum from the reaction $\overline{\nu_e} + p \longrightarrow e^+ + n$ has been measured at L = 37.9m from the core of the Gosgen power reactor to search for neutrino oscillations of the type $\overline{\nu_e} \longrightarrow \overline{\nu_x}$ in the low Δm^2 parameter range. The results were consistent with the no oscillation hypothesis. Upper limits of $\Delta m^2 < 0.016\ eV^2$ (90% CL) for full mixing, and $\sin^2 2\theta < 0.17$ (90% CL) in the limit of large Δm^2 were obtained. The ratio of the integrated experimental yield to that predicted for the case of no oscillations was

$1.05 \pm 0.02(stat) \pm 0.05(syst)$ (68% CL) in the Gosgen experiment.

Bugey, using detection modules filled with ^{6}Li-loaded liquid scintillator reported high statistics measurement of the neutrino energy spectra carried out at 15, 40 and 95 meters distance from a 2800 Megawatt reactor. No oscillations were observed. Exclusion zones for oscillation parameters are deduced from the observed consistency of the spectra at the three distances. The minimum excluded values of Δm^2 and $\sin^2 2\theta$ parameters are $1 \times 10^{-2}\ eV^2$ and 2×10^{-2} (at 90% CL),respectively.

The CHOOZ experiment is a long-baseline reactor experiment, the electron anti neutrinos from the two reactors were detected by a liquid scintillation calorimeter located at a distance of about 1 km. The detector was constructed in a tunnel protected from cosmic-rays. From the statistical agreement between detected and expected neutrino event rates, the CHOOZ experiment finds (at 90% CL) no evidence for neutrino oscillations in the disappearance mode for the parameter region given approximately by $\Delta m^2 > 0.9 \times 10^{-3} eV^2$ for maximum mixing and $\sin^2 2\theta > 0.18$ for large Δm^2.

The Kamland experiment consist of an ultra pure liquid scintillator, and is sensitive to the power reactors throughout Japan. Most of the $\overline{\nu_e}$ flux incident at Kamland is produced by power plants located at an average distance of 180 km from the detector. This distance provides the experiment with the sensitivity to probe the Δm^2 associated with MSW induced oscillations in the sun. A two flavor analysis is reported giving the best fit values of $\Delta m^2 = 7.59^{+0.21}_{-0.21} \times 10^{-5} eV^2$ and $\tan^2\theta = 0.47$

1.4.2 Meson Factory Experiments

The meson factory experiments use low energy neutrinos (several tens of MeV) which are generated by the decay of stopped π mesons. The existing experiments of this type are KARMEN [29], and LSND[30].

KARMEN is situated at the beam stop neutrino source at ISIS. It provides neutrinos from $\pi^+ \rightarrow \mu^+$ decay at rest. The oscillation channels $\nu_\mu \rightarrow \nu_e$ and $\overline{\nu_\mu} \rightarrow \overline{\nu_e}$ are investigated with a 56 t liquid scintillation calorimeter at a mean distance of 17.6 m from the source. No evidence for oscillations was found with KARMEN, resulting in 90% CL exclusion limits of $\sin^2 2\theta < 8.5 \times 10^{-3}$ ($\overline{\nu_\mu} \rightarrow \overline{\nu_e}$) and $\sin^2 2\theta < 4 \times 10^{-2}$ ($\nu_\mu \rightarrow \nu_e$) for $\Delta m^2 > 1.0\ eV^2$.

LSND carried out at the Los Alamos Meson Factory searched for $\overline{\nu_\mu} \rightarrow \overline{\nu_e}$ oscillations by using $\overline{\nu_\mu}$ from μ decay. The distance from the LSND detector to the neutrino source is 30 m. The $\overline{\nu_e}$ are detected via the reaction $\overline{\nu_e} + p \rightarrow e^+ + n$. The use of tight cuts to identify e events with correlated γ rays yielded 87.9 events with e^+ energies between 36 and 60 MeV. If attributed to $\overline{\nu_\mu} \rightarrow \overline{\nu_e}$ oscillations, this corresponds to an oscillation probability of $0.26 \pm 0.067 \pm 0.045\%$ indicating that neutrino oscillations occur in the Δm^2 range of 0.2-10 eV^2. A combined likelihood analysis of KARMEN+LSND [31] demonstrates that the different L values allow the two results - KARMEN and LSND - to be consistent with neutrino oscillations for $\Delta m^2 < 2.0\text{MeV}^2$.

1.4.3 High Energy Accelerator Experiments

High energy accelerator experiments use high energy neutrinos (several GeV) which are generated by high energy π K mesons in flight decays. These high energy mesons are produced by high energy proton beams focused on a fixed target. The energy range of these neutrinos is between 0.1 GeV and 100 GeV, and the flight length varies from 0.1 km to 735 km. FNAL [32], CHORUS [33], NOMAD [34] searched for ν_τ appearance, while CDHSW [35] searched for ν_μ disappearance. No oscillation signal was observed from these experiments. The K2K [36] long baseline neutrino oscillation experiment searched for ν_μ disappearance in the same region of Δm^2 as explored by atmospheric neutrinos. The beam consists of 98% muon neutrinos with a mean energy of 1.3 GeV. The neutrino beam is monitored by a near detector before propagating to a distant far detector. Information on neutrino oscillations is obtained by comparing the near detector data with the neutrino beam observed by the far detector which is the Super Kamiokande detector located at a distance of 250 km. The K2K collaboration reported that 108 events have been observed, whereas 150 were expected assuming no oscillations. The oscillation analysis based on the energy spectrum gives the best fit point in the allowed region as $(\sin^2 2\theta, \Delta m^2) = (1.0, 2.8 \times 10^{-3} eV^2)$. The MINOS experiment is another long baseline experiment, very similar to K2K. The MINOS experiment [37]uses a neutrino beam created at the Fermi Laboratory and two detectors separated by a distance of 735 km. The experimental data reported by this experiment is consistent with those results obtained by SK atmospheric and K2K, with a best fit point for the oscillation parameters located at $(\Delta m^2, \sin^2 2\theta) = (2.42 \times 10^{-3} eV^2, 1.0)$.

1.4.4 Solar Neutrino Experiments

Electron neutrinos are produced in nuclear reactions in the core of the Sun; the energy of these neutrinos goes from 0.1 Mev up to 15 Mev. Observations of solar neutrinos reported a number of neutrino events significantly smaller than expected. This is often call the solar neutrino problem. The Homestake [38] experiment was the first experiment which observed neutrinos from the sun using the interaction $\nu_e + Cl^{13} \rightarrow e^- + Ar^{37}$. Kamiokande [39] was the second experiment to detect solar neutrinos, it used a water Cherenkov detector. SAGE [40] and GALLEX [41] experiments also detected neutrinos using $\nu_e + Ga^{71} \rightarrow e^- + Ge^{71}$. Since 1996 Super-Kamiokande [42] has observed solar neutrinos detected by elastic scattering interactions. In 1999 the SNO [43] experiment, a Cherenkov detector using heavy water started observations. It detects charge current interaction $\nu_e + d \rightarrow p + p + e^-$, elastic scattering interaction $\nu_x + e^- \rightarrow \nu_x + e^-$ and neutral current interactions $\nu_x + d \rightarrow p + n + \nu_x$. SNO reported that the “solar neutrino problem ”was definitely a disappearance of electron neutrinos. A combination of the charge current , neutral current and elastic scattering gives the total number of neutrinos which is consistent with the solar model, while the relevant combination gives the number of ν_e neutrinos arriving at the Earth to be about a third of the total emitted by the Sun.

1.4.5 Atmospheric Neutrinos

Atmospheric Neutrinos are produced in the decay of mesons and muons created by the interaction of cosmic rays with the atmosphere. The study of these neutrinos revealed evidence for neutrino oscillations. Underground neutrino experiments have been able to detect atmospheric neutrinos. With these experiments one can measure μ and e neutrino events produced by ν_μ and ν_e charge current interactions. Among all these experiments NUSEX [44], FREJUS [45] observed data that was consistent with the expectations; however Kamiokande [46], SOUDAN [47] and IMB [11] reported a signal which was significantly smaller than the expected. This is know as the “Atmospheric Neutrino Anomaly ”. In 1996 the Super Kamiokande [48] experiment started; they reported a deficit in the ν_μ channel, a result consistent with $\nu_\mu \rightarrow \nu_\tau$ oscillations. Years later the Super Kamiokande collaboration confirmed that the atmospheric neutrino data showed an L/E dependence consistent with neutrino oscillation. Among all the experiments studying neutrino from the atmosphere, the Super Kamiokande experiment is the one that contributes the most to the determination of the neutrino oscillation parameters. The properties of this experiment make possible the study of neutrinos coming from different distances as well as studying neutrinos with different energies. It also detects neutrinos of different flavors, electron neutrinos and muon neutrinos.

1.5 Current Status

The current experimental picture for the three neutrino oscillation signal indications can be summarized:

- For the atmospheric neutrino parameter space: evidence from Super Kamiokande is very strong for $\nu_\mu \rightarrow \nu_x$ with small ν_e oscillations. The oscillation parameters have been independently confirmed using the K2K and MINOS beam of ~1 GeV ν_μ's. The present best fit values $(\Delta m^2, \sin^2 2\theta)$ are $(2.5 \times 10^{-3} eV^2, 1.0)$
- For the solar neutrino parameter space $(\nu_e \rightarrow \nu_x)$, the solar neutrino problem is now solved. While Super-K data favored large mixing via day/night and spectral measurements, SNO's D_2O-based NC and CC measurements have definitively confirmed that solar neutrinos are oscillating, and have reduced the allowed parameter space to the large mixing angle region using day/night and spectral measurements. More importantly, the KamLAND experiment has confirmed the solar solution using reactor $\bar{\nu}_e$'s. The best fit parameters for solar neutrinos are $(\Delta m^2, \sin^2\theta)$ are $(7.9 \times 10^{-5} eV^2, 0.30)$

- The LSND indication of $\bar{\nu}_\mu \rightarrow \bar{\nu}_e$ still stands; KARMEN does not rule out all of LSND's allowed parameters. The next experiment to investigate the LSND parameter space is MiniBooNE (Booster Neutrino Experiment.) This looks at ~ 1 GeV neutrinos from the 8 GeV booster at Fermilab, at a baseline of about 500 m (with a second experiment planned at longer baseline if an oscillation signal is seen.) This experiment is primarily designed to test $\nu_\mu \rightarrow \nu_e$ at about the same L/E as LSND. Since the neutrino energy is higher, and the backgrounds are different, systematic will presumably be different from those at LSND. MiniBooNE expects to cover all of LSND parameter space. The MiniBooNE Collaboration [49] reported the results of a search for ν_e appearance and found no excess of events for neutrinos with energy higher than 475 MeV. This is consistent with no neutrino oscillation in the framework of two neutrino oscillations model, a result that does not confirm the LSND mass prediction.

1.5.1 Non-Oscillation Neutrino Experiments

So far this review has focused on neutrino oscillation studies. However, oscillation physics hardly comprises all of neutrino physics. Perhaps the two most compelling experimental questions that cannot be answered by oscillation experiments are:

- What is the absolute mass scale? This question is fundamental, and additionally has profound consequences for cosmology.
- Are neutrinos Majorana or Dirac? In other words, are they their own antiparticles, described by a two-component spinor, or described by a 4-component Dirac spinor? The answer to this question has tremendous implications for the construction of the theory describing neutrino masses. For instance, the “see-saw” mechanisms for neutrino mass generation [50] require the neutrino to be Majorana.

In the following I will very briefly review experiments which aim to answer some, or both, of these questions.

- Kinematic Neutrino Mass Experiments.

As noted above, neutrino oscillation measurements say nothing about the absolute masses of the mass states or the average masses of the flavor states. The idea behind kinematic neutrino mass searches is simple: look for missing energy. The traditional tritium beta decay spectrum endpoint experiments now have limits for absolute the $\bar{\nu}_e$ mass from the Mainz and Troitsk experiments of ≤ 3 eV [51], and there are some prospects for improvement down to the sub-eV level by the Katrin[52] experiment. Some new techniques are also under consideration [53]. The ν_μ and ν_τ mass limits are currently 190 keV [54] and 15.5 MeV [55] respectively; however improving these direct ν_μ and ν_τ mass measurements seems less compelling if information about differences between the mass states is available from oscillation experiments.

- Double Beta Decay

  Another way of getting at absolute neutrino mass and determine that the neutrino is Majorana, is to discover neutrino less double beta decay, $(N, Z) \rightarrow (N-2, Z+2) + e^- + e^-$. Such a decay is only possible if the neutrino has mass, and is Majorana. The current 90% confidence level lowest mass limits from non-observation of double beta decay are $\langle m_\nu \rangle = |\Sigma U_{1j}^2 m_{\nu j}| < 0.35$ eV [51, 56] The current best limits are from ^{76}Ge experiments. Many new double beta decay search experiments are planned and under construction, some employing novel techniques. It appears challenging but not impossible to push the limits down to $\sim$0.02 eV [57].

CHAPTER II

ATMOSPHERIC NEUTRINOS

2.1 Cosmic Rays

In 1912, Victor Hess [58] used a device to measure the rate of ion production inside a hermetically sealed container to an altitude of 5300 meters in a free balloon flight. He found the ionization rate increased approximately four fold over the rate at ground level. He concluded "The results of my observation are best explained by the assumption that a radiation of very great penetrating power enters our atmosphere from above ". In 1913-14, Werner Kolhörster confirmed Victor Hess' results by measuring the increased ionization rate at an altitude of 9 km. Hess received the Nobel Prize in Physics in 1936 for his discovery of what came to be called "cosmic rays". Cosmic rays are very energetic particles coming from the outer space and colliding with the Earth's atmosphere. They come from different sources such as the Sun, neutron stars, supernovae, black holes, etc. There exist two types of cosmic rays, primary and secondary. The primary cosmic rays are the ones that arise from astrophysical sources. The primary cosmic rays generally do not make it through the earth's atmosphere, and hence constitute only a small fraction of what is measured by particle detectors at the earth's surface. What is measured, however, are the results of interactions of the primary cosmic rays with the upper atmosphere. These remnants are termed "secondary"cosmic rays.

Approximately 90% of all cosmic rays are protons, about 9% are helium nuclei (alpha particles) and about 1% are electrons. The remaining small fraction is made up of heavier nuclei which are abundant end products of nuclear synthesis in stars.

Cosmic rays [60] can have energies of over 10^{20} eV, far higher than the 10^{12} to 10^{13} eV that man-made particle accelerators can produce. Figure 3 pictures the energy spectrum of cosmic rays. The flux of cosmic rays hitting the Earth's atmosphere is affected by different processes; the Earth's magnetic field and the solar wind.

- The Earth's magnetic field deflects some of the cosmic rays, which is confirmed by

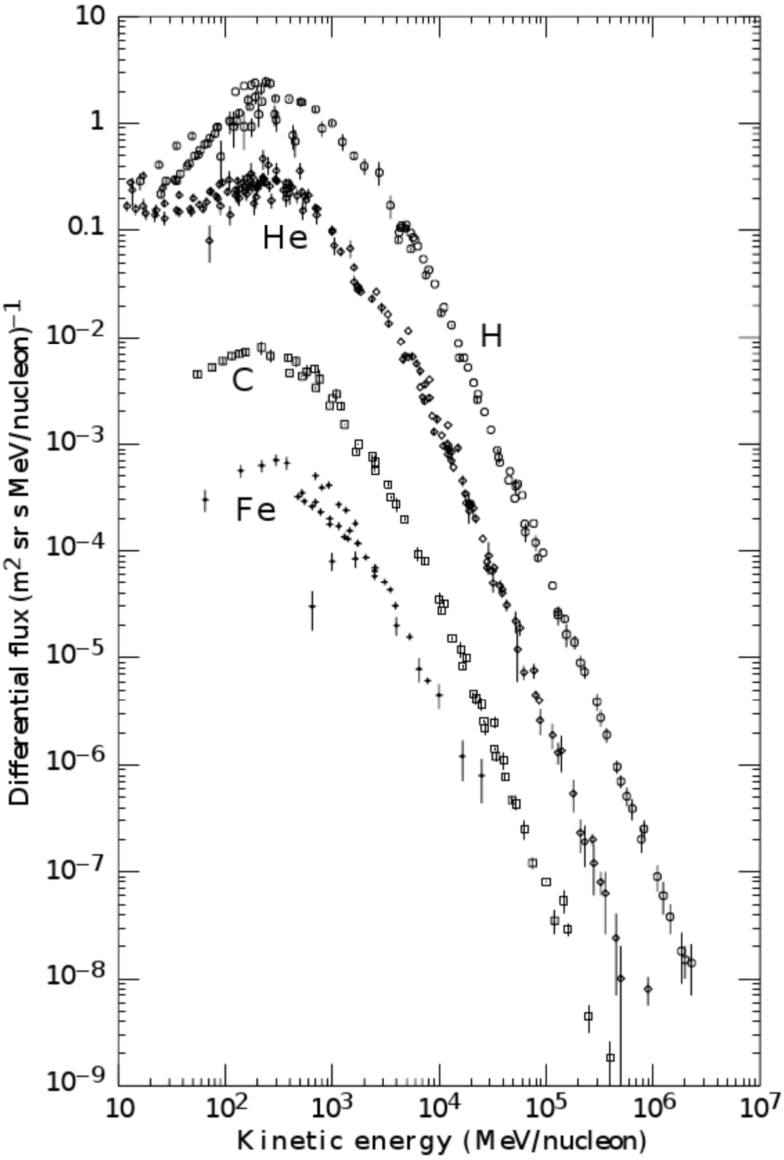

Figure 3: Cosmic Ray Spectrum from [59]

the fact that the intensity of cosmic radiation is dependent on latitude, longitude and azimuthal angle. The cosmic flux depends on the eastern or western directions due to the polarity of the Earths geomagnetic field and the positive charge dominance in primary cosmic rays; this is termed the east-west effect. The cosmic ray intensity at the equator is lower than at the poles as the geomagnetic cutoff value is greatest at the equator. This can be understood by the fact that charged particles tend to move in the direction of field lines and not across them. This is the reason the Aurorae occurs at the poles, since the field lines curve down towards the Earths surface there. Finally, the longitude dependence arises from the fact that the geomagnetic dipole axis is not parallel to the Earths rotation axis.

- Cosmic rays are affected by the variations in the solar magnetic field, which is modulated by the solar wind, given that the amount of solar wind is not constant due to changes in solar activity over its regular eleven-year cycle. Therefore the cosmic ray flux varies in auto correlation with solar activity.

When cosmic ray particles enter the Earth's atmosphere they collide with molecules, mainly oxygen and nitrogen, to produce a cascade of lighter particles, a so called air shower. The general idea is shown in figure 4 which shows a cosmic ray shower produced by a high energy proton striking an atmospheric molecule.

2.2 Neutrino Fluxes

Atmospheric neutrinos are produced [61] in the collision of primary cosmic rays with the air in the upper atmosphere. The atmosphere acts as a shield against cosmic rays, and therefore most of the incoming cosmic rays never reach the surface of the Earth. When primary cosmic rays collide in the atmosphere they produce secondary particles, pions and some kaons which later will decay and produce neutrinos.

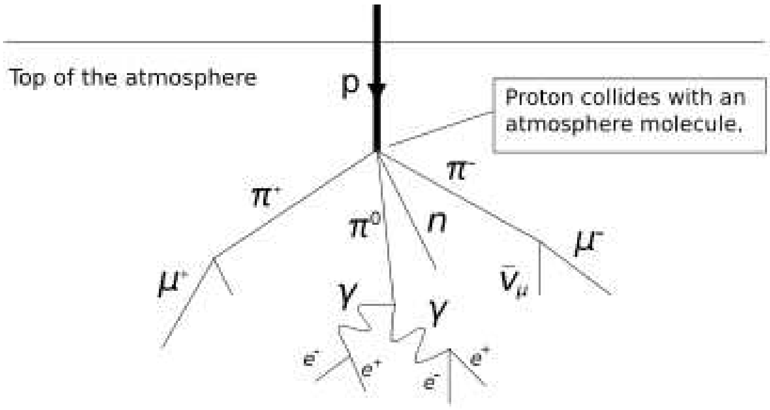

Figure 4: Interaction with the Earth's atmosphere

The main decay chain for neutrino production is

$$\begin{aligned}\pi^+ &\longrightarrow \mu^+ + \nu_\mu \\ &\qquad\longrightarrow e^+ + \nu_e + \overline{\nu}_\mu \\ \pi^- &\longrightarrow \mu^- + \overline{\nu}_\mu \\ &\qquad\longrightarrow e^+ + \overline{\nu_e} + \nu_\mu .\end{aligned}$$

Note two muon and one electron neutrinos are produced by the above decay chain. Thus the neutrino flux ratio $(\nu_\mu + \overline{\nu}_\mu)/(\nu_e + \overline{\nu}_e)$ is expected to be TWO for low energies. For high energies, this ratio increases because the high energy muons reach the ground without decaying and therefore the relative number of electron neutrinos decreases. The distance traveled by atmospheric neutrinos to an underground detector varies from 15 km to 13,000 km depending on their production location as shown in Figure 5. The neutrino zenith angle is defined to be the angle between the neutrino direction and a line perpendicular to the ground, with the $\cos\theta$ of the zenith angle chosen such that, $\cos\theta = -1$ corresponds to the upward-going direction, $\cos\theta = 0$ to the horizontal direction, and $\cos\theta = +1$ to the downward-going direction.

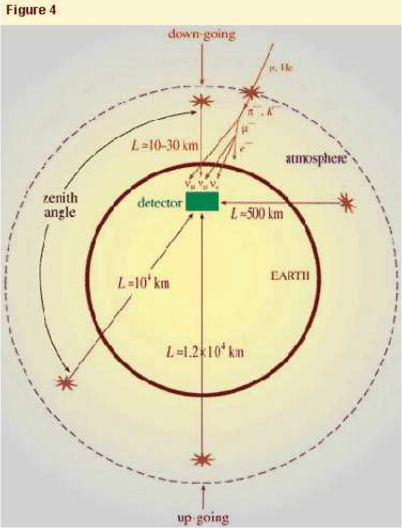

Figure 5: Schematic view of the distrance traveled by atmospheric neutrinos.

2.3 Atmospheric Neutrino Experiments

The first atmospheric neutrino experiments employed water Cherenkov detectors, Irvine-Michigan-Brookhaven (IMB) [11, 12] and Kamiokande [46]. Although their primary scientific goals were to search for proton decay, atmospheric neutrinos were found to be their main backgrounds. These backgrounds quickly became a topic of interest for study. Both experiments found that the measured ratio was different from two. In practice, they constructed the double ratio R,

$$R(\tfrac{\mu}{e}) = \frac{\left(\frac{N_\mu}{N_e}\right)_{DATA}}{\left(\frac{N_\mu}{N_e}\right)_{MC}}$$

Where N_μ (N_e) is the muon (electron) number of events and the double ration takes the ratio of data to that of a Monte Carlo prediction. The double ratio is used in order to to cancel the detector systematic and the uncertainties in the flux calculations, where the uncertainty in the absolute atmospheric neutrino flux is about 20 % while the error in the flavor ratio is expected to be about 5 %.

Both, the IMB and Kamiokande experiments measured R that was much less than unity. This became the atmospheric neutrino anomaly in the 1980s and was interpreted as a possible indication for neutrino oscillations [62]. Later experiments, NUSEX [44] and Frejus [45], using iron calorimeters, reported no deviation from unity but used smaller data samples. However, Soudan 2, also an iron tracking calorimeter, later measured a smaller flavor ratio with higher statistics [47]. In addition to the flavor ratio, Kamiokande measured a zenith angle dependence of R. Using upward-going muons induced by atmospheric neutrinos, Kamiokande [46], Soudan 2 [47], and MACRO (composed of liquid scintillation counters) [63] found a zenith angle dependent deficit of muon neutrinos. Recently, the atmospheric neutrino results from K2K [36] and the MINOS experiment have also found the consistent results with atmospheric measurements [64]. All observations indicated that neutrinos oscillate, and that the expected Δm^2 and $\sin^2 2\theta$ by Kamiokande [46, 65], MACRO [63, 66], Soudan 2 [47, 67], K2K [36] and MINOS [64] in a $\nu_\mu \rightarrow \nu_\tau$ analyzes are consistent with each other.

Since starting operations in 1996, Super-K also observed a ratio much smaller than unity, with much larger statistics, [48, 68]. In 1998, Super-K announced its first evidence for neutrino oscillations by reporting a strong zenith angle dependent deficit of muon neutrinos [48]. Precise extraction of the oscillation parameters from the atmospheric neutrino data have been made [48, 68], and the evidence for an oscillatory signature in the atmospheric neutrino oscillations have been observed. The Super-K atmospheric neutrino data favor $\nu_\mu \rightarrow \nu_\tau$ oscillations and have excluded $\nu_\mu \rightarrow \nu_e$[69] and pure $\nu_\mu \rightarrow \nu_{sterile}$ oscillations [70] as a dominant source of the deficit of muon neutrinos.

2.4 Super Kamiokande Experiment

The Kamioka Observatory, Institute for Cosmic Ray Research is a neutrino physics laboratory located underground in the Mozumi Mine near the city of Hida (in an area formerly known as Kamioka) in Gifu Prefecture, Japan. The precursor to the Super Kamiokande experiment was the Kamioka experiment, where the name KamiokaNDE came from Kamioka Nucleon Decay Experiment. It was a large water Cherenkov detector designed to search for proton decay. To observe the decay of a particle with a lifetime as long as a proton, the experiment must run for a long time and observe an enormous number of protons. This can be done most cost effectively if the target (the source of the protons) and the detector itself are made of the same material. Water is an ideal candidate because it is inexpensive,

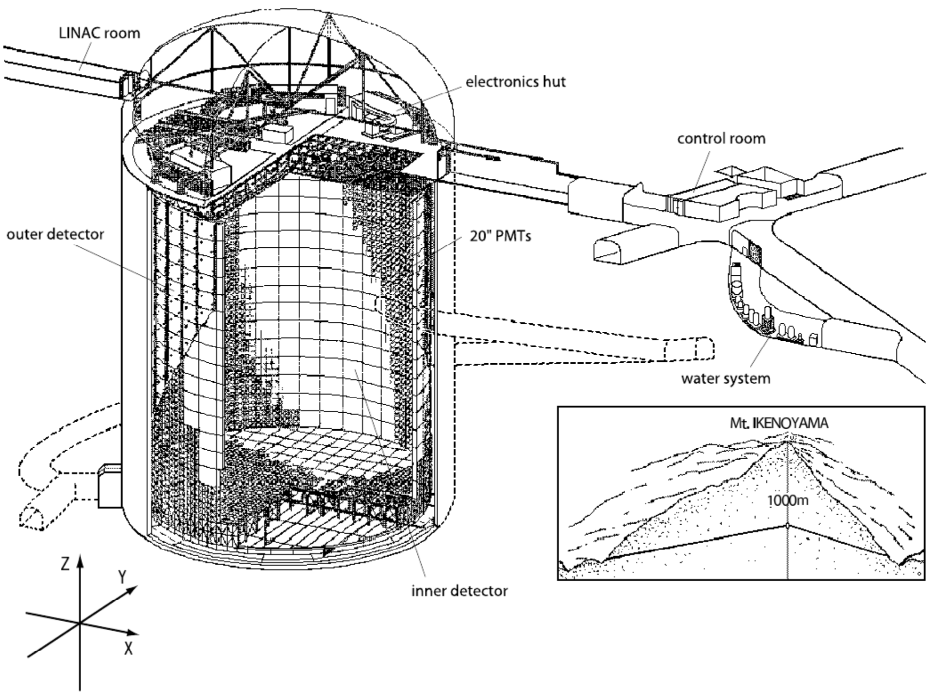

Figure 6: Schematic view of the Super Kamiokande Detector taken from [72]

easy to purify, stable, and can detect relativistic charged particles through the production of Cherenkov radiation. A proton decay [71] detector must be buried deep underground because the background from cosmic ray muons in such a large detector located on the surface of the Earth would be far too large. The muon rate in the Kamiokande experiment was about 0.4 Hz, roughly five orders of magnitude smaller than what it would have been if the detector had been located at the surface.

The Kamioka detector was a cylindrical tank which contained 4.5 ktons of pure water and had about one thousand photomultiplier tubes (PMTs) attached to the inner surface. The size of the outer detector was 16.0 m in height and 15.6 m in diameter. The detector failed to observe proton decay, but set what was then the world's best limit on the lifetime of the proton.

The Kamiokande experiment happened to be running at a particularly fortuitous time, as a supernova occurred while the detector was online and taking data. With the upgrades that had taken place the detector was sensitive enough to observe the thermal neutrinos produced by Supernova 1987A [73], which took place roughly 160,000 light years away in the Large Magellanic Cloud. The neutrinos arrived at the Earth in February of 1987, and the Kamiokande detector observed 11 events. The Kamiokande experiment was replaced by a much larger experiment with much improved resolution, The Super Kamiokande (SK) experiment. We provide a more detailed discusion because the data from this detector provide the central result for this dissertation. Super-Kamiokande is a large, underground, water Cherenkov detector located in an active zinc mine in the Japanese Alps (see Figure 6) . The experiment began data taking in April 1996. It supersedes previous detectors (IMB and Kamiokande) both in size and resolution. The container consists of a stainless steel tank, 40 meters tall by 40 meters in diameter. It is filled with 50 ktons of ultra-pure water: the optical attenuation length is in excess of 70 meters. The volume is separated into a large inner region, optically isolated from a 2 meter wide outer region. The inner region is viewed with 11,200 photomultiplier tubes, each 50 centimeters in diameter. These tubes record the Cherenkov light from relativistic charged particles created in or passing through the water. The outer region of water acts as a passive shield against low energy particles entering from outside the detector. In addition, it is instrumented with 1800 photomultiplier tubes that are used to veto or reconstruct muons that enter or exit the detector. Large volume water detectors were invented to discover proton decay, but so far have only set limits. As Super-K is approximately 15 times larger than the previous generation of detectors, it can reach a proton lifetime of 10^{34} years, probing predictions of modern Grand Unified Theories. The background for proton decay are the interactions of 1 GeV neutrinos produced by cosmic ray showers in the upper atmosphere. As observed in the prior generation of water Cherenkov detectors, these atmospheric neutrinos, seemed to have puzzling behavior compared to theoretical expectation. In 1998, Super-K resolved this puzzle as being due to neutrino flavor oscillation.

2.4.1 Detection Procedure

The Super Kamiokande detector detects particles by measuring the emitted Cherekov radiation. In 1934 P. A. Cherenkov discovered this radiation which is electromagnetic radiation emitted when a charged particle travels through a medium with a velocity v greater than the speed of light in that medium (i.e. $v > c/n$), where c is the speed of light in vacuum and n is the index of refraction of the medium. Super-K contains ultra-pure water, of which the refraction index is $n = 1.34$. The Cherenkov threshold momentum for electrons/positrons, muons , and pions are 0.58, 120, and 159 MeV/c respectively. The emitted Cherenkov photons form a cone with an opening angle θ_C with respect to the direction of the particle. The opening angle θ_C is given by:

$$\cos\theta_C = \frac{1}{n(\lambda)\beta},$$

where $\beta = v/c$. The number of Cherenkov photons (dN) radiated per unit wavelength ($d\lambda$) per unit distance (dx) the charged particle travels is given by :

$$\frac{d^2N}{dxd\lambda} = \frac{2\pi\alpha}{\lambda^2}\left(1 - \frac{1}{(n(\lambda)\beta)^2}\right) = \frac{2\pi\alpha}{\lambda^2}\sin^2\theta_C,$$

where α is the fine structure constant. For relativistically charged particles ($\beta \approx 1$) in pure water, the Cherenkov angle is $\theta_C \approx 42$ degrees , and the number of photons emitted is approximately 340 per cm over the Cherenkov spectrum between the wavelength of 300 nm to 600 nm, where the photomultiplier tubes (PMTs) are sensitive. In the SK detector, Cherenkov photons are detected in order to observe charged particles producing the radiation. The position, direction, energy, and the type of charged particles are reconstructed by measuring the number of Cherenkov photons in ring like patterns.

CHAPTER III

EXPERIMENTAL SIMULATION I

The Super Kamiokande experiment plays a crucial role in the phenomenology of neutrino oscillation. The next two chapters explain in detail the procedure developed in this dissertation to simulate this experiment. Unlike experimentalists, we don't attempt to simulate each single part of the experiment which would require a Monte Carlo simulation with the complications that such calculations involve. We choose not to a do Monte Carlo simulations for two reasons: First, a Monte Carlo project represents a huge amount of work, and in particular would call for the participation of many people. Secondly, performing Monte Carlo calculations would involve a great amount computer resources, which is not available for our analysis purposes. Instead, we need an analysis tool capable of simulating most of the experimental results and at the same time practical, simple, and able to provide answers in a reasonable amount of time. In order to do that we have developed a computer code and a physics model that simplifies the simulations of each experimental event making use of some well-known experimental aspects as well as making use of some of the Monte Carlo results provided by the Super Kamiokande Collaboration.

3.1 Our Model of the Super Kamiokande Experiment

In this section we provide a complete description of the main ingredients that have been used to model the SK experiment. The first ingredient we need to include in our simulation is a model of the neutrino source. In this case, since we are studying atmospheric neutrinos, we need to have a description of the neutrinos coming from the atmosphere. As we have mentioned in previous chapters, atmospheric neutrinos are the products of the interactions that occur between primary cosmic rays and the molecules in the upper atmosphere. The current status of the measurements of the cosmic ray proton flux is shown in Figure 7. The primary cosmic ray spectrum has been precisely measured by BESS and AMS [81, 82] in experiments for energies up to 100 GeV . The cosmic ray flux changes depending on

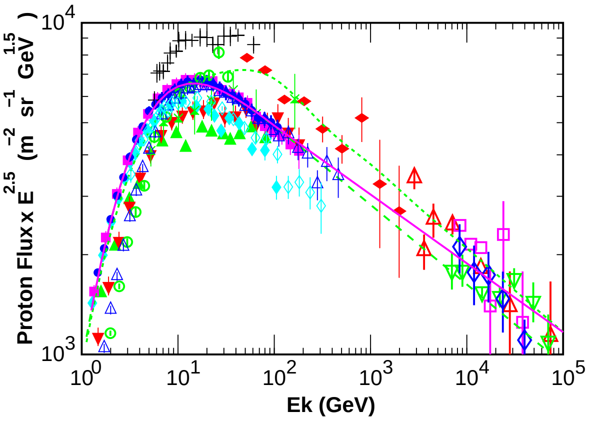

Figure 7: Primary cosmic ray for protons from [74]. Crosses indicate data from Ref. [75], open circles indicate data from MASS [76], closed upward triangles LEAP [77], closed downward triangles IMAX [78], closed vertical diamonds CAPRICE-94 [79], open vertical diamonds CAPRICE-98 [80], closed circles BESS [81], closed horizontal diamonds AMS [82], open upward triangle BESS-TeV [83], closed horizontal diamonds Ryan et al [84], open downward large triangles JACEE [85], open diamonds large RUNJOB [86], open upward large triangles from Ivanenko et al. [87], and open large squares from Kawamura et al. [88].

the turbulence of the solar wind, which is higher when the solar activity is high (solar maximum) and lower when the solar activity is low (solar minimum). In addition we have the geomagnetic field affecting the direction of the incoming cosmic rays. All these effects are taken into account in calculating the neutrino fluxes.

Different groups are working on modeling the neutrino fluxes, BARTOL [89], HONDA [90] and FLUKA [91] have 3 dimensional models that seem to provide similar answers. For our simulation we use the HONDA 3D [74] flux which is specifically designed for the Super Kamiokande location. It utilizes a 3 dimensional model to simulate the propagation of particles in all directions with respect to the incident cosmic ray. Previous one dimensional models assumed the created neutrino to be in the same direction as the parent meson. The Honda neutrino fluxes provide the flux of neutrinos and anti-neutrinos for both flavors, electron and muons. They are given as function of zenith angle , azimuthal angle and energy, for an energy range of 0.1 GeV to 10 TeV. Figure 8, shows the flux of $\nu_e + \overline{\nu}_e$ and $\nu_\mu + \overline{\nu}_\mu$ averaged over all directions. The flavor ratio is about two up to a few GeV energy, then it

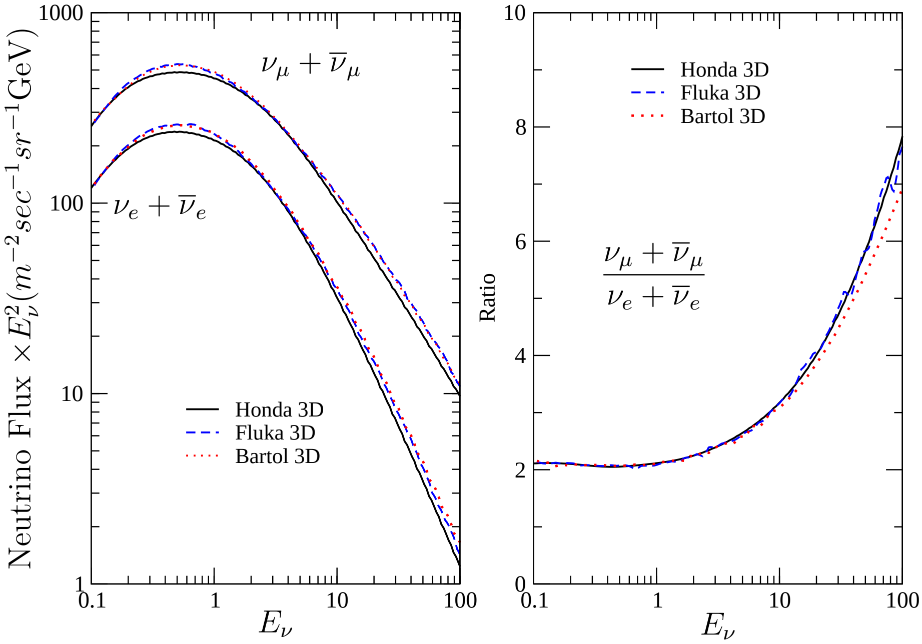

Figure 8: Flux of atmospheric neutrinos

becomes larger than two. As the neutrino energy increases more cosmic ray muons reach the ground before decaying. The systematic uncertainty in the absolute flux is estimated to be about 20% due to the uncertainty of the absolute primary cosmic ray flux. The uncertainty in the flavor ratio is smaller than about 5%.

The calculated flux ratios of $\nu_e/\overline{\nu}_e$ and $\nu_\mu/\overline{\nu}_\mu$ are shown in figure 9. The calculations from different models agree to about 5 % for both below 10 GeV, while above 10 GeV the disagreement is larger as a function of the neutrino energy becoming 10% and 25% at 100 GeV for ν_e and ν_μ, respectively. The zenith angular dependence is shown in figure 10 where $\cos\theta = 1$ and $\cos\theta = -1$ refer to the neutrinos coming from above and below respectively.

3.2 Atmospheric Neutrino Interactions

Once we know the neutrino flux, we can proceed to study the second ingredient, something required for for the simulation of the detector. As we have mentioned, the Super Kamiokande detector consists of a container filled with purified water. As we have also mentioned earlier,

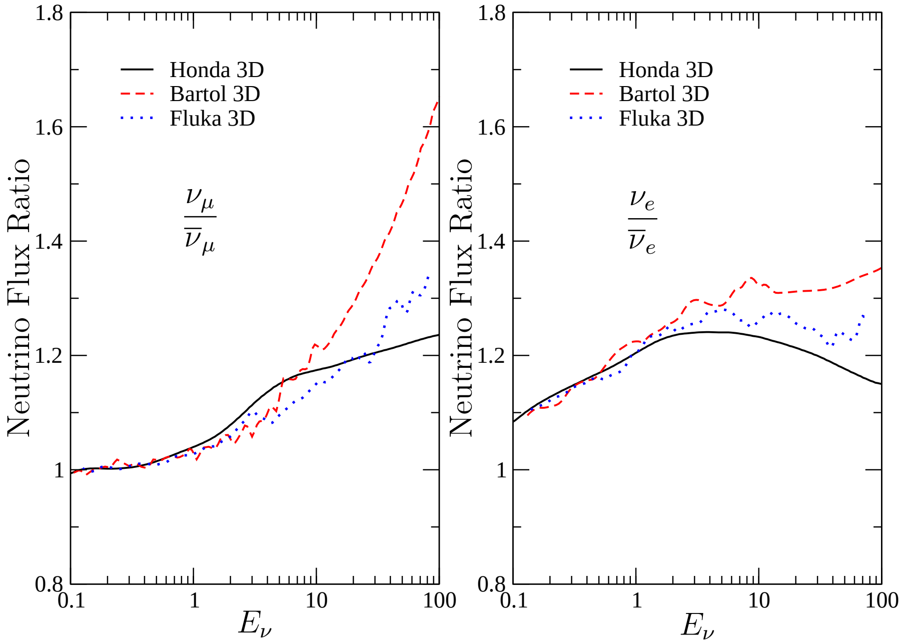

Figure 9: Calculated atmospheric flux ratios.

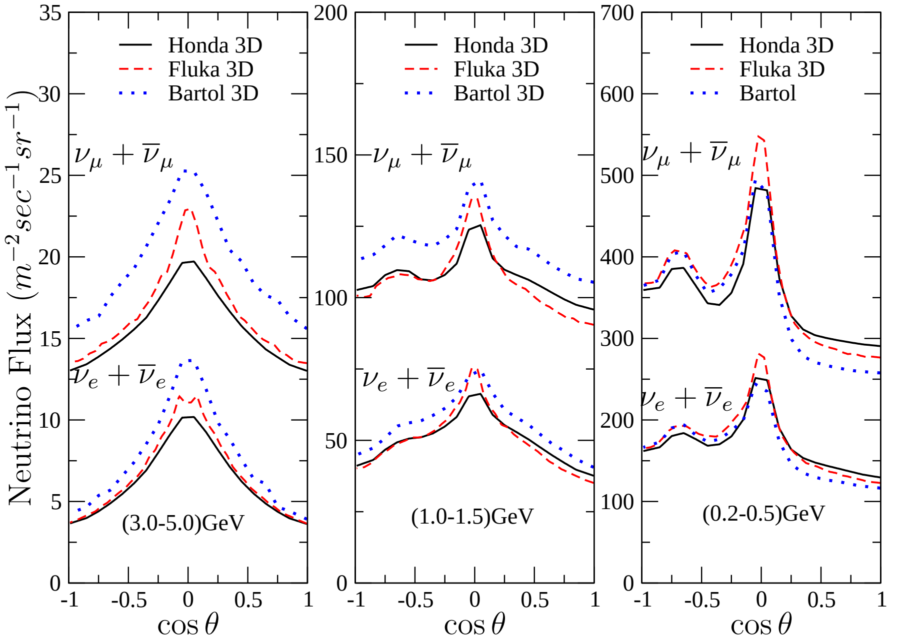

Figure 10: Zenith angular dependence of atmospheric neutrinos.

neutrinos being weakly interacting particles, they can be detected by two different methods: neutral current interactions (NC) or charge current (CC) interactions. The neutral current interaction occurs when a neutrino exchanges an electrically neutral Z boson to scatter off an electron that moves relativistically and generates Cherenkov light. All three flavors of neutrinos can interact with nuclei and electrons via the neutral current. On the other hand the charged current interaction occurs when a neutrino interacts with a nucleon by exchanging a $W^{\pm}$ to generate a lepton. This lepton preserves the same flavor as the neutrino. From the properties of the SK detector, as well as the energy range of the neutrinos, we can classify the most relevant neutrino interactions in the following way:

3.2.1 Quasi Elastic Cross Section

Quasi elastic scattering occurs when a neutrino strikes a nucleus, and the scattered particle neutrino or lepton has nearly the same energy as the incident neutrino. It can either be charge current quasi-elastic (CCQE) scattering, where a neutrino scatters off a nucleon generating a lepton of the same flavor, or NC elastic scattering, where any flavor neutrino scatters off an electron. The differential cross section of the charged current quasi-elastic scattering for free protons (i.e. the hydrogen atom in water) is given by [92]

$$\frac{d\sigma^{\nu(\overline{\nu})}}{dq^2} = \frac{M^2 G_F^2 \cos^2\theta_c}{8\pi E_\nu^2}\left[A(q^2) \mp B(q^2)\frac{s-u}{M^2} + C(q^2)\frac{(s-u)^2}{M^4}\right]$$

where E_ν is the neutrino energy, M is the mass of the target nucleon, G_F is the Fermi coupling constant, θ_C is the Cabbibo angle, q^2 is the four-momentum transferred to the nucleon, and s and u are Mandelstam variables [93]. The factors A, B and C are :

$$\begin{aligned} A(q^2) = {} & \frac{m^2-q^2}{4M^2}\left[\left(4-\frac{q^2}{M^2}\right) \mid F_A \mid^2 - \left(4+\frac{q^2}{M^2}\right) \mid F_V^1 \mid^2\right] \\ & -\frac{m^2-q^2}{4M^2}\left[\frac{q^2}{M^2} \mid \xi F_V^2 \mid^2 \left(1+\frac{q^2}{4M^2}\right) - \frac{4q^2\xi F_V^1 F_V^2}{M^2} - \frac{m^2}{M^2}\left((F_V^1+\xi F_V^2)^2 + \mid F_A \mid^2\right)\right], \end{aligned} \tag{24}$$

$$B(q^2) = \frac{q^2}{M^2}\left((\xi F_V^2 + F_V^1)F_A\right),$$

$$C(q^2) = \frac{1}{4}\left(\mid F_A \mid^2 + \mid F_V^1 \mid^2 - \frac{q^2}{4M^2} \mid \xi F_V^2 \mid^2\right),$$

where m is the lepton mass, $\xi = \mu_p - \mu_n = 3.7$ MeV. The vector form factors, $F_V^1(q^2)$ and $F_V^2(q^2)$ and the axial vector form factor, $F_A(q^2)$ are determined experimentally and are given by

$$F_V^1(q^2) = \left(1 - \frac{q^2}{4M^2}\right)^{-1} \left[G_E(q^2) - \frac{q^2}{4M^2}G_M(q^2)\right],$$

$$\xi F_V^2(q^2) = \left(1 - \frac{q^2}{4M^2}\right)^{-1} \left[G_E(q^2) - G_M(q^2)\right],$$

$$F_A(q^2) = -1.23\left(1 - \frac{q^2}{M_A^2}\right)^{-2},$$

$$G_E(q^2) = (1+\xi)^{-1}G_M(q^2) = \left(1 - \frac{q^2}{M_V^2}\right)^{-2}$$

where G_E and G_M are the electric and magnetic form factors. The vector mass M_V is set to 0.84 GeV and the axial vector mass M_A is set to 1.11 GeV, as taken from experimental data [94]. For larger M_A values, interactions with higher Q^2 values are enhanced. The M_A value is tuned utilizing the K2K near detector data. Figure 11 shows the cross section for the quasi-elastic scattering.

The cross sections for neutral current elastic scattering are approximated through from the following relations [96, 97]:

$$\sigma(\nu p \rightarrow \nu p) = 0.153\sigma(\nu n \rightarrow e^- p)$$

$$\sigma(\nu n \rightarrow \nu n) = 1.5\sigma(\nu p \rightarrow \nu p)$$

$$\sigma(\overline{\nu} p \rightarrow \overline{\nu} p) = 0.218\sigma(\overline{\nu} p \rightarrow e^+ n)$$

$$\sigma(\overline{\nu} n \rightarrow \overline{\nu} n) = 1.0\sigma(\overline{\nu} p \rightarrow \overline{\nu} p)$$

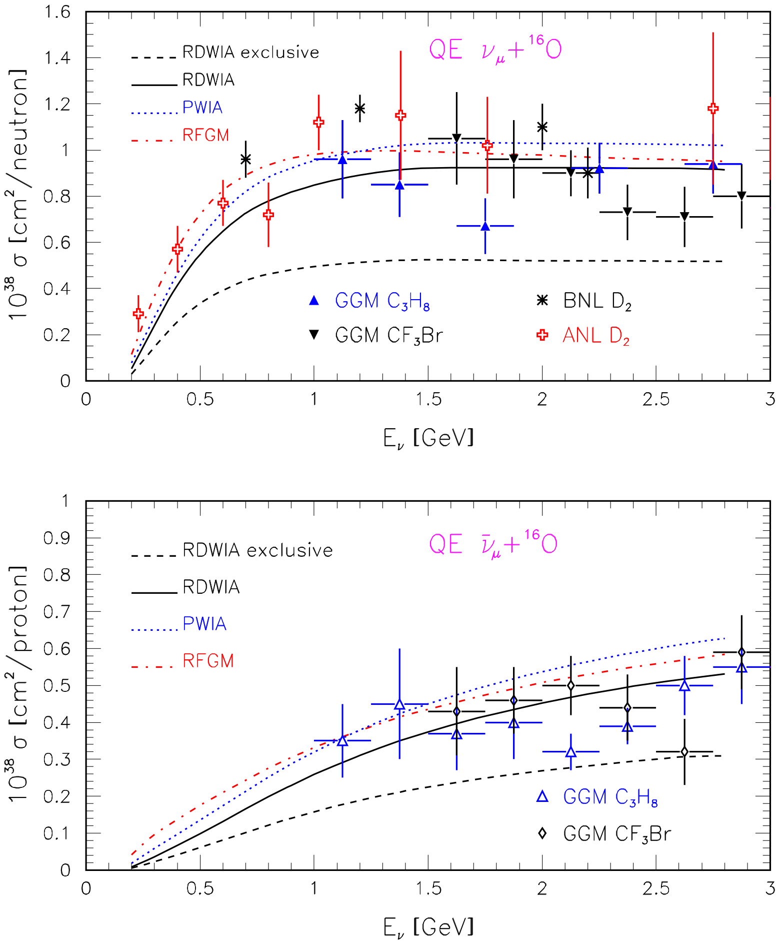

Figure 11: Quasi-elastic neutrino cross section of muon neutrino (upper panel) and antineutrino (lower panel) on ^{16}O as a function of incoming (anti) neutrino energy, from [95].

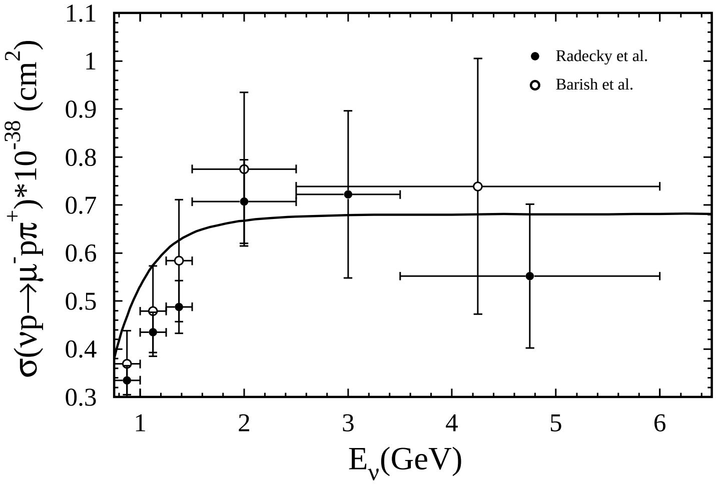

Figure 12: Total cross section for the $\nu_\mu + p \to \mu^- + p + \pi^+$ process plotted versus the incoming neutrino energy, figure taken from [98].

3.2.2 Single Pion Production

The resonant single meson production of π, K, and η is simulated based on the model of Rein and Sehgal [99, 100].

$$\nu + N \rightarrow l + N^*$$

$$N^* \rightarrow N^{'} + \text{meson}$$

This method assumes an intermediate baryon resonance : where N and $N^{'}$ are nucleons and N^* is a baryon resonance. The differential cross section of single-meson production is a product of the amplitude of each resonance production and the probability of the baryon resonance decay to this meson. For negligible decay width of a baryon resonance (N^*), the differential cross section is

$$\frac{d^2\sigma}{dq^2 dE_\nu} = \frac{1}{32\pi M E_\nu^2}\frac{1}{2} \mid \textstyle\sum_j T(\nu N \rightarrow l N_j^*)\sqrt{\chi_E} \left(sign(N_j^*)\sqrt{\frac{\Gamma_j}{2\pi}} \frac{1}{W - M_j + i\frac{\Gamma_j}{2}} \right) \mid^2$$

where M is the mass of the target nucleon, E_ν the neutrino energy, W is the invariant mass of the hadronic system (or the mass of the intermediate baryon resonance), M_j the mass of the baryon resonance N_j^* and $T(\nu N \rightarrow l N_j^*)$ is the amplitude for resonance production, which is calculated using the FKR (Feynman-Kislinger-Ravndal) model [101], $sign(N_j^*)$ is the sign of the decay amplitude N_j^*, Γ_j the total decay width of N_j^*, and χ_E the branching of N_j^* to $N^{'}$ + meson. The invariant mass, W , is restricted to be less than 2 GeV/c^2 . For W larger than 2 GeV, the interactions are simulated as deep-inelastic scattering. For single-meson production, the axial vector mass M_A is set to be 1.11 GeV, from experiment [94]. Figures 12 and 13 show the cross sections for charged current and neutral current resonant single-meson production for the calculations and the experimental data.

3.2.3 Deep inelastic scattering

Occasionally the neutrino scattering will create multiple pions, particularly at higher energies. For low masses ($W < 1.3$GeV), multiple pion cross sections are calculated with the Rein and Seghal model previously mentioned. For larger masses the cross sections are found

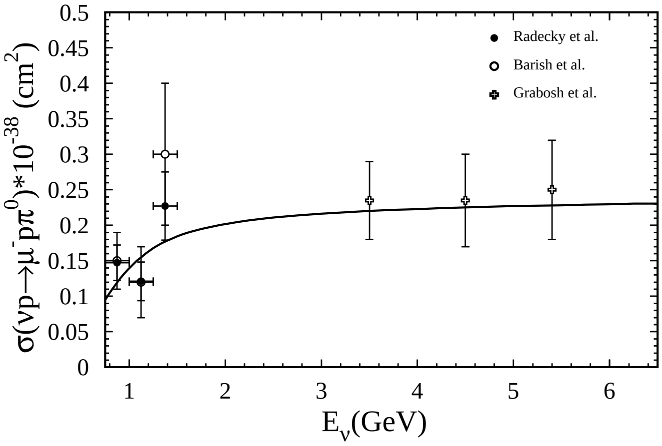

Figure 13: Total cross section for the $\nu_\mu + n \rightarrow \mu^- + p + \pi^0$ process plotted versus the incoming neutrino energy,figure taken from [98] .

assuming deep inelastic scattering (fragmented target and transformed into other particles) using the GRV94 [102] parton distribution functions. The cross section of charged current deep inelastic scattering is calculated by integrating the following equation in the range of the invariant mass $W > 1.3$GeV[103]:

$$\frac{d^2\sigma^{\nu,\bar{\nu}}}{dxdy} = \frac{G_F^2 M_N E_\nu}{\pi} \Big(F_2(x,q^2)(1 - y + \tfrac{y^2}{2} + C_1) \pm xF_3(x,q^2)(1 - \tfrac{y}{2} + C_2)y \Big) ,$$

$$C_1 = \frac{y m_l^2}{4 M_N E_\nu x} - \frac{x y M_N}{2E_\nu} - \frac{m_l^2}{4E_\nu^2} - \frac{m_l^2}{2 M_N E_\nu x}, \qquad C_2 = -\frac{m_l^2}{M_N E_\nu x}.$$

where $x = q^2/(2M_N(E_\nu - E_l))$ and $y = (E_\nu - E_l)/E_\nu$ are Bjorken scaling parameters, M_N is the nucleon mass, m_l is the outgoing lepton mass, E_ν and E_l are the energy of incoming neutrino and outgoing lepton in the laboratory frame, respectively. The nucleon structure functions F_2 and xF_3 are taken from GRV94 [102]. In Fig. 14 it is shown the deep inelastic cross sections for $\nu_\mu(\bar{\nu}_\mu) + N \rightarrow \mu^-(\mu^+) + X$ as a function of neutrino energy.

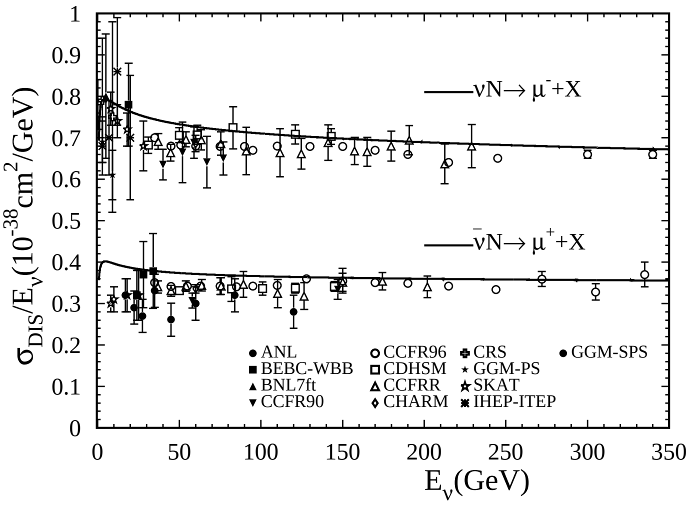

Figure 14: Deep inelastic cross section for the $\nu_\mu + N \rightarrow \mu^- + X$and $\bar{\nu}_\mu + N \rightarrow \mu^+ + X$ plotted versus the incoming neutrino energy with the normalization of $1/E_\nu$. Figure taken from [105]

The theoretical background of the relevant interactions occurring in the SK detector are as described above. Rather than modeling these from scratch, we use, and modify according to our own needs the existing computer code NEUGEN [104]. NEUGEN (Neutrino Event Generator) is a neutrino event generator and cross section library that simulates neutrino-nucleus interactions. This code is commonly used to simulate neutrino scattering by various experimental groups, giving us confidence in the values of the cross sections we use.

3.3 Classification of Atmospheric Neutrino Data

Let me make a short summary of the experiment: First of all, we have a neutrino source, we have the expected flux of neutrinos arriving at the detector, and finally we have the detector. Inside the detector the neutrinos interact in different ways, as mentioned above. A result of these interactions is the production of new particles, mainly leptons. It is the detection of the produced particles that is used as a signature of a neutrino interaction

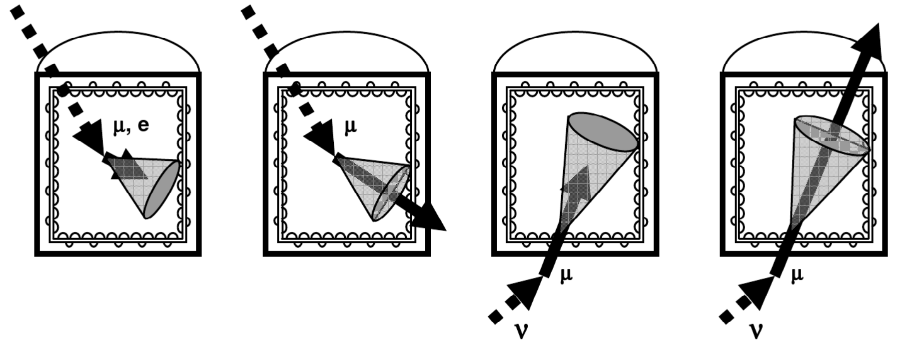

Fully Contained (FC)

Partially Contained (PC)

Upward stopping μ

Upward through-going μ

Figure 15: Super Kamiokande Event Classification

event. Notice that the detection of neutrinos is indirect. The neutrino creates a particle, the particle is detected and a theoretical model is required to infer properties of the neutrino from the measured properties of the created particle. These created particles are detected by the Cherenkov radiation they produce when propagating through water. The Cherenkov radiation is detected as rings of light by photomultiplier tubes located on the walls of the detector. In addition, the Super Kamiokande detector has an inner and outer detector. This allows the separation of events with particles remaining in the interior of detector and events with particles leaving the detector. Among all the features that the Super Kamiokande detector has, we need to make emphasis in its capability to detect neutrinos coming from all directions which is crucial as the distance L varies from the diameter of the Earth $\sim$ 13000 km, to the distance to the upper atmosphere $\sim$ 15 km. In addition, the recent experimental analysis has been done with finer energy resolution. This improves the determination of the atmospheric neutrino mass. Events are classified into two categories Contained Events and Upward Going Events as described next.

3.3.1 Contained Events

Contained events are when the neutrino interacts with the water in the detector to produce a particle. If a single particle is produced, there will be a single Cherenkov ring detected. This are termed “single ring”events. Production of more than one particle will create more than one ring and hence this events are called “multi ring ”events. Contained events are further classified as follows (see Fig. 15 for a schematic view):

Fully Contained Events

Fully contained (FC) events provide the greatest amount of information in the SK experiment. A fully contained event occurs when a neutrino enters Super-K and interacts with the water in the inner detector. The interaction creates a charged particle that recoils through the detector and generates Cherenkov light which gets captured by the photomultiplier tubes (PMTs). Having insufficient energy to exit the inner detector and the particle comes to a stop within the detector. This situation is termed a fully contained event. The median energy for this type of event is about 1 GeV The fully contained events are further divided according to the visible energy into Sub-GeV ($E_{vis} < 1.3GeV$) events and Multi-GeV ($E_{vis} > 1.3GeV$) events. The Cherenkov ring patterns produced by electrons and muons are significantly different such that electrons ($e^{\pm}$) and muons ($\mu^{\pm}$) can be distinguished. Because electrons are very light, they do not travel far in the water before being knocked off course, often radiating a high-energy gamma ray (photon). Each photon likewise travels only a short distance before splitting into an electron/anti-electron pair, with each secondary particle heading in a slightly different direction than the original electron. This process is known as an electromagnetic “shower”. As a result, a single high-energy electron eventually generates hundreds of low-energy electrons, each of which travels only a short distance and makes its own faint Cherenkov ring. It is the sum of the rings from these many short, divergent tracks which is recorded by the PMT’s, hence a blurred, diffuse Cherenkov pattern is observed. On the other hand, muons are much heavier than electrons, and hence do not get knocked off course. Instead, they maintain their initial direction and travel a distance roughly proportional to their initial energy before stopping. The Cherenkov pattern of a muon corresponds much more closely to the ideal case. Tests with real electrons and muons, as well as simulated data, show that the probability of mistaking an electron for a muon (or vice versa) is less than 2%. Without a magnetic field, the detector cannot distinguish between an e^+ and e^- or a μ^+ and μ^-. This means that the neutrino creating the lepton cannot be distinguished from an anti-neutrino. The data is thus summed over $\nu_e + \overline{\nu_e}$ called “e-like”event and summed over $\nu_\mu + \overline{\nu_\mu}$, called “μ-like”event.

Partially Contained Events

Similar to a FC event, a neutrino enters the inner detector and interacts, but in this case the energy is large enough to allow the created particle to exit the inner detector and enter the outer detector. The majority of PC events are muons, as electrons in the water quickly shower their kinetic energy via further interactions or Bremsstrahlung. These events have a median energy of about 10 GeV or typically 10 times higher than that of fully contained events.

3.3.2 Upward going Events

Neutrinos can also interact outside the detector, in the surrounding rock. If they are muon neutrinos, the resulting muon can penetrate the rock and be detected in Super-K. Muons from interactions above the detector cannot be sorted out from the continuous rain of muons created in cosmic ray showers in the atmosphere. Muons coming from below can only be due to neutrino interactions. This is so because cosmic ray muons cannot make it through from the other side of the Earth. However, muons are very penetrating particles, and thus might be produced by a neutrino interaction quite some distance from the detector. Thus, the effective target volume for observing neutrino interactions using upward going muons is much larger than the detector itself, and grows with the energy of the neutrino (since higher energy neutrinos produce higher energy muons, which can travel through more rock). This results in the upward going muon data probing a far higher range in energy than the contained event analysis. The penalty paid for this large energy range is that it is not possible to measure the energy of each muon, since it spends only a small fraction of its time in the detector itself. However, if an upward muon stops in the detector

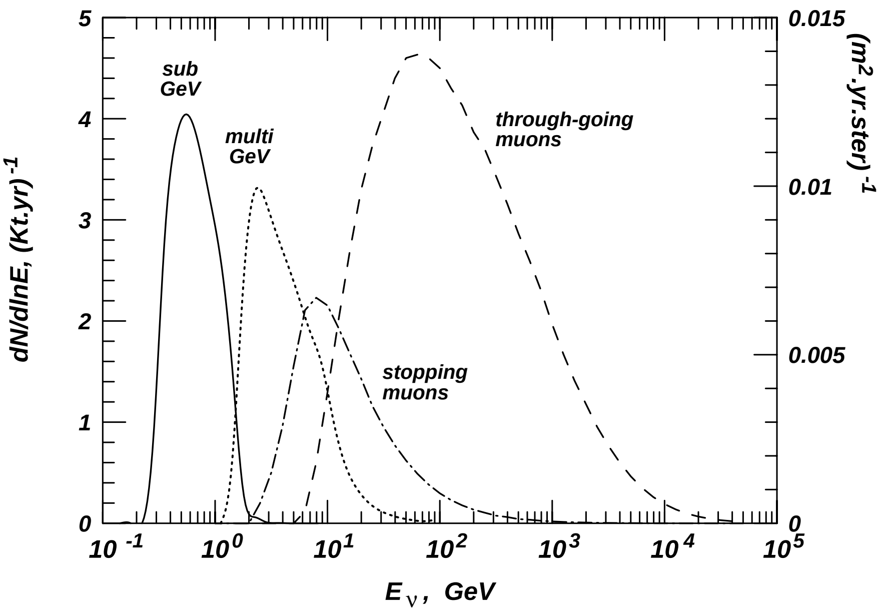

Figure 16: Super Kamiokande Event Spectrum taken from [106]

rather than blasting all the way through, it is likely to have come from a lower energy parent neutrino. Thus, the upward muon sample can be divided into two data sets - a high-energy ”through-going muon” set, and a medium-energy “stopping muon”set. The stopping muon sample are those muons which stop within the detector. They arise from interactions of low energy neutrinos, energies of approximately 10 GeV. The through going sample are muons which pass completely through the detector. These muons are created by high neutrinos with energies of about 100 GeV. In figure 16 we show the theoretical energy distribution for all the neutrino sample observed by the SK experiment.

CHAPTER IV

EXPERIMENTAL SIMULATION II

In this chapter, the procedure used to simulate the experiment is described. First, we start with the contained events, deriving the theoretical model, and thereafter we derive our model for the upward going events

4.1 Simulation: Contained Events

In this section, we derive the basic formula needed to model neutrino oscillation experiments. Atmospheric neutrinos differ from other experiments in that the angle of the created lepton is measured. We start the derivation at the beginning in order to make this more accessible to the non-expert. Start with a neutrino of flavor α ($\alpha = \mathrm{e}, \mu, \tau$) with energy E incident on the detector at an angle θ_ν measured with respect to vertical, $\cos\theta_\nu = 1$ being neutrinos from directly overhead. The Super-K detector is filled with H_2O and the neutrino will scatter and produce a lepton through three reactions as discused above and summarized here. Dominant at low energies and peaking around 0.5 GeV is charge current elastic and quasi-elastic scattering from the proton and from the nucleons in the oxygen,

$$\nu_\alpha + N \to \ell_\alpha + N' \,. \tag{25}$$

Note that the flavor of the lepton matches the flavor of the neutrino, this defines the neutrino type. The charge on the lepton is determined by lepton number conservation. Charge conservation determines the change in the charge between N and N'. For example,

$$\overline{\nu}_e + p^+ \to e^+ + n, \qquad \nu_e + n \to e^- + p^+. \tag{26}$$

Cross sections for scattering off the proton have been explained in Chapter 3.

At intermediate energies, peaking around 1.5 GeV, single pion production dominates.

$$\nu_\alpha + N \to \ell_\alpha + N^*, \qquad N^* \to N' + \pi \ . \tag{27}$$

At higher energies and momentum transfers, the natural degrees of freedom become the quarks and gluons. Deep inelastic scattering begins to rise around 1 GeV and dominates above 10 GeV. Graphs and data for the various cross sections were given in chapter 3.

The detector will detect the produced lepton ℓ through the Cherenkov light that it radiates. Thus we need the inclusive cross section, the cross section summed and integrated over all final particles except the lepton

$$\nu + N \rightarrow \ell + X \ . \tag{28}$$

We must include the cross section depending on the type of neutrino event being study (proton, bound neutron/proton) labeled j,

$$\frac{d^3\sigma_\alpha(E_\nu;\, E_\ell,\, \cos\theta_s)}{dE_\ell\, d\cos\theta_s\, d\phi_s}, \tag{29}$$

where E_ℓ is the energy of the produced lepton, θ_s and ϕ_s are the zenith and azimuthal scattering angles of the lepton as measured from the direction of the neutrino. The cross section $d^3\sigma_\alpha/dE_\ell\, d\cos\theta_s\, d\phi_s$ is the differential cross section for a neutrino of flavor α, interacting with target particles. Note its units are area/energy.

We then need the flux of neutrinos incident on the target as a function of the neutrino energy E_ν and zenith angle of the neutrino θ_ν given by $d^2\, \Phi_\alpha(E_\nu, \cos\theta_\nu)/dE_\nu\, d\cos\theta_\nu$. The Earth's magnetic field introduces a small dependence on the azimuthal neutrino angle ϕ_ν. We utilize the ϕ_ν integrated flux. If we multiply the flux by the cross section, Eq. 29, integrate over the incident neutrino's energy, E_ν, and its zenith angle, $d\cos\theta_\nu$, and integrate over the detected leptons, E_ℓ and their angles $d\cos\theta_\ell\, d\phi_\ell$ we get, for no oscillations,

$$\begin{aligned} N_\alpha &= N\ T \int dE_\nu \int d\cos\theta_\nu \int dE_\ell \int d\cos\theta_s \int d\phi_s \\ &\times\ \varepsilon(E_{vis})\, \frac{d^2\, \Phi_\alpha(E_\nu, \cos\theta_\nu)}{dE_\nu\, d\cos\theta_\nu}\ \frac{d^3\sigma_\alpha(E_\nu;\, E_\ell,\, \cos\theta_s)}{dE_\ell\, d\cos\theta_s\, d\phi_s}\ , \end{aligned} \tag{30}$$

where N is the total number of target nucleons and T the experimental running time. For $\varepsilon(E_{vis}) = 1$, N_α is the number of neutrino events of a given flavor α that are produced in the detector. However, the detector is not one hundred percent efficient. Thus, to get the total number of neutrino events of a flavor α that are actually detected, we have inserted the detection efficiency, $\varepsilon(E_{vis})$, which we assume depends only on the visible energy E_{vis} . This efficiency term plays an important role in the determination of the number of neutrino events. The efficiency functions will be derived later in this chapter as these values are not provided by the Super Kamiokande collaboration.

The detector detects the Cherenkov light emitted by the lepton while traveling through H_2O. The emission of Cherenkov light is independent of the sign of the charge of the lepton. Thus an e^+ (μ^+) cannot be distinguished from a e^- (μ^-). The $e^\pm$ can be distinguished from the $\mu^\pm$ by the fuzziness of the ring of light detected as explained earlier. What is being measured is thus the sum of the electron neutrino and anti-neutrino $\nu_e + \overline{\nu}_e$, or the sum of the muon neutrino plus anti-neutrino $\nu_\mu + \overline{\nu}_\mu$, which are termed "e-like" or "μ-like" events. The symbol α thus needs to be reinterpreted as e-like or μ-like.

So far, we have assumed no oscillations. To include oscillations, we introduce the rate at which a neutrino originates in state α but is in state β when detected, $N_{\alpha\to\beta}$. This requires only that we insert the oscillation probability into Eq. 30,

$$\begin{aligned} N_{\alpha\to\beta} &= N\,T \int dE_\nu \int d\cos\theta_\nu \int dE_\ell \int d\cos\theta_s \int d\phi_s \\ &\times\ \varepsilon(E_{vis})\,\frac{d^2\,\Phi_\alpha(E_\nu,\cos\theta_\nu)}{dE_\nu\,d\cos\theta_\nu}\,\tilde{\mathcal{P}}_{\alpha\beta}(E_\nu,\,cos(\theta_\nu))\,\frac{d^3\sigma_\beta(E_\nu;\,E_\ell,\,\cos\theta_s)}{dE_\ell\,d\cos\theta_s\,d\phi_s}\ . \end{aligned} \tag{31}$$

Note that for a fixed angle $\cos\theta_\nu$ the distance L from the point of creation [107] in the atmosphere to the point of detection is not unique. The distance L depends on the height h in the atmosphere where the neutrino is created. L is given by, for fixed $\cos\theta_\nu$,

$$L = \sqrt{R^2\,\cos^2\theta_\nu + h\,(2R+h)} - R\,\cos\theta_\nu\ , \tag{32}$$

where R is the radius of the Earth and h is the vertical height above the ground. The oscillation probability $\tilde{\mathcal{P}}_{\alpha\beta}(E_\nu,\,cos(\theta_\nu))$ is related to the oscillation probability $\mathcal{P}_{\alpha\beta}(L/E_\nu)$ for a given distance L by

$$\tilde{\mathcal{P}}_{\alpha\beta}(E_\nu,\,cos(\theta_\nu)) = \int_0^\infty dh\,\mathrm{P}_\beta(h,E_\nu)\,\mathcal{P}_{\alpha\beta}(L(h,\cos\theta_\nu)/E_\nu) \tag{33}$$

where $\mathrm{P}_\beta(h,E_\nu)$ is the normalized probability that a neutrino of flavor β and energy E_ν is created at a height h.

Production Height

The production height of atmospheric neutrinos depends on various factors. For instance the energy of the incident cosmic rays and zenith angle. This has been studied by Gaisser and Stanev [107], who have performed Monte Carlo simulations of the cosmic ray interaction in the atmosphere, in order to estimate the slant distance for different neutrino zenith angles as function of the neutrino energy.

A unique feature of the Super-K atmospheric experiment is that it measures the direction of the neutrino event as well as the visible energy E_{vis}, this visible energy varies depending on the type of neutrino event, so we will explain this later in this chapter. At high energies the production cross section is forward peaked so that there is a strong correlation between the lepton direction and the incident neutrino direction. This is much less so at the lower energies. The data is binned into ten equal bins in $\cos\vartheta$, with ϑ the zenith angle of the neutrino event. The dependence of L on $\cos\theta_\nu$, the zenith angle of the neutrino, is pictured in Fig. 17. Notice that the distance L is related to the zenith angle $\cos\theta_\nu$ in a vary nonlinear way. In particular, over the two bins centered around horizontal, $\cos\theta_\nu = 0$, the distance L changes from 73 km at $\cos\theta_\nu = 0.2$ to 2600 km at $\cos\theta_\nu = -0.2$, a factor of 36. When the oscillation phase ϕ ($\phi_{ij} = 1.27\Delta m^2_{ij}L/E$), is $\pi/2$, the oscillation probability $\mathcal{P}_{ee}(\Delta m^2, L/E)$ is at its first minimum. For a typical energy E of 1 GeV and the extracted atmospheric mass-squared difference of $\Delta m^2 = 2.5 \times 10^{-3}$ eV^2, this occurs at a distance of 530 km. This corresponds to an angle $\cos\theta_\nu = -0.02$, nearly horizontal. Thus, the important data for determining the mass-squared difference Δm^2 lies within the two bins near the horizontal where the uncertainty in determining L from $\cos\theta_\nu$ is maximum. Combining this with the fact that what is measured is the neutrino event angle measured from the vertical, $\cos\vartheta$, which through the scattering angle is different from the incident neutrino angle, particularly at low energies, gives an inherent limit on how well atmospheric data can measure the atmospheric mass-squared difference.

The data is binned in E_{vis} and $\cos\vartheta$. For the energy bin, we simply restrict the energy interval, by inserting a Heaviside function in the integral

$$\Theta(E_{vis}^{m,max} - E_{vis}) * \Theta(E_{vis} - E_{vis}^{m,min}) \tag{34}$$

where $E_{vis}^{m,min}$ ($E_{vis}^{m,max}$) is the minimum (maximum) value of E_{vis} for bin m.

The angular binning is less direct. The angular binning is done in $\cos\vartheta$, the zenith angle of the lepton as measured with respect to vertical, this angle is expressed in terms of $\cos\theta_\nu$,

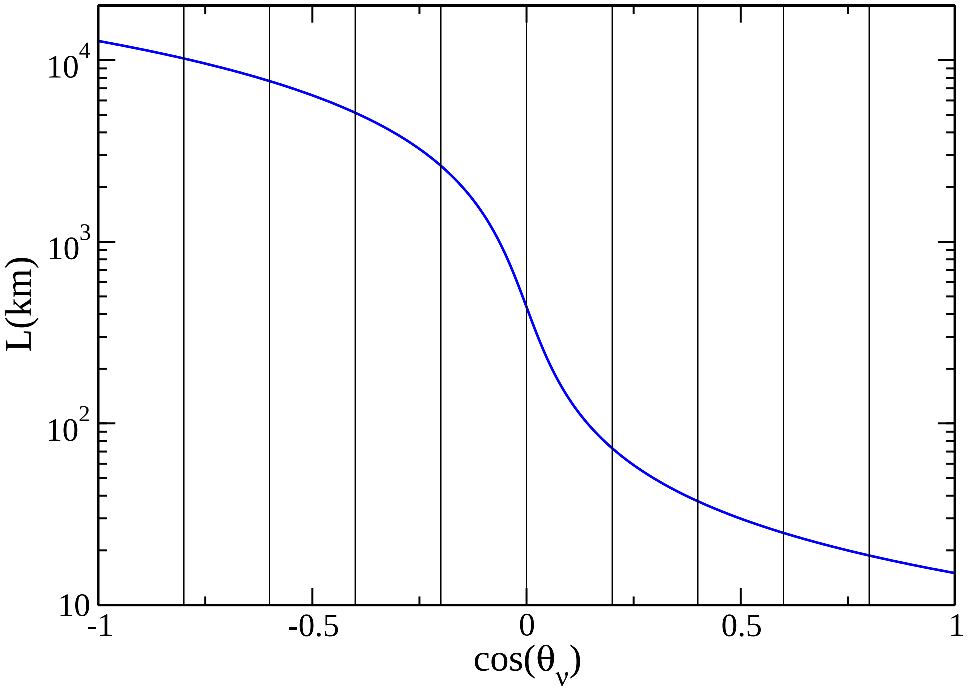

Figure 17: (Color online) The distance L a neutrino travels from its point of creation at a height $h = 15$ km and zenith angle θ_ν as a function of $\cos\theta_\nu$. The vertical lines delineate the angular bins of the data.

$\cos\theta_s$, and ϕ_s. Of course, $\cos\vartheta$ is a function of $\cos\theta_\nu$, $\cos\theta_s$, and ϕ_s. The exact expression and more details will be given later in this chapter.

The binning can be performed by numerically integrating over the full angular space of $\cos\theta_s$ and ϕ_s with Heaviside functions Θ inserted, where $\Theta(x)$ is zero for $x < 0$ and one for $x > 0$. We insert $\Theta(\cos\vartheta^{n,max} - \cos\vartheta)$ and $\Theta(\cos\vartheta - \cos\vartheta^{n,min})$ to restrict ϑ to bin n. This gives the number of neutrinos that are created as type α and then detected as neutrinos of type β in energy bin m and angular bin n,

$$\begin{aligned} N^{nm}_{\alpha\to\beta} &= N\,T \int dE_\nu \int d\cos\theta_\nu \int dE_\ell \int d\cos\theta_s \int d\phi_s \\ &\times\ \varepsilon(E_{vis})\,\frac{d^2\,\Phi_\alpha(E_\nu,\cos\theta_\nu)}{dE_\nu\,d\cos\theta_\nu}\,\tilde{\mathcal{P}}_{\alpha\beta}(E_\nu,\,cos\theta_\nu)\,\frac{d^3\sigma_\beta(E_\nu;\,E_\ell,\,\cos\theta_s)}{dE_\ell\,d\cos\theta_s\,d\phi_s} \\ &\times\ \Theta(\cos\vartheta^{n,max} - \cos\vartheta) * \Theta(\cos\vartheta - \cos\vartheta^{n,min}) \\ &\times\ \mathit{\Theta}(E^{m,max}_{vis} - E_{vis}) * \mathit{\Theta}(E_{vis} - E^{m,min}_{vis})\ . \end{aligned} \tag{35}$$

Finally, the absolute number of neutrino events of type α detected, independent of whether they originate as type α or type β is given by

$$N_{\alpha}^{nm} = N_{\alpha\to\alpha}^{nm} + N_{\alpha\to\beta}^{nm} \ . \tag{36}$$

This result, Eqs. 35 and 36, constitute what we will term an exact calculation, in the sense that the results would be exact if the inputs were all known exactly. Although written in a different form, this result is equivalent to the results utilized in Refs. [108] and [109], for example.

4.1.1 Energy and Direction Reconstruction

So far we have followed the standard procedure to calculate the number of contained neutrino events occurring at the detector. However there are a few difficulties we need to overcome to perform an actual calculation. These are:

- The meaning of “Visible Energy ”
- The meaning of “Neutrino Event Angle ”
- A good estimate of the efficiencies.

As noted earlier contained events are classified as fully contained events and partially contained events. Then fully contained events are further separated into single ring events and multi ring events. In the fully contained single ring events we only have one particle (lepton) propagating after the neutrino interaction and therefore it is straightforward to determine the “visible energy ”and direction of the neutrino event. However for the multi ring and partially contained events the reconstruction of the “visible energy ”becomes indirect and difficult to implement. We utilize some of the Monte Carlo results available from the SK collaboration and use them as a means to estimate the visible energy E_{vis} and neutrino event direction $\cos\vartheta$.

Energy Reconstruction for Fully Contained Single Ring Events

The visible energy for the fully contained single ring events is equivalent to the energy of the produced lepton.

$$E_{vis} = E_{lepton} \tag{37}$$

Energy Reconstruction for Fully Contained Multi Ring Events

For the multi ring events the visible energy is reconstructed by adding the energy of all the rings that are created, in this case pions for μ-like events, and electrons for e-like events, plus the created lepton according to [110].

$$E_{vis} = E_{lepton} + \sum_{i=2}^{n} (E_{\pi}^{i} \quad or \quad E_{e}^{i}). \tag{38}$$

Energy Reconstruction for Partially Contained Events

For the partially contained events , the visible energy is calculated by adding the following terms:

$$E_{vis} = E_{inner} + E_{dead} + E_{anti} \tag{39}$$

with E_{inner} is the total energy of the charged particle observed in the inner detector, E_{dead} is the energy deposited in the region between the inner detector and the outer detector and E_{anti} is the energy deposited in the outer detector.

Reconstruction of the Neutrino Event Direction

The direction of a fully contained single ring and partially contained event is simply the direction of the created lepton, which is a function of the neutrino scattering angle $\cos\theta_s$, the scattering polar angle ϕ_s, the neutrino azimuthal angle $\cos\theta_\nu$ and can be expressed as

$$\cos\vartheta = \cos\theta_s \, \cos\theta_\nu - \sin\theta_s \, \sin\theta_\nu \, \cos\phi_s \ . \tag{40}$$

For the multi ring sample, the direction assigned to each neutrino event is estimated as the sum of the momentum weighted directions summed over all identified rings. The zenith angle is reconstructed as

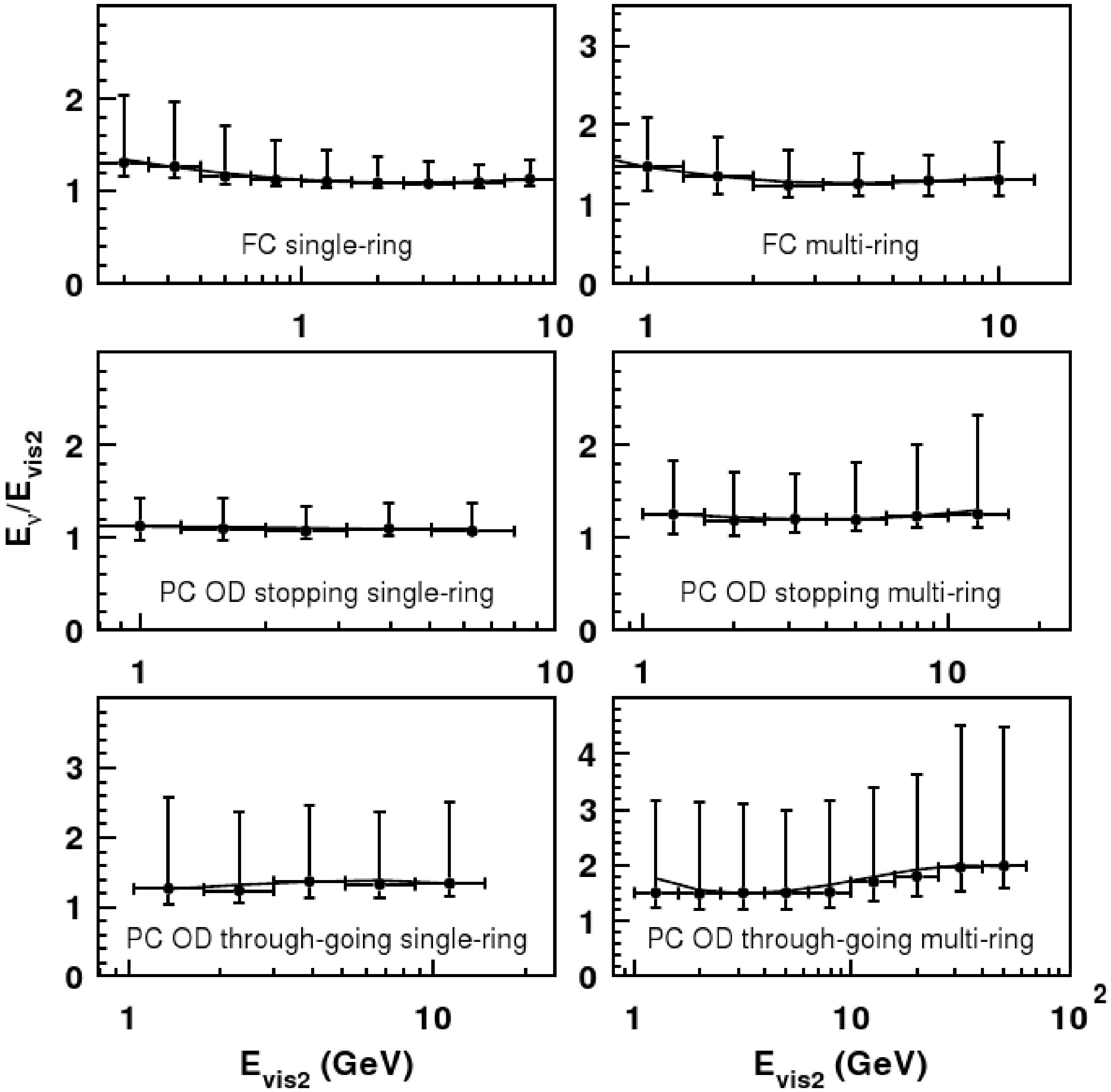

Figure 18: Monte Carlo Simulation of the relation between E_{vis} and E_ν taken from [110]

$$\cos\vartheta = \cos\vartheta_{sum} \tag{41}$$

$$\overrightarrow{d}_{sum} = p_\mu \cdot \overrightarrow{d_1} + \sum_{2}^{n}(p_\pi \quad or \quad p_e) \cdot \overrightarrow{d}_i \tag{42}$$

where n is the number of rings, p_μ, p_π and p_e are the momentum of charged particles, $\overrightarrow{d}_i$ is the direction of the i ring, and $\overrightarrow{d}_{sum}$ and $\cos\vartheta_{sum}$ are the direction and the cosine of the zenith angle of the momentum weighted vector sum, respectively.

Using Monte Carlo Results

We have given above the procedure followed by the SK collaboration to reconstruct energies. However, this procedure can be done only for the fully contained single ring event sample. The multi-ring events cannot be easily modeled given the kinematics of a process in which several particles are produced in the final state. Similarly we cannot easily estimate E_{inner}, E_{dead} and E_{anti} for the partially contained events. However, we can use the Monte Carlo Results given by the SK collaboration [69] to estimate the visible energy. Figure 18 in [110] gives the result of Monte Carlo simulation in which the ratio E_ν/E_{vis} is plotted as a function of logE_{vis} for all the data samples. Utilizing these curves we are able to translate E_ν to E_{vis} and vise versa.

We use a similar method to determine the event direction. We can use the Monte Carlo simulation to estimate the average scattering angle, and then use Eq. 40 to determine the event direction. We show the average scattering angle as a function of the lepton momentum in Figure 19 taken from [111]. However this can only be applied to fully contained single ring event and partially contained events for which we have only one particle emitting a Cherenkov ring. The multi ring sample becomes a real challenge since implementing equation 41 and 42 in our program is practically impossible. For the multi-ring sample, unlike the single ring case, we don't have a single scattering angle with respect the neutrino direction, instead we have several particle being produced and thus several scattering angles. The procedure used by the SK collaboration described earlier, estimates a single direction of this multiparticle

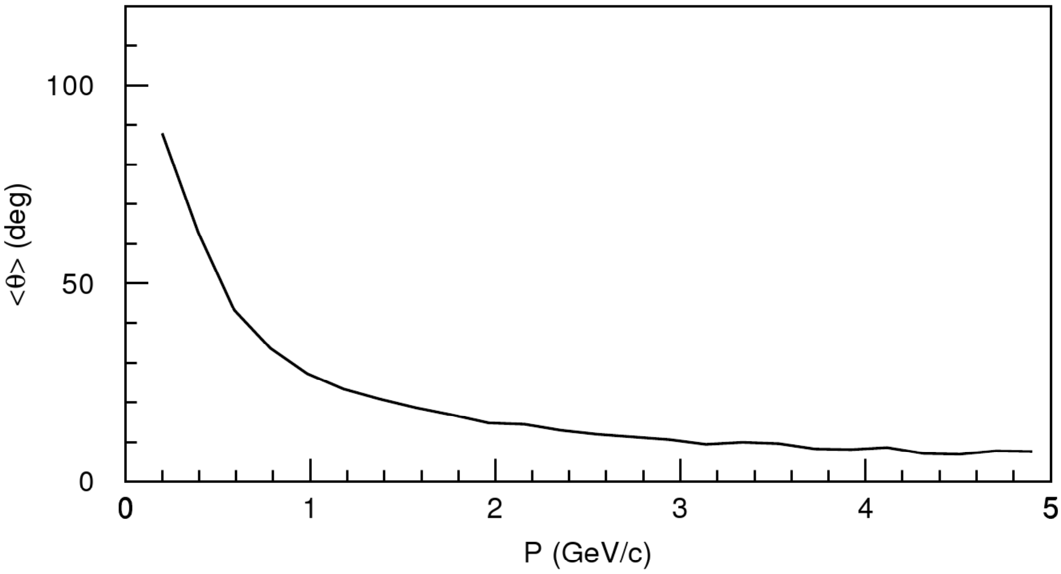

Figure 19: Monte Carlo simulation of the scattering angle with respect to the incident neutrino direction taken from [111]

neutrino event. We implement a naive method in which we defined an average scattering angle for each energy bin, we used the SK monte carlo simulation in the absence of oscillation to estimate this average scattering angle and finally we use Eq. 40 to determine the event direction.

Determining Efficiencies

Here we describe a method to determine the efficiencies of the SK detector. The efficiency $\varepsilon(E_{vis})$ is an intrinsic property of the detector and is assumed to depend on the visible energy of the detected particle, E_{vis}. The most recent data uses a finer energy binning [69] than was for previous publications [48]. No efficiency information is available for this new binning. We need a method to somehow obtain this information. We start with our Eq. 35 and the assumption of no oscillations, $\tilde{\mathcal{P}}_{\alpha\alpha} = 1$ and $\tilde{\mathcal{P}}_{\alpha\beta} = 0$. We can integrate over all angular variables and leave just the integral over energies. Therefore the expected number of neutrino no oscillation events in the energy bin m is given by

$$\begin{aligned} N_\alpha^m &= N\,T \int dE_{vis} \int dE_\nu \\ &\times\ \varepsilon(E_{vis})\, \frac{d\,\Phi_\alpha(E_\nu)}{dE_\nu}\, \frac{d\sigma_\alpha(E_\nu;\,E_\ell)}{dE_\ell} \\ &\times\ \Theta(E_{vis}^{m,max} - E_{vis}) * \Theta(E_{vis} - E_{vis}^{m,min})\ . \end{aligned} \tag{43}$$

We approximate the value of the efficiency $\varepsilon(E_{vis})$ as constant over the energy bin m. This is more reasonable due to the smallness of the new energy binning; if the efficiency is constant we can take it out of the integral and name it $\overline{\varepsilon(m)}$ and have

$$\begin{aligned} N_\alpha^m &= \overline{\varepsilon}(m)\, N\,T \int dE_{vis} \int dE_\nu\, \frac{d\,\Phi_\alpha(E_\nu)}{dE_\nu}\, \frac{d\sigma_\alpha(E_\nu;\,E_\ell)}{dE_\ell} \\ &\times\ \Theta(E_{vis}^{m,max} - E_{vis}) * \Theta(E_{vis} - E_{vis}^{m,min})\ . \end{aligned} \tag{44}$$

We are almost finished, we just need to to use one more time the experimental information available [69]. In this case we will use the Monte Carlo no oscillation number of events as our N_α^m in Eq. 44, call them $N_\alpha^{MC}(m)$, to give for $\overline{\varepsilon}(m)$

$$\overline{\varepsilon}(m) \;=\; \frac{N_\alpha^{MC}(m)}{N\,\int dE_{vis} \int dE_\nu\, \frac{d\,\Phi_\alpha(E_\nu)}{dE_\nu}\, \frac{d\sigma_\alpha(E_\nu;\,E_\ell)}{dE_\ell} \Theta(E_{vis}^{m,max} - E_{vis}) * \Theta(E_{vis} - E_{vis}^{m,min})} \tag{45}$$

This provides all the necessary ingredients to model the contained events in a qualitatively yet numerically efficient way.

4.2 Simulation:Upward Going Muons

The next data sample to be modeled is the upward going muon events, which as we said before consists of the muons created by neutrino interactions outside the detector. In order to search for neutrino oscillations using the upward through going muon, we need to compare the observed upward going muon flux with the expected one calculated numerically. In this case, we used a method of numerical calculation that has been applied for various experiments that have studied the same phenomenon.

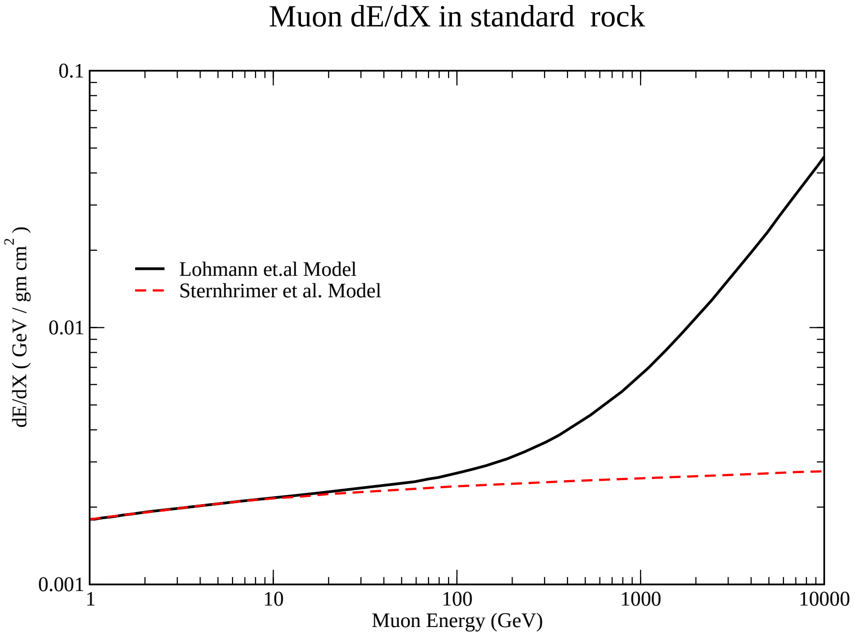

Figure 20: Energy loss dE/dx of muons in standard rock.

4.2.1 Calculation of Upward Through Going Muon Flux

As described earlier, the upward through going events are muons produced in the rocks surrounding the SK detector, which then travel completely through the detector. The experimentally measured quantity is then the energy and angular dependence of this muon flux, the quantity we must model. To model this flux we require the following quantities:

- The atmospheric muon neutrino flux
- The charged current cross section between neutrino and nucleon
- The muon range in the rock

In the following calculation and given the relevant neutrino energy, we approximate the neutrino event angle as being equal to the lepton zenith angle which, at the same time is assumed to be equal to the neutrino zenith angle. The flux of induced muons which are generated by parent neutrinos of energy E_ν is given by the product of cross section and neutrino flux

$$\frac{d^2\sigma}{dxdy} \cdot \frac{d^2\phi_\nu(E_\nu, \cos\theta_\nu)}{dE_\nu d\cos\theta_\nu}, \tag{46}$$

where $d^2\sigma/dxdy$ is the differential charged current cross section as a function of the Bjorken scaling parameters, x and y. $d^2\phi_\nu(E_\nu, \cos\theta_\nu)/dE_\nu d\cos\theta_\nu$ is the differential spectrum of the parent neutrinos as a function of the neutrino energy, E_ν, and the zenith angle θ_ν. The survival of the muon depends on the range, X, defined as the distance traveled d times the density of the medium, ρ in (g/cm^3), through which the muon is traveling. We define $g(X; E_\mu; E_{th})$ as the probability that a muon generated with a energy of E_μ survives with energy larger than E_{th} after traveling the range X. Then the upward going muon flux at the detector with energy larger than E_{th} is given by

$$\frac{d\phi_\mu(E_{th}, \cos\theta)}{d\Omega} = N_A \int_0^\infty dX \int_{E_{th}}^\infty dE_\mu \int_0^1 dy \int_0^1 dx \frac{d^2\sigma}{dxdy} \frac{d^2\phi_\nu(E_\nu, \cos\theta_\nu)}{dE_\nu d\Omega} g(X; E_\mu; E_{th}), \tag{47}$$

where N_A is avogadro's number and $g(X; E_\mu; E_{th})$ is given by

$$g(X; E_\mu; E_{th}) = \vartheta(R(E_\mu, E_{th}) - X), \tag{48}$$

$R(E_\mu; E_{th})$ is the range of the muons in the rock. The range is the distance that the muon travels while its energy decreases from E_μ to E_{th} in units of g/cm^2, and $\vartheta(x)$ is the Heaviside step function.

The integral over X can be simply replaced by $R(E_\mu; E_{th})$ to give,

$$\frac{d\phi_\mu(E_{th}, \cos\theta)}{d\Omega} = N_A \int_{E_{th}}^\infty dE_\mu \int_0^1 dy \int_0^1 dx \frac{d^2\sigma}{dxdy} \frac{d^2\phi_\nu(E_\nu, \cos\theta_\nu)}{dE_\nu d\Omega} R(E_\mu; E_{th}). \tag{49}$$

Since the neutrino flux and the muon range do not depend on the scaling parameter x, and the integral over y is independent of the neutrino energy spectrum, equation 49 can be rewritten as follows,

$$\frac{d\phi_\mu(E_{th}, \cos\theta)}{d\Omega} = N_A \int_{E_{th}}^\infty \left[\int_0^1 \left[\int_0^1 \frac{d^2\sigma}{dxdy} dx\right] R(E_\mu; E_{th}) dy\right] \frac{d^2\phi_\nu(E_\nu, \cos\theta_\nu)}{dE_\nu d\Omega} dE_\mu. \tag{50}$$

We define a probability function of the form

$$P(E_\nu, E_{th}) = N_A \int_0^1 \left[\int_0^1 \frac{d^2\sigma}{dxdy} dx \right] R(E_\mu; E_{th}) dy, \tag{51}$$

then equation 50 can be written as

$$\frac{d\phi_\mu(E_{th}, \cos\theta)}{d\Omega} = \int_{E_{th}}^{\infty} \frac{d^2\phi_\nu(E_\nu, \cos\theta_\nu)}{dE_\nu d\mathit{\Omega}} P(E_\nu, E_{th}) dE_\mu \tag{52}$$

The function $P(E_\nu, E_{th})$ is interpreted as the probability that the neutrinos of energy E_ν are observed as muons at the detector with energy larger than E_{th}.

Notice that for an oscillation analysis, the mean flux depends on the oscillation parameters, the mass squared difference and the mixing angle. However, $P(E_\nu, E_{th})$ does not depend on the oscillation parameters and can be calculated outside the fitting routine. Because neutrinos and anti-neutrinos have different cross sections, equation 52 should be replace by:

$$\frac{d\phi_\mu(E_{th}, \cos\theta)}{d\Omega} = \\ \int_{E_{th}}^{\infty} \left[\frac{d^2\phi_{\nu_\mu}(E_\nu, \cos\theta_\nu)}{dE_\nu d\mathit{\Omega}} P(E_\nu, E_{th}) + \frac{d^2\phi_{\overline{\nu}_\mu}(E_\nu, \cos\theta_\nu)}{dE_\nu d\mathit{\Omega}} P(E_{\overline{\nu}}, E_{th}) \right] dE_\mu \tag{53}$$

Muon Energy Loss in Rock

Finally, we need $R(E_\mu; E_{th})$, the energy loss of the muons in the rock. High energy muons passing through matter lose energy due to electro-magnetic processes, mainly through ionization, bremsstrahlung, and direct pair production. Figure 20 gives dE/dx for muons in standard rock calculated by Sternheimer [112] and by Lohmann [113]. Then the range can be calculated from dE/dx as follows

$$R(E_\mu, E_{th}) = \int_{E_\mu}^{E_{th}} \frac{-dE}{dE/dx} \tag{54}$$

we use Lohmann's dE/dx to calculate the muon range.

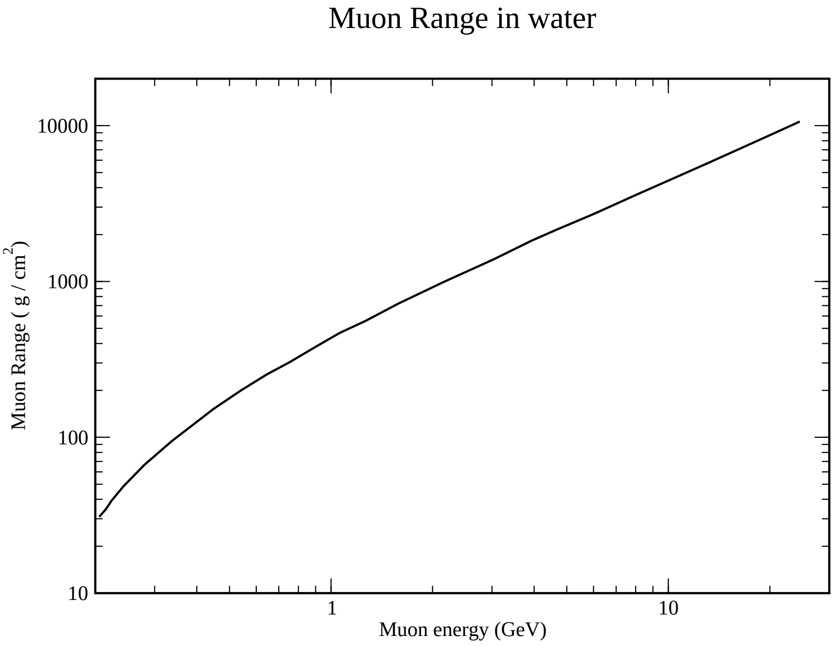

Figure 21: Muon Range in water.

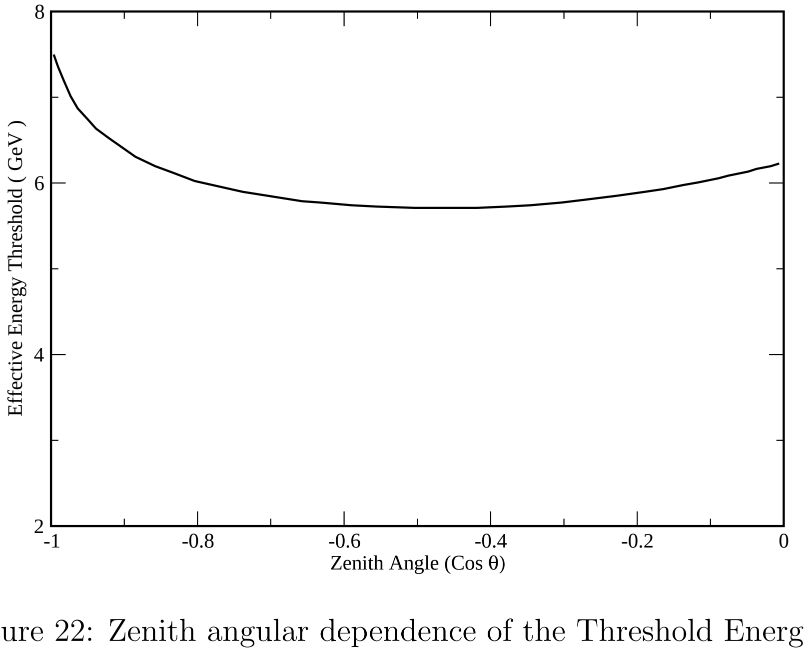

Figure 22: Zenith angular dependence of the Threshold Energy.

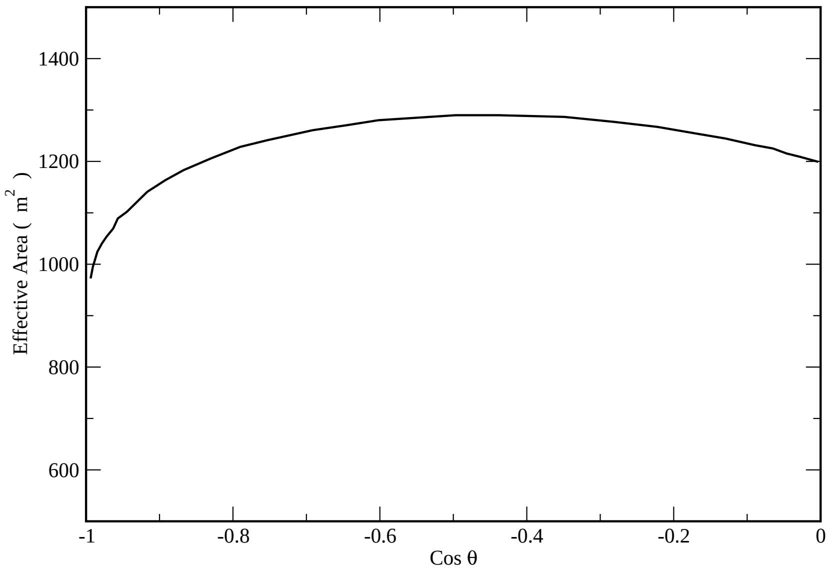

Figure 23: Effective area as function of the zenith angle.

Muon Energy Loss in Water

In order to study the trajectory of upward going muons inside the detector we also need to calculate the energy loss when traveling through water. Figure 21 shows the muon range in water.

Threshold Muon Energy

Equation 53 involves the threshold energy E_{th}. For the upward through going events, E_{th} is the minimum amount of energy needed for a muon to travel through the water in the detector. This can be as small as 7 meters or as large as 50 meters depending on the angle of the incident muon with respect to the vertical. Figure 22 shows the angular dependence of the energy threshold.

Upward through-going muon flux

Finally we can use equation 53 to calculate the expected flux of through-going muons. To do this, we can integrate equation 53 over the energy threshold range which depends on the muon track length, a quantity that varies with the zenith angle. We also need to multiply

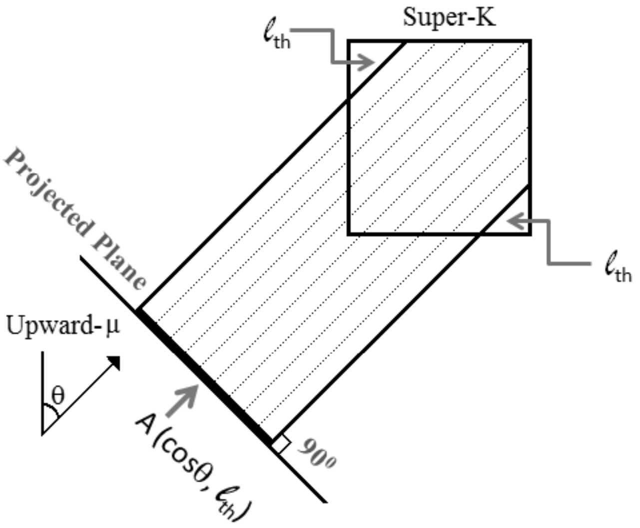

Figure 24: Schematic view of the effective area of the SK detector.

by the effective area of the detector according to,

$$\frac{d\phi^{thr}(\cos\theta)}{d\Omega} = \frac{1}{A(\cos\theta, 7m)} \int_{l_{min}}^{l_{max}} \frac{dA(\cos\theta, l)}{dl} \cdot \frac{d\phi_{\mu}(E_{th}, \cos\theta)}{d\Omega} dl \tag{55}$$

Here $A(\cos\theta, l)$ is the effective area of the detector for the through going muons for a transit distance between l_{max} and l_{min}, see schematic view in figure 24. The zenith angle dependence of the effective area is shown in figure 23.

Upward stopping muon flux

The upward stopping muon flux is calculated by subtracting the upward-through going flux $d\phi^{thr}/d\Omega$ from the $d\phi^{7m}/d\Omega$ which is the muon flux with the track length longer than $7m$, thus we have

$$\frac{d\phi^{stop}(\cos\theta)}{d\Omega} = \frac{d\phi^{7m}(\cos\theta)}{d\Omega} - \frac{d\phi^{thr}(\cos\theta)}{d\Omega} \tag{56}$$

4.2.2 Upward Going Muons and Neutrino Oscillations

So far we have provided the derivation of our method to simulate the atmospheric upward going sample, however we have made no assumption about the existence of neutrino oscillation. In order to incorporate this phenomenon into our simulation we need to modify equation 53 in such a way that we include oscillation probabilities with matter effects. We need to include electron neutrino and electro anti-neutrino that oscillate into muon neutrino and anti-neutrino plus muon neutrino and anti-neutrino which do not oscillate, giving

$$\begin{aligned}
&\frac{d\phi_\mu(E_{th},\cos\theta)}{d\Omega} = \\
&\int_{E_{th}}^{\infty} P(E_\nu, E_{th}) \left[\frac{d^2\phi_{\nu_\mu}(E_\nu,\cos\theta_\nu)}{dE_\nu d\mathit{\Omega}} P_M(\nu_\mu \to \nu_\mu) + \frac{d^2\phi_{\nu_e}(E_\nu,\cos\theta_\nu)}{dE_\nu d\mathit{\Omega}} P_M(\nu_e \to \nu_\mu)\right] dE_\mu \\
+ &\int_{E_{th}}^{\infty} P(E_{\overline{\nu}}, E_{th}) \left[\frac{d^2\phi_{\overline{\nu}_\mu}(E_\nu,\cos\theta_\nu)}{dE_\nu d\mathit{\Omega}} P_M(\overline{\nu}_\mu \to \overline{\nu}_\mu) + \frac{d^2\phi_{\overline{\nu}_e}(E_\nu,\cos\theta_\nu)}{dE_\nu d\mathit{\Omega}} P_M(\overline{\nu}_e \to \overline{\nu}_\mu)\right] dE_\mu.
\end{aligned} \tag{57}$$

Combining this with equations 57 , 55 and 56 we obtain the through going and stopping muon flux respectively in the presence of neutrino oscillations. In equation 57 P_M is the oscillation probability including the earth matter effects. For this we use the procedure developed by [114]. Important differences occur when matter effects are taken into account. In vacuum if CP is conserved we have $P(\nu_\mu \to \nu_\mu) = P(\overline{\nu}_\mu \to \overline{\nu}_\mu)$. While in matter $P_M(\nu_\mu \to \nu_\mu) \neq P_M(\overline{\nu}_\mu \to \overline{\nu}_\mu)$ because matter affects neutrinos and anti-neutrinos differently. Thus even in the case of no fundamental CP violation, upward going data are different for neutrino and anti-neutrino.

CHAPTER V

STATISTICAL ANALYSIS OF ATMOSPHERIC NEUTRINO DATA

Before utilizing our computational model to extract new information, we calibrate our model by comparing its results to those obtained by the SK experimentalist. To do this, we follow the SK experimentalist analysis and introduce the leading term in the subdominant expansion for the oscillation probability,

5.1 Oscillation Analysis

Our goal is to develop a model which incorporates a full three neutrino analysis, an analysis which does not utilize any expansion or approximation to the oscillation probabilities. To compare with the analysis performed by the SK experiment, we can utilize the equations 58 by setting the small mass square difference Δm^2_{21} equal to zero such that in the full analysis code $\Delta m^2_{31} = \Delta m^2_{23} = \Delta m^2$ The SK collaborations include the Earth MSW effect utilizing an approximation taken from [115]. We incorporate the Earth MSW effect for atmospheric neutrinos utilizing the method proposed in [114]. This method allows us to treat the full 3×3 MSW effect exactly as long as the Earth is modeled as composed of layers of constant matter density.

$$\begin{aligned}
\mathrm{P}(\nu_e \to \nu_e) &= 1 - \sin^2 2\theta_{13} \sin^2\left(\frac{1.27\Delta m^2 L}{E}\right) \\
\mathrm{P}(\nu_\mu \to \nu_e) &= \mathrm{P}(\nu_e \to \nu_\mu) = \sin^2\theta_{23}\sin^2 2\theta_{13}\sin^2\left(\frac{1.27\Delta m^2 L}{E}\right) \\
\mathrm{P}(\nu_\mu \to \nu_\mu) &= 1 - 4\cos^2\theta_{13}\sin^2\theta_{23}(1-\cos^2\theta_{13}\sin^2\theta_{23}) \\
&\quad \times \sin^2\left(\frac{1.27\Delta m^2 L}{E}\right) \qquad (58)
\end{aligned}$$

The SK data is divided into 37 energy bins as follows;

- Fully Contained Events: 18 energy bins

  E-like Events: 10 energy bins

  - Sub-GeV e-like Events $E_{vis} < 1.3GeV$: 5 energy bins
  - Multi-GeV e-like Events $E_{vis} > 1.3GeV$: 5 energy bins
- Mu-like Events: 8 energy bins
  - Sub-GeV μ-like Events $E_{vis} < 1.3GeV$: 5 energy bins
  - Multi-GeV μ-like Events $E_{vis} > 1.3GeV$: 3 energy bins

- Fully Contained (FC) Multi-Ring Events: 9 energy bins
  - FC Multi-Ring e-like Events: 5 energy bins
  - FC Multi-Ring μ-like Events: 4 energy bins

- Partially Contained (PC) Events: 8 energy bins
  - PC Stopping Events: 4 bins
  - PC Through Going Events: 4 bins

- Upward Going Muon (UPμ) Events Events: 2 bins
  - Upward Stopping Muons: 1 bin
  - Upward Through Going Muons: 1 bin

- Total=37 bins

In the analysis we performed here the most recent data from [69] is used. The energy bins are divided more finely in this data allowing a greater sensitivity to Δm^2. Each energy bin is further divided into 10 zenith angle bins, from $\cos\theta = 1$ to $\cos\theta = -1$ for the contained sample and from $\cos\theta = 0$ to $\cos\theta = -1$ for the UPμ sample. We have a total number of $37 \times 10 = 370$ bins. In order to determine the oscillation parameters, the model for the SK experiment described earlier gives the theoretical predictions for each bin. We construct a χ^2 function assuming that the experimental data has a Poisson distribution,

$$\chi^2 \; = \; \sum_{n=1}^{370} \left[2 \left\{ \overline{N}_{the}(n) - N_{obs}(n) \right\} + 2 N_{obs}(n) \ln \left(\frac{N_{obs}(n)}{\overline{N}_{the}(n)} \right) \right] + \sum_{i=1}^{43} \left(\frac{\xi_i}{\sigma_i} \right)^2 . \qquad (59)$$

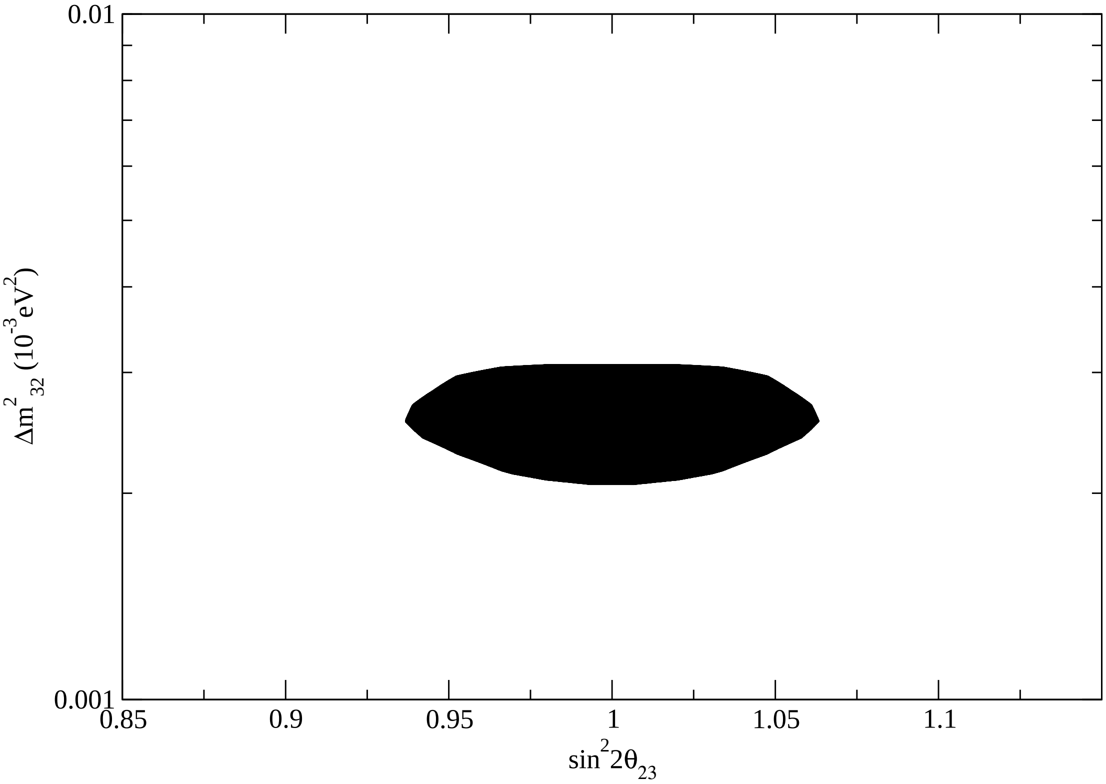

Figure 25: Super Kamiokande 90% CL allowed region for Δm^2 vs $\sin^2 2\theta_{23}$

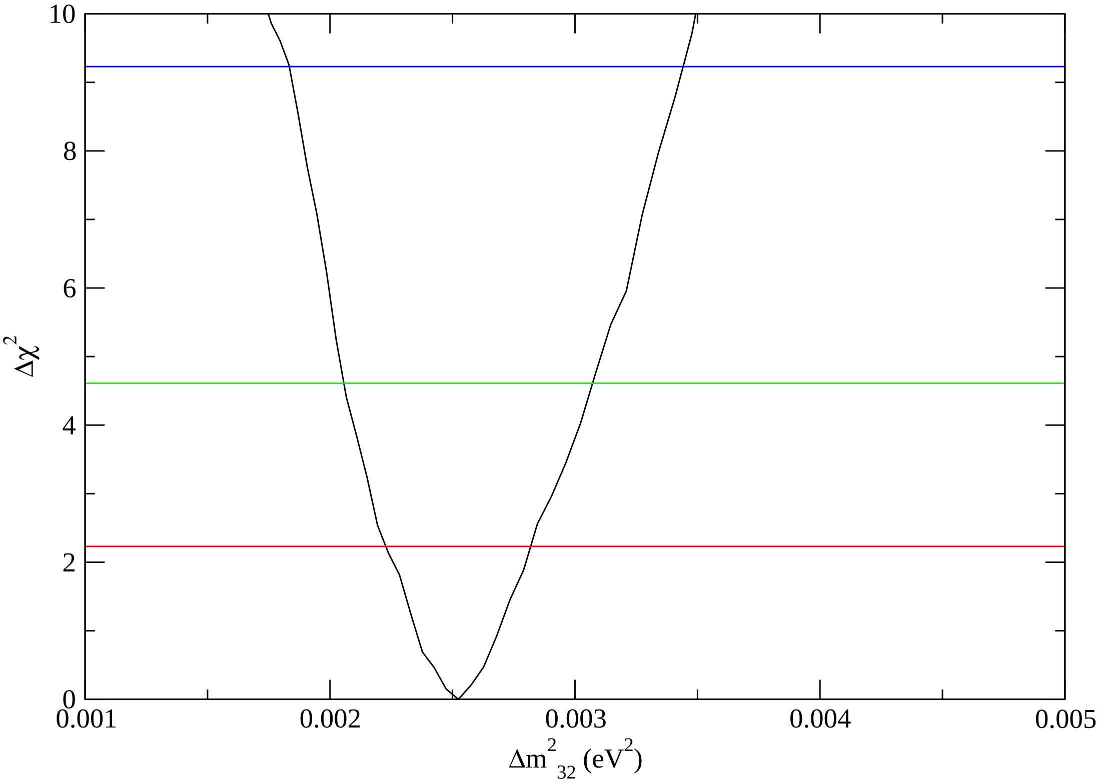

Figure 26: Super Kamiokande χ^2 vs Δm^2

where

$$\overline{N}_{the}(n) = N^{the}(n)\left(1 + \sum_{i=1}^{45} f_i^n \cdot \xi_i\right). \tag{60}$$

In order to treat systematic errors we use the "Pull"approach as described [116]. This approach allows one to incorporate systematic errors without adding adjustable parameters. The approach derives from making linear corrections to the theoretical predictions for each systematic error. The formulas are derived from Gaussian statistics and are approximated for Poisson statistics. In equation 59 and 60, $N_{obs}(n)$ is the number of observed events in the bin n, $N_{th}(n)$ is the theoretical prediction, ξ_i is the systematic error pull for the systematic error, f_i^n is the systematic error coefficient and σ_i is the one sigma value for the systematic error. $\overline{N}_{the}(n)$ accounts for effects of the systematic errors on the theoretical predictions through the pulls ξ_i . Here we use 45 systematic errors arising from different sources as described in tables 2 to 5. For these 45 errors, all of them contributed to the χ^2 except the overall normalization and the normalization for the multi-GeV multi ring sample, which are floated freely. During each fit these 45 ξ_i are varied to minimize χ^2 for a given set of oscillation parameters. The minimization of χ^2 with respect to ξ_i ($\frac{\partial\chi^2}{\partial\xi_j} = 0$) is equivalent to solve numerically 45 coupled equations of the form

$$\frac{\partial\chi^2}{\partial\xi_j} = \sum_{n=1}^{370} f_j^n \left(N_{th}(n) - \frac{N_{obs}(n)}{1 + \sum_{i=1}^{45} f_i^n \cdot \xi_i} \right) + \sum_{i=1}^{43} \frac{\xi_i}{\sigma_i^2}\delta_{ij} = 0 \qquad (61)$$

Solving the 45 non-linear equations is computationally orders of magnitude faster than not using the pull method, which would involve varying 45 parameters.

For the subdominant approximation for the oscillation parameters Eq.58, we minimize the χ^2 function as defined in 59 to find the best fit oscillation parameters given by $(\Delta m^2, \sin^2\theta_{23}, \theta_{13}) = (2.5 \times 10^{-3} eV^2, 0.51, 0.01)$ with an overall $\chi^2 = 416$

We also obtain the allowed regions curves for different oscillation parameters. The 90% confidence level allowed region for Δm^2 vs $\sin^2 2\theta_{23}$ is shown in figure 25, which is obtained by calculating $\chi^2 - \chi^2_{min} = 4.6$. From here on, all curves shown are the result of our computer simulation. In figure 26, 27 and 28 we also plot χ^2 curves versus each individual parameter Δm^2, $\sin^2\theta_{23}$, and θ_{13}. From these curves we can see that $2.1 \times 10^{-3} eV^2 < \Delta m^2 < 3.1 \times 10^{-3} eV^2$, $0.938 < \sin^2 2\theta_{23}$ and $-0.38 < \theta_{13} < 0.38$ are allowed at 90 % confidence level.

Table 2 and 3 provide the number of events observed by the SK experiment corresponding to the FC, PC and UPμ sample. In Table 4 and 5 we show the Monte Carlo expected events for the no oscillation case. Numbers I, II, ... X are used to label the zenith angle bins $-1 < \cos\Theta < -0.8$, $-0.8 < \cos\Theta < -0.6$, ... and $0.8 < \cos\Theta < 1.0$ respectively for FC and PC events, $-1 < \cos\Theta < -0.9$, $-0.9 < \cos\Theta < -0.8$, ... and $0.1 < \cos\Theta < 0.0$ respectively for upward stopping and through-going muon events. The numbers 1 to 5 in the E_{vis} column correspond to the momentum ranges <250, 250-400, 400-630, 630-1000 and >1000 MeV/c for sub-GeV samples and the numbers 6 to 10 correspond to <2.5, 2.5-5.0, 5.0-10, 10-20 and $> 20 \sim$ GeV/c for multi-GeV samples. The letters a to f in the E_{vis} columns correspond to energy ranges 0.2-1.33, 1.33-2.5, 2.5-5.0, 5.0-10, 10-20, $> 20 \sim$GeV.

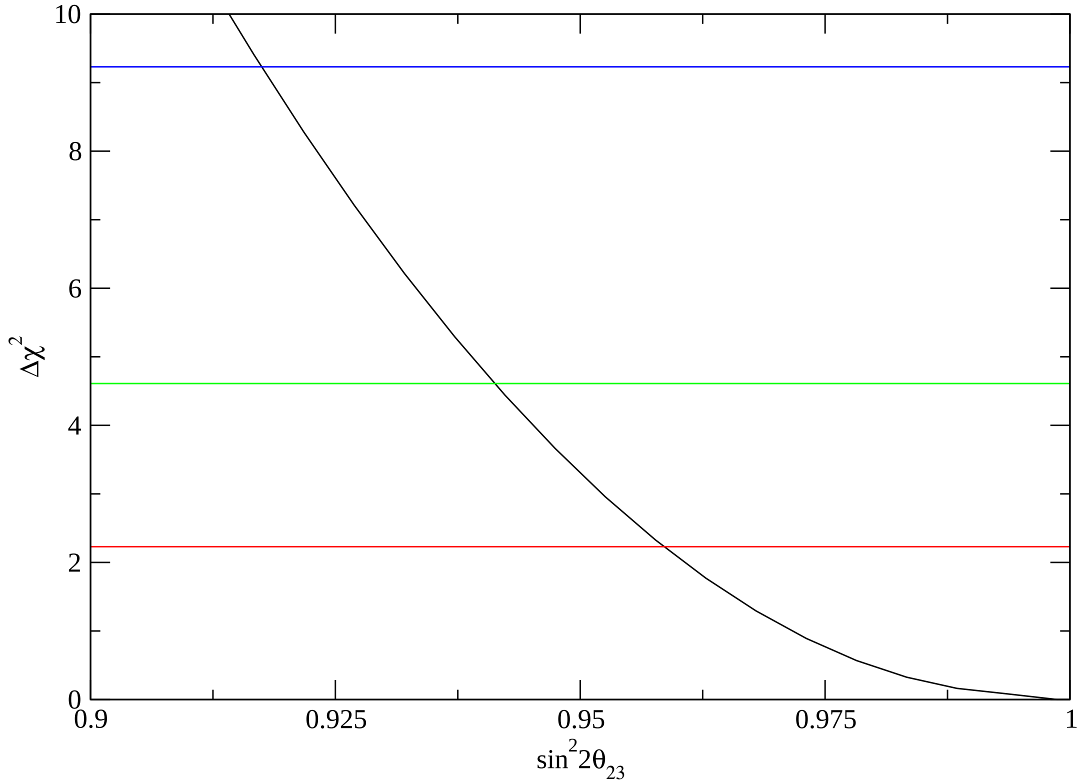

Figure 27: Super Kamiokande χ^2 vs $\sin^2 2\theta_{23}$

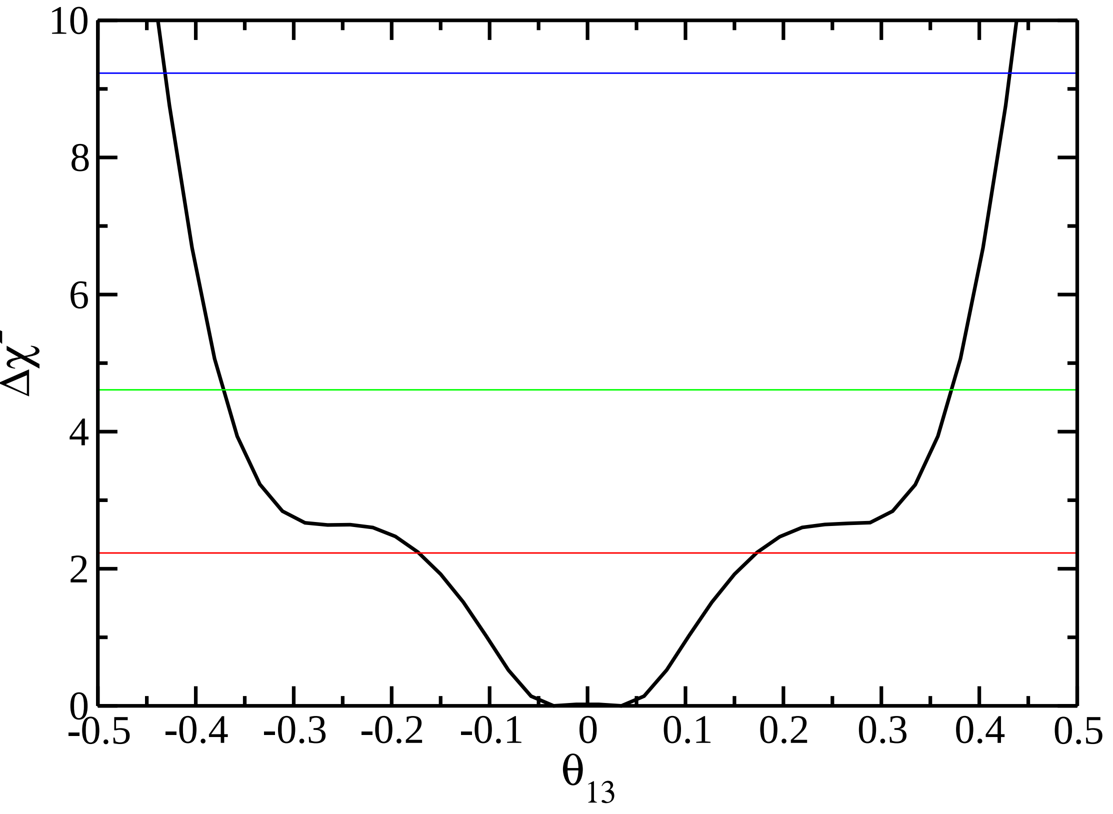

Figure 28: Super Kamiokande χ^2 vs θ_{13}

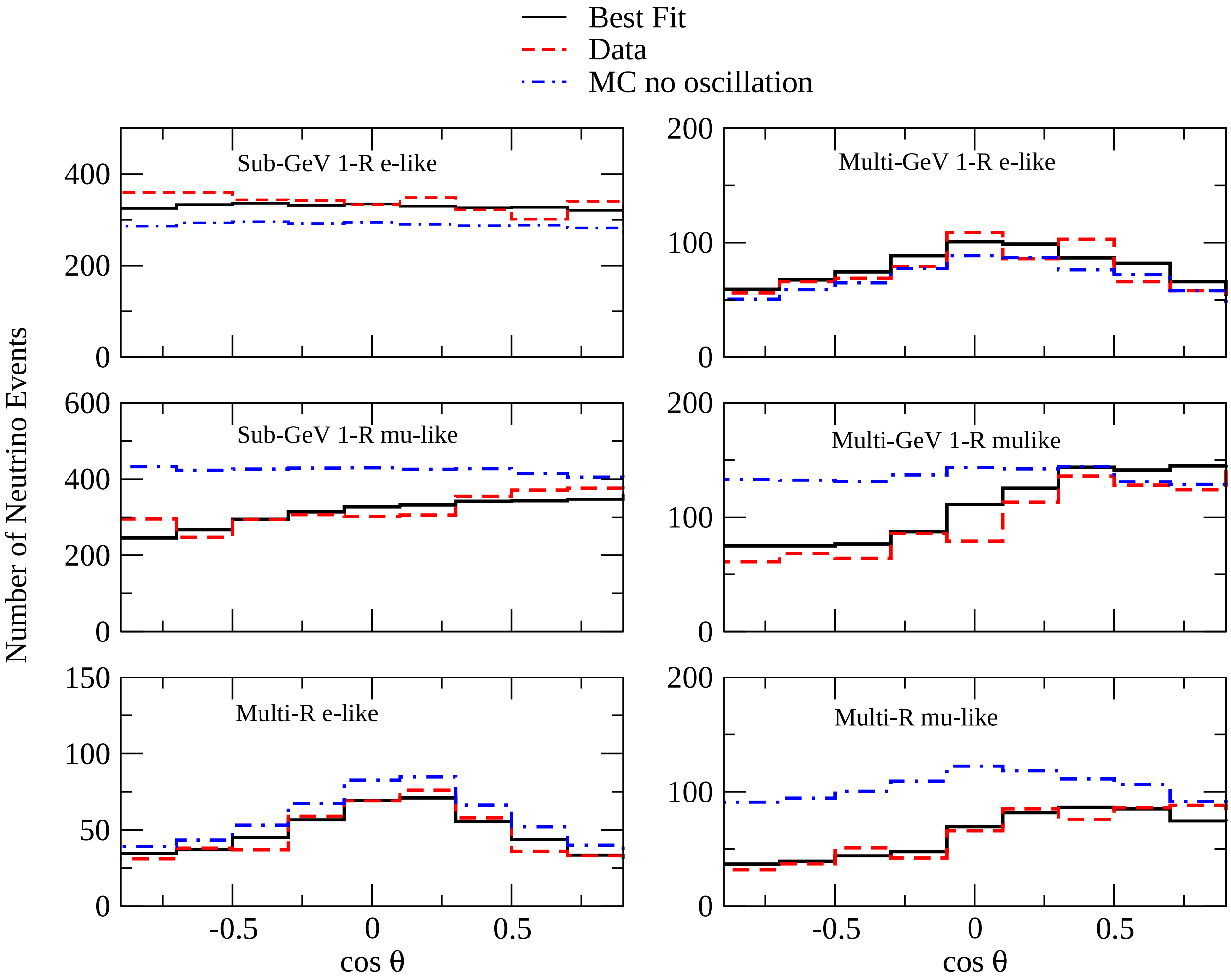

Figure 29: Super Kamiokande Neutrino Events corresponding to the best fit parameters. The tables reprecent the different experimental data samples.

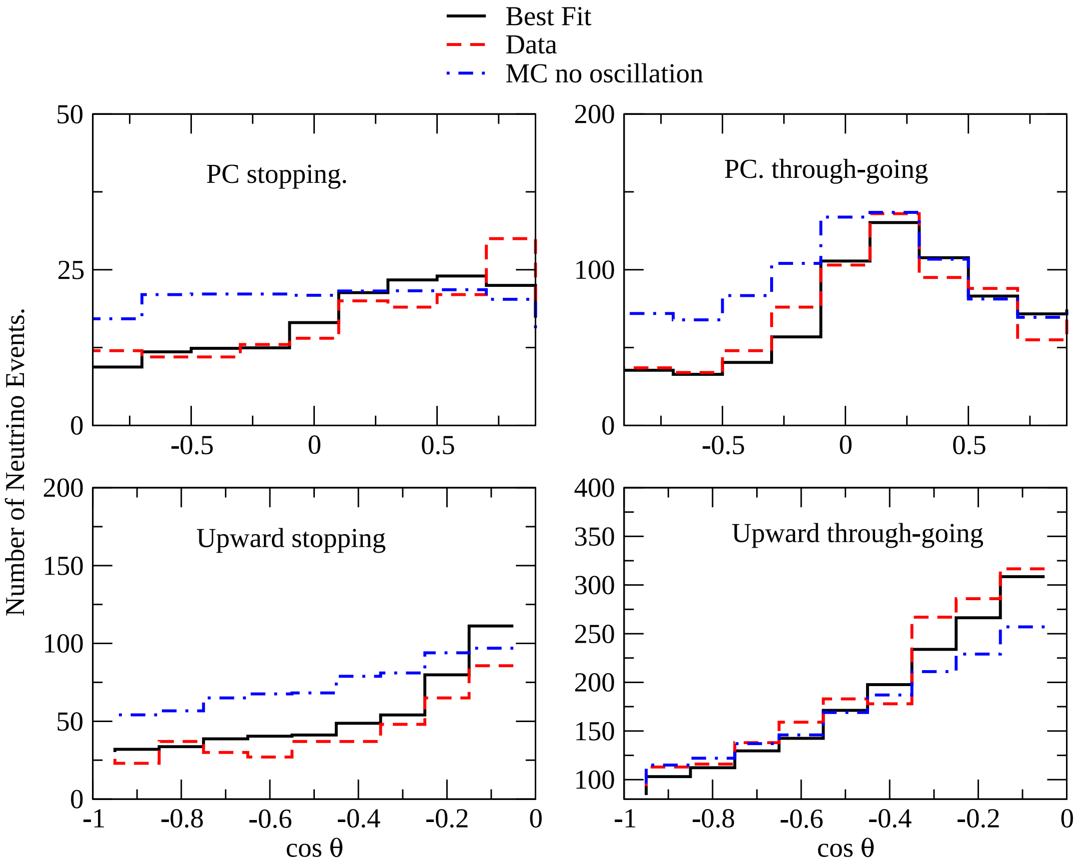

Figure 30: Super Kamiokande Neutrino Events corresponding to the best fit parameters. The tables reprecent the different experimental data samples.

Table 2: Observed number of neutrino events for the Fully Contained Single Ring (Multi-Ring) e-like and μ-like sample taken from [72]

FC single-ring e-like

E_{vis}	I	II	III	IV	V	VI	VII	VIII	IX	X
1	114	95	74	94	88	91	79	74	91	100
2	96	93	96	90	89	85	85	74	83	78
3	76	80	80	69	72	60	69	71	85	63
4	48	57	62	52	60	74	55	58	60	43
5	26	35	31	37	24	38	34	24	21	20
6	33	35	41	37	46	49	49	32	36	36
7	10	20	15	28	36	19	28	24	18	9
8	9	5	10	6	14	11	16	8	2	5
9	2	4	3	7	7	6	6	1	1	1
10	2	2	0	1	6	1	4	1	1	3

FC single-ring μ-like

E_{vis}	I	II	III	IV	V	VI	VII	VIII	IX	X
1	36	40	39	37	35	34	35	45	48	46
2	86	77	99	86	87	80	91	85	94	76
3	94	60	81	94	87	84	116	119	97	118
4	52	48	53	53	68	68	72	81	91	86
5	27	22	22	37	25	40	41	41	46	48
6	27	35	29	32	35	57	66	69	49	56
7	4	10	12	15	16	15	27	16	25	33
8∼10	3	1	1	2	3	1	2	2	4	4

FC multi-ring e-like

E_{vis}	I	II	III	IV	V	VI	VII	XII	IX	X
b	16	18	16	22	26	31	23	19	14	11
c	9	12	13	26	21	22	15	11	10	12
d	4	3	6	7	12	14	13	3	4	6
e	2	4	1	3	5	4	6	2	3	1
f	0	1	1	1	5	5	1	1	2	2

FC multi-ring μ-like

E_{vis}	I	II	III	IV	V	VI	VII	XII	IX	X
a	14	8	20	14	25	16	21	32	29	29
b	11	14	16	19	20	33	28	31	30	25
c	6	11	11	7	13	20	19	17	23	19
d∼f	1	4	4	2	8	16	8	6	6	11

Table 3: Observed number of neutrino events for the Partially Contained and Upward Going Muons sample respectively taken from [72].

PC Through-Going

E_{vis}	I	II	III	IV	V	VI	VII	XII	IX	X
a	5	9	10	9	9	9	11	10	10	7
b	4	6	10	21	18	18	12	22	11	20
c	8	6	12	15	20	48	36	27	11	18
d∼f	20	13	16	31	56	61	36	29	23	23

PC Stopping

E_{vis}	I	II	III	IV	V	VI	VII	XII	IX	X
a	5	2	2	2	1	5	5	6	9	5
b	2	2	3	4	6	2	3	5	9	5
c	4	7	3	1	2	5	7	4	4	8
d∼f	1	0	3	6	5	8	4	6	8	2

Upward Through-Going Muon

	85	113	116	138	159	183	178	267	286	316.6

Upward Stopping Muon

	28	23	37	30	27	37	37	48	65	85.7

5.1.1 Summary

The SK collaboration performed this calculation [69] and demonstrate that the atmospheric neutrino data alone helps to contrain the mixing angle θ_{13}, although not as much as does the CHOOZ experiment [27]. We simulate this calculation in order to calibrate our model. In particular we are interested in θ_{13} which is a relatively small effect. We find a similar allowed region for θ_{13} as did the SK analysis, $| \theta_{13} | < 0.38$ for $\Delta\chi^2 = 4.6$. For the same $\Delta\chi^2$ the SK collaboration also finds $1.9 \times 10^{-3} eV^2 < \Delta m^2 < 3.0 \times 10^{-3} eV^2$ and $0.93 < \sin^2 2\theta_{23}$. We find for this same $\Delta\chi^2$ the values $2.1 \times 10^{-3} eV^2 < \Delta m^2 < 3.1 \times 10^{-3} eV^2$ and $0.938 < \sin^2 2\theta_{23}$. This level of agreement assures us that our theoretical model, which is computationally efficient, is reasonably quantitative and addequate for exploring detailed physics questions. In figures 29 and 30 we compare the expected neutrino number of events corresponding to the best fit parameters, the experimental data as well as the montecarlo predictions in the absence of neutrino oscillation. In these figures we plot the zenith angular distribution of the neutrino events for the different data sample. From this plots we can

Table 4: Monte Carlo expected events assuming no neutrino oscillation for the Fully Contained Single Ring (Multi-Ring)e-like and μ-like sample taken from [72].

FC single-ring e-like

E_{vis}	I	II	III	IV	V	VI	VII	XII	IX	X
1	79.3	83.3	81.4	82.0	84.0	79.8	79.5	84.2	81.5	82.9
2	75.6	71.7	73.2	69.4	68.4	68.8	69.5	67.2	71.1	69.7
3	64.2	66.9	65.8	63.6	64.6	64.1	62.4	61.7	59.7	57.5
4	45.4	47.9	50.1	50.9	51.6	51.6	50.8	49.1	46.5	42.5
5	21.7	23.2	25.1	25.8	25.6	25.9	25.0	26.1	23.6	18.5
6	29.3	33.2	34.9	39.7	42.8	43.9	40.7	39.5	32.0	27.3
7	13.8	16.6	18.4	23.5	26.6	24.2	22.0	19.9	17.2	12.4
8	5.27	5.40	7.49	9.42	12.4	11.8	8.38	8.26	5.87	4.18
9	1.47	2.83	2.62	3.73	4.38	4.83	3.38	2.63	1.71	1.63
10	0.86	0.86	1.63	1.26	2.40	2.16	1.68	1.79	1.23	1.26

FC single-ring μ-like

E_{vis}	I	II	III	IV	V	VI	VII	XII	IX	X
1	54.7	53.7	54.4	55.1	55.8	53.8	53.5	53.6	52.6	52.1
2	124	123	123	122	119	120	123	118	116	121
3	119	112	113	116	113	113	113	112	108	105
4	91.1	88.0	90.5	91.0	94.7	91.1	89.6	88.2	84.5	82.9
5	43.4	45.9	44.9	44.5	47.0	47.5	47.9	42.6	44.0	43.6
6	58.8	57.3	59.6	61.6	62.3	63.2	64.4	59.6	55.1	54.0
7	26.1	24.9	23.8	27.3	30.7	28.3	28.6	24.6	25.3	26.8
8∼10	4.61	4.21	3.11	3.66	3.36	3.14	3.17	4.19	4.16	4.04

FC Multi-Ring e-like

E_{vis}	I	II	III	IV	V	VI	VII	XII	IX	X
b	16.9	18.1	21.2	26.9	27.8	27.6	24.0	22.1	16.8	16.0
c	13.4	14.9	18.9	22.4	28.2	28.1	22.2	17.9	14.2	12.8
d	5.77	6.40	8.44	11.3	15.1	16.0	12.4	7.28	6.20	4.77
e	2.17	2.71	2.83	5.05	7.61	8.38	5.19	3.74	1.87	2.07
f	0.89	1.11	1.68	1.75	4.00	4.70	2.33	0.98	0.89	1.21

FC Multi-Ring μ-like

E_{vis}	I	II	III	IV	V	VI	VII	XII	IX	X
a	27.6	31.2	33.4	33.7	36.1	35.6	34.1	32.9	28.9	29.1
b	33.2	33.6	36.7	39.9	43.9	43.0	40.7	40.7	33.8	32.5
c	22.4	22.8	23.5	27.5	31.6	28.8	28.0	24.8	22.4	20.4
d∼f	7.68	6.88	6.73	8.28	10.8	10.9	8.49	7.81	6.29	7.92

Table 5: Monte Carlo expected events assuming no neutrino oscillation for the Partially Contained and Upward Going Muons sample respectively taken from [72].

PC Through-Going

E_{vis}	I	II	III	IV	V	VI	VII	XII	IX	X
a	9.90	5.69	8.48	11.2	13.5	15.1	13.3	8.53	7.13	9.55
b	13.9	14.0	17.3	22.1	25.2	25.9	19.9	17.9	14.0	14.7
c	18.7	20.9	26.1	32.4	36.9	40.2	34.5	24.1	21.8	22.2
d∼f	29.4	27.2	31.5	38.4	58.2	55.6	39.1	30.7	26.5	26.2

PC Stopping

E_{vis}	I	II	III	IV	V	VI	VII	XII	IX	X
a	4.26	3.53	3.67	4.29	4.98	4.14	4.26	4.14	3.72	3.78
b	4.38	7.23	6.67	5.18	5.81	6.01	6.85	6.76	6.42	4.29
c	4.18	5.61	6.95	6.88	6.02	6.28	5.89	6.57	6.55	4.63
d∼f	4.30	4.63	3.81	4.75	4.08	5.16	4.62	4.33	3.56	2.90

Upward stopping muon

	51.2	54.1	56.7	65.0	67.6	68.2	78.9	81.0	94.0	96.9

Upward through-going muon

	96.1	115	122	137	146	169	187	211	229	257

clearly see the good agreement that exist between our best fit predictions and the experimental data, providing in this way with good evidence about the quality of our simulation.

Table 6: Summary of systematic uncertainties in the prediction of the atmospheric neutrino flux. The last column shows the error parameter numbers (j), which appeared in Eqs.59 and 61 taken from [72].

			$\sigma\,(\%)$	*No.*
(A) Systematic uncertainties in neutrino flux				
Absolute normalization			free	*1*
$(\nu_\mu + \overline{\nu}_\mu)/(\nu_e + \overline{\nu}_e)$	$E_\nu < 5\,\mathrm{GeV}$		3.0	*2*
	$E_\nu > 5\,\mathrm{GeV}$		3.0	*3*
$\nu_e/\overline{\nu}_e$	$E_\nu < 10\,\mathrm{GeV}$		5.0	*4*
	$E_\nu > 10\,\mathrm{GeV}$		5.0	*5*
$\nu_\mu/\overline{\nu}_\mu$	$E_\nu < 10\,\mathrm{GeV}$		5.0	*6*
	$E_\nu > 10\,\mathrm{GeV}$		5.0	*7*
Up/down	$< 400\,\mathrm{MeV}$	e-like	0.5	*8*
		μ-like	0.8	*8*
	$> 400\,\mathrm{MeV}$	e-like	2.1	*8*
		μ-like	1.8	*8*
	Multi-GeV	e-like	1.5	*8*
		μ-like	0.8	*8*
	PC		0.4	*8*
	Sub-GeV multi-ring μ		0.8	*8*
	Multi-GeV multi-ring μ		0.7	*8*
Horizontal/vertical[f]	$< 400\,\mathrm{MeV}$	e-like	0.3	*9*
		μ-like	0.3	*9*
	$> 400\,\mathrm{MeV}$	e-like	1.2	*9*
		μ-like	1.2	*9*
	Multi-GeV	e-like	2.8	*9*
		μ-like	1.9	*9*
	PC		1.4	*9*
	Sub-GeV multi-ring μ		1.5	*9*
	Multi-GeV multi-ring μ		1.3	*9*
K/π ratio			20.0	*10*
L_ν (production height)			10.0	*11*
Energy spectrum	$E_k < 100\,\mathrm{GeV}$		0.03	*12*
	$E_k > 100\,\mathrm{GeV}$		0.05	*12*
Sample-by-sample	FC Multi-GeV		5.0	*13*
	PC + upward stopping μ		5.0	*14*

Table 7: Summary of systematic uncertainties in neutrino interactions. The last column shows the error parameter numbers (j), which appeared in Eqs.59 and 61 taken from [72].

	σ (%)	*No.*
(B) Systematic uncertainties in neutrino interaction		
M_A in quasi-elastic and single-π	10.0	*15*
Quasi-elastic scattering (model dependence)	1.0	*16*
Quasi-elastic scattering (cross-section)	10.0	*17*
Single-meson production (cross-section)	10.0	*18*
Multi-pion production (model dependence)	1.0	*19*
Multi-pion production (total cross-section)	5.0	*20*
Coherent pion production (total cross-section)	30.0	*21*
NC/CC ratio	20.0	*22*
Nuclear effect in ^{16}O	30.0	*23*
Energy spectrum of pions	1.0	*24*
CC ν_τ interaction cross section	30.0	*25*

Table 8: Summary of systematic uncertainties in event selection. The last column shows the error parameter numbers (j), which appeared in Eqs.59 and 61 taken from [72].

			σ (%)	*No.*
(C) Systematic uncertainties in event selection				
Reduction for fully-contained event			0.2	*26*
Reduction for partially-contained event			2.6	*27*
Detection efficiency	upward stopping μ		1.3	*28*
	upward through-going μ		0.5	*28*
FC/PC separation			0.9	*29*
Hadron simulation			1.0	*30*
Non-ν	Sub-GeV	e-like	0.4	*31*
		μ-like	0.1	*32*
	Multi-GeV	e-like	0.2	*31*
		μ-like	0.1	*32*
	PC		0.2	*32*
Upward stopping/through-going μ separation			0.4	*33*

Table 9: Summary of systematic uncertainties in event reconstruction. The last column shows the error parameter numbers (j), which appeared in Eqs.59 and 61 taken from [72].

			σ (%)	*No.*
(D) Systematic uncertainties in event reconstruction				
Ring separation	< 400 MeV	e-like	6.3	*34*
		μ-like	2.4	*34*
	> 400 MeV	e-like	3.4	*34*
		μ-like	1.3	*34*
	Multi-GeV	e-like	15.9	*34*
		μ-like	6.2	*34*
	Sub-GeV multi-ring μ		3.7	*34*
	Multi-GeV multi-ring μ		7.2	*34*
Particle identification	Sub-GeV	e-like	0.6	*35*
		μ-like	0.6	*35*
	Multi-GeV	e-like	0.4	*35*
		μ-like	0.4	*35*
	Sub-GeV multi-ring μ		3.4	*36*
	Multi-GeV multi-ring μ		4.7	*36*
Energy calibration for FC event			2.0	*37*
Energy cut for upward stopping muon			1.1	*38*
Up/down symmetry of energy calibration			0.6	*39*

Table 10: Systematic Errors for Non-ν and Non-(ν_e CC) backgrounds, PC separation and multi ring normalization. The last column shows the error parameter numbers (j), which appeared in Eqs.59 and 61 taken from [72] .

		σ (%)	*No.*
(E) Sources of systematic errors for Non-ν backgrounds			
Non-ν background	upward through-going muons	3.0	*40*
	upward stopping muons	17.0	*41*
Non-(ν_e CC) background	multi-GeV single-ring e-like	14.0	*42*
	multi-GeV multi-ring e-like	20	*43*
PC stopping - PC through-going separation		12	*44*
Sample normalization of multi-GeV multi-ring e-like		free	*45*

CHAPTER VI

OTHER EXPERIMENTS IMPACTING ATMOSPHERIC NEUTRINO OSCILLATION PARAMETERS

In this chapter we describe other experiments that contrain the atmospheric oscillation parameters Δm^2, θ_{23} and the parameter θ_{13}. We probide the detail of how we model each of these experiments so that we can combine them with the SK result to study new physics. We present the description of these experiments in chronological order, starting with CHOOZ, then K2K, and finishing with the most recent, MINOS.

6.1 CHOOZ Experiment

CHOOZ is a neutrino oscillation [27] experiment located in France, utilizing two nuclear reactors as the neutrino source. The average energy of the neutrinos was 3 MeV. The detector is located approximately 1 km from the reactors giving an average $L/E \sim 300$ m/MeV. Since the source consists of nuclear reactors, the neutrino flux consists only of anti neutrinos. They are detected via the inverse beta decay reaction $\overline{\nu_e} + p \rightarrow n + e_+$ in an underground detector, see figure 31. CHOOZ collected data for a total of 8210 hours: 3420 hours with neither reactor running, 3250 hours with one reactor running, and 1540 hours with both reactors running. A total of 2991 neutrino candidates were observed during this period.

6.1.1 Oscillation Method

The data consists of seven positron energy bins for each reactor, for a total of 14 bins. We utilize a χ^2 function derived below and minimize it with respect to the neutrino oscillation parameters. In this statistical analysis we include a 14×14 covariance matrix to account for the correlation between the energy bins as indicated in [27]. We also included the systematic error from the overall normalization and for the energy calibration. For the χ^2 function we use the expected positron yield for the k-th reactor and the j-th energy spectrum bin

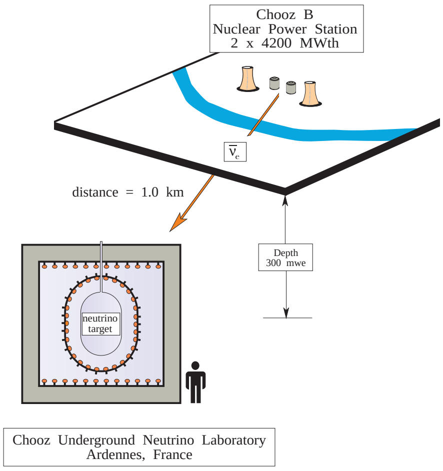

Figure 31: Overview of the CHOOZ experiment site from [27].

parameterized as

$$\overline{X}(E_j, L_k, \theta, \Delta m^2) = \tilde{X}(E_j)\overline{P}(E_j, L_k, \theta, \Delta m^2) \qquad (j = 1, \ldots, 7 \quad k = 1, 2), \tag{62}$$

where $\tilde{X}(E_j)$ is the distance-independent positron yield in the absence of neutrino oscillations, L_k is the reactor-detector distance, and the last factor represents the survival probability averaged over the energy bin and the finite detector and reactor core sizes. Here, for comparison reasons, we use the two neutrino formula used in the analysis performed by the CHOOZ collaboration.

$$P(\overline{\nu_e} \to \overline{\nu_e}) = 1 - \sin^2 2\theta \, \sin^2\left(\frac{1.27\,\Delta m^2(\mathrm{eV}^2)\,L(\mathrm{m})}{E_\nu(\mathrm{MeV})}\right). \tag{63}$$

In combination with other experiments, the full three neutrino formula will be used. The experimental yield for the 7 energy bins and the two positions L_k are given in table 11. We arrange these values into a 14-element array X arranged as follows:

$$\vec{X} = (X_1(E_1), \ldots, X_1(E_7), X_2(E_1), \ldots, X_2(E_7)), \tag{64}$$

Table 11: Experimental positron yields for both reactors (X_1 and X_2)and expected spectrum ($\tilde{X}$) for no oscillation. The errors (68% C.L.) and the covariance matrix off-diagonal elements are also listed taken from [27].

E_{e^+} MeV	$X_1 \pm \sigma_1$ (counts $d^{-1}GW^{-1}$)	$X_2 \pm \sigma_2$	$\tilde{X}$	σ_{12}
1.2	0.151 ± 0.031	0.176 ± 0.035	0.172	$-2.2\ 10^{-4}$
2.0	0.490 ± 0.039	0.510 ± 0.047	0.532	$-1.5\ 10^{-4}$
2.8	0.656 ± 0.041	0.610 ± 0.049	0.632	$-3.5\ 10^{-4}$
3.6	0.515 ± 0.036	0.528 ± 0.044	0.530	$-3.3\ 10^{-4}$
4.4	0.412 ± 0.033	0.408 ± 0.040	0.379	$-2.0\ 10^{-4}$
5.2	0.248 ± 0.030	0.231 ± 0.034	0.208	$-0.7\ 10^{-4}$
6.0	0.102 ± 0.023	0.085 ± 0.026	0.101	$-1.3\ 10^{-4}$

and similarly to define the associated covariance matrix. Combining the statistical variances with the systematic uncertainties related to the neutrino spectrum, the 14×14 covariance matrix can be written in a compact form as follows:

$$V_{ij} = \delta_{i,j}(\sigma_i^2 + \tilde{\sigma}_i^2) + (\delta_{i,j-7} + \delta_{i,j+7})\sigma_{12}^{(i)} \qquad (i, j = 1, \ldots, 14), \tag{65}$$

where σ_i are the statistical errors associated with the yield array Eq.64, $\tilde{\sigma}_i$ are the systematic uncertainties and $\sigma_{12}^{(i)}$ are the covariance of reactor 1 and 2 yield contributions to the i-th energy bin (see table. 11). We must also take into account the systematic error related to the absolute normalization; we utilize an overall normalization uncertainty of $\sigma_\alpha = 2.7\%$. In order to test for neutrino oscillation, we define the following χ^2 function as,

$$\chi^2\big(\theta, \Delta m^2, \alpha, g\big) = \sum_{i=1}^{14}\sum_{j=1}^{14}\Big(X_i - \alpha\overline{X}\big(gE_i, L_i, \theta, \Delta m^2\big)\Big)V_{ij}^{-1}$$
$$\Big(X_j - \alpha\overline{X}\big(gE_j, L_j, \theta, \Delta m^2\big)\Big) + \left(\frac{\alpha - 1}{\sigma_\alpha}\right)^2 + \left(\frac{g-1}{\sigma_g}\right)^2 \tag{66}$$

where α is the absolute normalization constant, g is the energy-scale calibration factor, $L_{i,j} = L_1$ for $i, j \leq 7$ and $L_{i,j} = L_2$ for $i, j > 7$. The result of this analysis is that at 90 %CL no evidence is found for neutrino oscillation in the $\overline{\nu_e}$ disappearance channel. This result

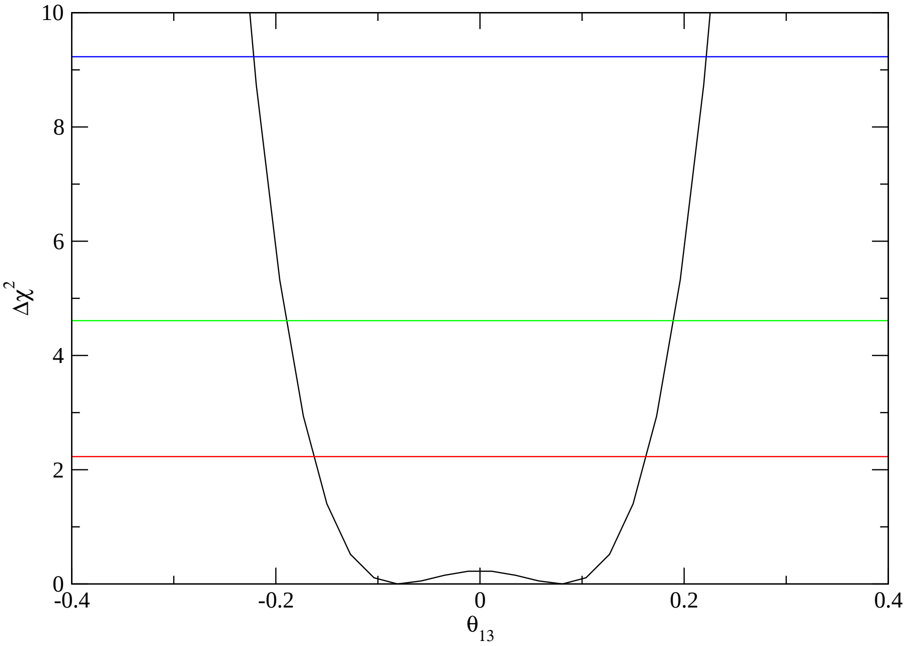

Figure 32: χ^2 vs θ_{13} curve predicted by CHOOZ experiment, fixing the other oscillation parameters to their best fit value, horizontal lines represent the 68%, 90% and 99% confidence level.

does not favor $\nu_e \to \nu_\mu$ oscillations. In figure 32 we present χ^2 versus θ_{13} for CHOOZ where we have fixed Δm^2 and θ_{23} to their best fit values from [69].

6.1.2 CHOOZ Implications

The most important consequence of the CHOOZ experiment is that it imposes an upper limit on the parameter θ_{13}. This will be more evident when we combine CHOOZ with other experiments. At 90 % CL the upper limit is $\theta_{13} < 0.19$.

6.2 K2K Experiment

The K2K neutrino oscillation experiment uses the Super Kamiokande detector. Instead of using neutrinos from the atmosphere as a source, K2K detects neutrinos produced by an accelerator at the Japanese National Accelerator Facility, KEK, located 250 km away from the SK location, see figure 33. The neutrinos produced at KEK are detected at a near detector located at a distance of 300 meters from the source. The near detector serves to

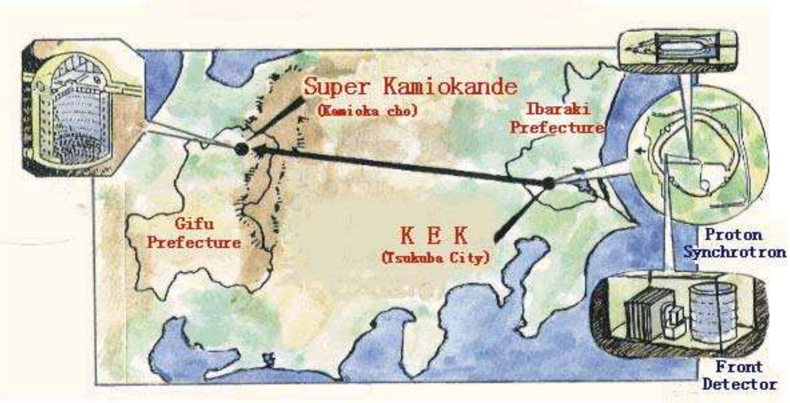

Figure 33: Overview of the K2K experiment site.

Table 12: The E_ν interval of each bin.

E_ν [GeV]	0.0–0.5	0.5–0.75	0.75–1.0	1.0–1.5	1.5–2.0	2.0–2.5	2.5–3.0	3.0–

measure the beam and its energy spectrum. The near detector used to measure the properties of the neutrino beam is made up of two main parts. The "1 kilo-ton water detector" is a small scaled down replica of the much larger 50 kilo-ton Super-Kamiokande detector. By making this detector as similar as possible to the large detector 250 kilometers away, a comparison of the properties of the neutrinos measured both close to and far away from the neutrino source can be made utilizing the same techniques. A comparison of the spectra in the near and far detector is used to test for neutrino oscillations.

The neutrino beam used in the K2K experiment is produced by a 12 GeV proton beam taken from the KEK Proton Synchrotron with fast extraction. After hitting an aluminum target the positively charged particles produced by the beam are focused by a pair of magnetic horns. These charged particles (mostly pions) then enter a long tunnel where they decay and produce neutrinos. The beam is estimated to be 99 % muon neutrino with a 1 % electron neutrino contamination. The peak energy of the resulting neutrinos is estimated to be 1 GeV and the mean energy 1.4 GeV.

6.2.1 K2K simulation method

A fundamental analysis of this experiment would start with a simulation of the expected neutrino spectrum at the far detector. This simulated spectrum would be the result of a complex Monte Carlo simulation, such as the performed by the K2K [36] collaboration that takes into account different factors and correlations between the far and near detector. This would be a very difficult task for us to do. We can use the result of the Monte Carlo simulation done by the experimentalist as the no oscillation spectrum expected on the far detector. We use the Monte Carlo data points shown in figure 34 taken from [117] for the no oscillation spectrum. The expected number of neutrino events in the presence of neutrino oscillation is then,

$$N^{theo}(n) = \int_{E_{min}(n)}^{E_{max}(n)} S(E_\nu) P_{\mu\mu}(L/E_\nu) \tag{67}$$

where $S(E_\nu)$ is the no oscillation spectrum, $P_{\mu\mu}(L/E_\nu)$ is the neutrino survival probability, $E_{max}(n)$ and $E_{min}(n)$ are the maximum and minimum energy values for the energy bin n. Table 12 gives $E_{max}(n)$ and $E_{min}(n)$ for each energy bin.

6.2.2 K2K oscillation analysis test

Similarly to the SK atmospheric experiment K2K uses single ring and multi ring data. For our analysis we use just the single ring sub-sample which consist of 58 neutrino events. A χ^2 analysis is performed based on a comparison between the observation and the model predictions. The signature for neutrino oscillations from ν_μ to ν_τ are both a reduction in the total number of observed neutrino events and a distortion in the neutrino energy spectrum. The χ^2 function is divided into two terms: the observed total number of events detected at the SK χ^2_{norm} and the shape of the spectrum included in χ^2_{shape}. We use the "pull "method to account for the systematic uncertainties by adding a third term χ^2_{syst}.

$$\chi^2_{\mathrm{K2K}} = \chi^2_{\mathrm{norm}} + \chi^2_{\mathrm{shape}} + \chi^2_{\mathrm{syst}} \tag{68}$$

The best fit oscillation parameters, Δm^2_{23} and θ_{23}, are obtained by minimizing χ^2_{tot}. The systematic parameters included in χ^2_{syst} consist of the neutrino energy spectrum at the near

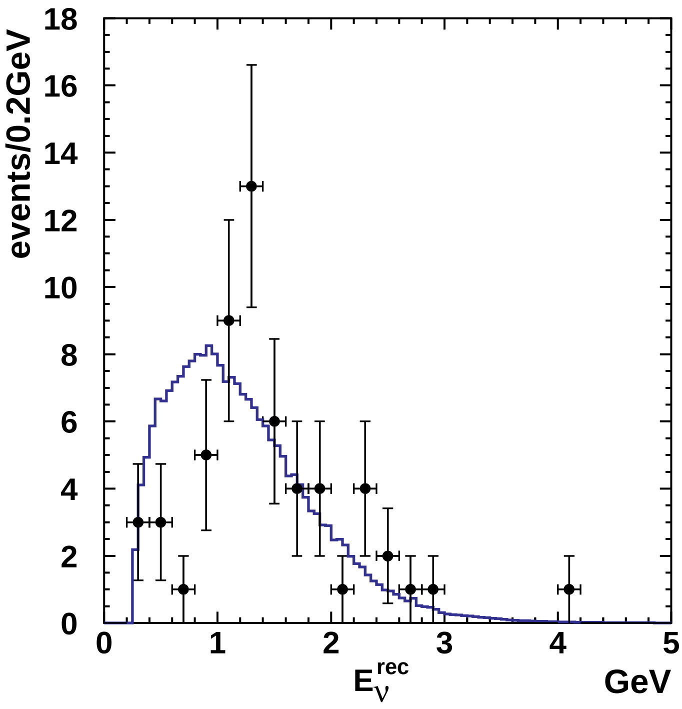

Figure 34: The reconstructed K2K E_ν distribution for the 1-ring μ-like sample. Points with error bars are data, the dashed line is the expectation without oscillation that we used as our spectrum. Taken from [117]

detector site, the flux ratio, the neutrino-nucleus cross-section, the efficiency and the energy scale of the SK detector, and the overall normalization. Due to the low statistics we use an analysis based on the Poisson distribution, hence the expressions for χ^2_{norm} , χ^2_{shape} and χ^2_{syst} are given by

$$\chi^2_{\rm shape} = 2\sum_{n=1}^{8}\left(\tilde{N}_n^{\rm theo} - N_n^{\rm data} - N_n^{\rm data}\ln\frac{\tilde{N}_n^{\rm theo}}{N_n^{\rm data}}\right), \tag{69}$$

$$\chi^2_{\rm norm} = 2\left(\tilde{N}_{\rm total}^{\rm theo} - N_{\rm total}^{\rm data} - N_{\rm total}^{\rm data}\ln\frac{\tilde{N}_{\rm total}^{\rm theo}}{N_{\rm total}^{\rm data}}\right), \tag{70}$$

with the “pull ”approach [116] accounting for the variations of the theoretical predictions due to the 31 systematic errors. Thus,

$$\tilde{N}_n^{\rm theo} = N^{\rm theo}(n) + \sum_{k=1}^{31} C_n^k \xi_k, \tag{71}$$

$$\tilde{N}_{\rm total}^{\rm theo} = \sum_{n=1}^{8}\tilde{N}_n^{\rm theo}, \tag{72}$$

$$N_{\rm total}^{\rm data} = \sum_{n=1}^{8} N_n^{\rm data}, \tag{73}$$

where $N^{\rm theo}(n)$ is given by equation 67, $N^{\rm data}$ is the experimental data provided by the K2K collaboration [117], $N_{\rm total}^{\rm data}$ and $N_{\rm total}^{\rm theo}$ are the experimental and theoretical total number of neutrino events respectively, C_n^k is the systematic error coming from the source k corresponding to the bin n, and ξ_k is the pull that accounts for the variation of the systematic k, and the data is divided into 8 energy bins.

Finally, for the $\chi^2_{\rm syst}$, we use 31 sources of systematic errors classified in different groups as follows:

$$C \equiv C(C^{\phi}, C^{\rm nonQE}, C^{\rm NC}, C^{\rm F/N}, C^{\varepsilon_{\rm SK-I}}, C^{\rm E-scale}_{\rm SK-I}, C^{\varepsilon_{\rm SK-I}}, C^{\rm E-scale}_{\rm SK-II}, C^{\rm norm}_{\rm K2K-Ia}, C^{\rm norm}_{\rm K2K-Ib}, C^{\rm norm}_{\rm K2K-II}),$$

where C^{ϕ} represents the systematic error in the energy spectrum measured by the ND, $C^{\rm nonQE}$ and $C^{\rm NC}$ are the source of errors in the cross sections, $C^{\rm F/N}$ is the error in the far/near flux

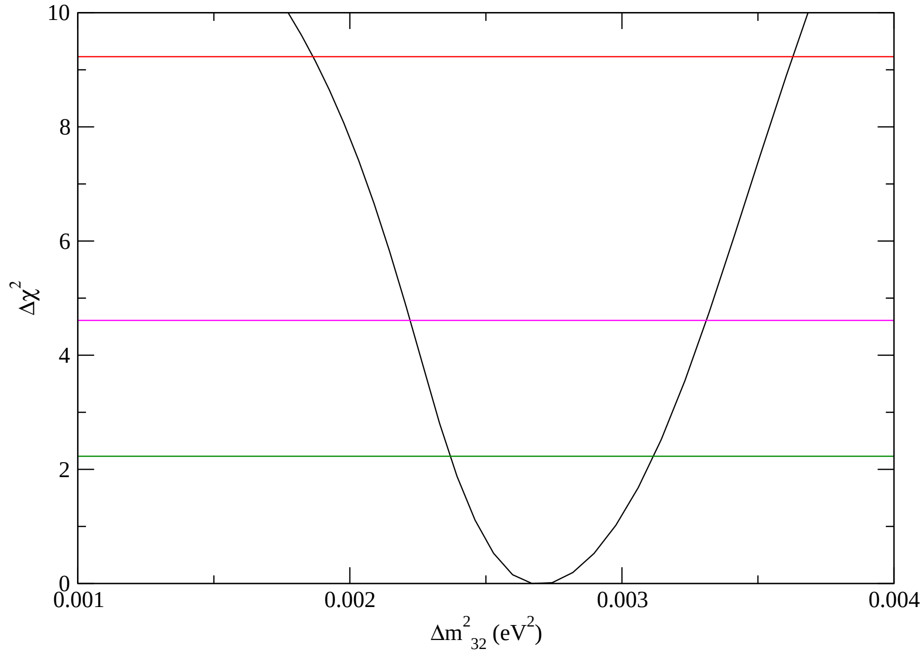

Figure 35: K2K χ^2 vs Δm^2

ratio, $C^{\varepsilon_{\mathrm{SK-X}}}$ is the systematic error in the detection efficiency at SK, $C^{\mathrm{E-scale}}_{\mathrm{SK-I}}$ is the error in the energy scale of SK and $C^{\mathrm{norm}}_{\mathrm{K2K-X}}$ is the error in the overall normalization at the K2K near detector. Table 10.1 from thesis [118] summarizes all the systematic errors for K2K as well as their estimated values. The explicit expression for χ^2_{syst} is then

$$\chi^2_{\mathrm{syst}} = \sum_{j,k=1}^{31} \xi_k (M_{kj})^{-1} \xi_i \tag{74}$$

M_{kj} is the error matrix which can be constructed from Tables 8.1 and 8.2 provided by [118] and the ξ_k's are the statistical pulls.

We minimized χ^2_{K2K} with respect to the pulls ξ_k and the oscillation parameters. The minimization with respect to the pulls is performed by the solution of 31 coupled equations as explained earlier.

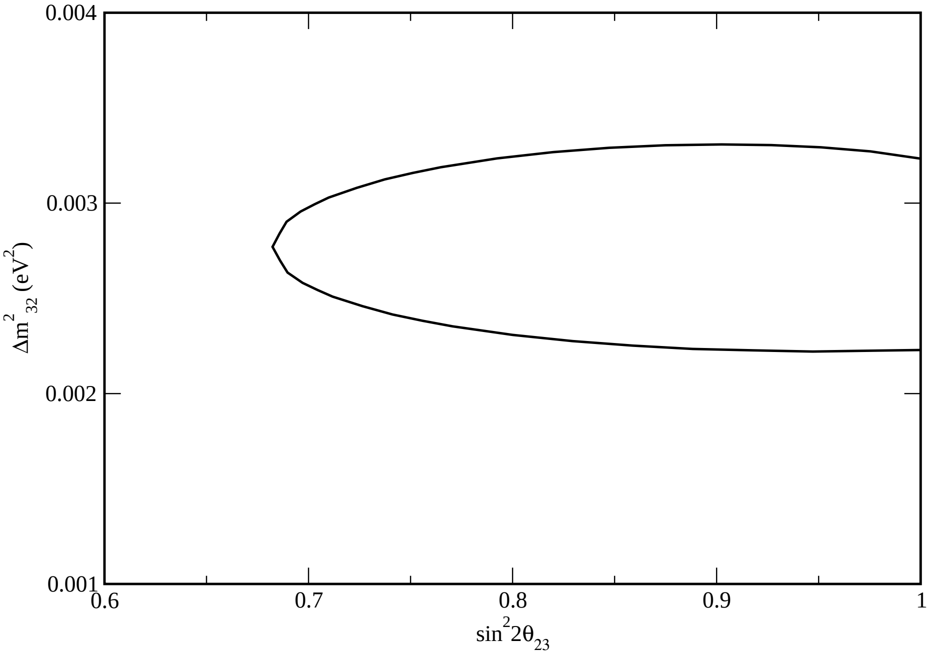

Figure 36: K2K 90% CL. Δm^2 vs $\sin^2 2\theta_{23}$ allowed region.

6.2.3 K2K results.

The statistical analysis performed in the Δm^2, $\sin^2 2\theta_{23}$ space, gives an absolute minimum χ^2 for the neutrino oscillation parameters given by $(\Delta m^2, \sin^2 2\theta_{23}) = (2.78\times10^{-3}eV^2, 0.998)$. The total number of observed events 58, is in agreement with the 56 events found from the model. We find $2.2 \times 10^{-3}eV^2 < \Delta m^2 < 3.2 \times 10^{-3}eV^2$ and at the 90 % confidence level for $\Delta\chi^2 = 2.58$. This result is consistent with the results obtained by the SK experiment for Δm^2 and $\sin^2 2\theta_{23}$, confirming in this way the hypothesis of neutrino oscillation in the atmospheric neutrino data. In figures 35 and 36 we plot χ^2 vs Δm^2 and Δm^2-$\sin^2 2\theta_{23}$ 90% CL. allowed region, respectively. These curves show the agreement the exist between our result and the result provided by the K2K collaboration [117].

6.3 MINOS Experiment

The MINOS experiment (or Main Injector Neutrino Oscillation Search) is the most recent neutrino experiment designed to study the phenomena of neutrino oscillations. This

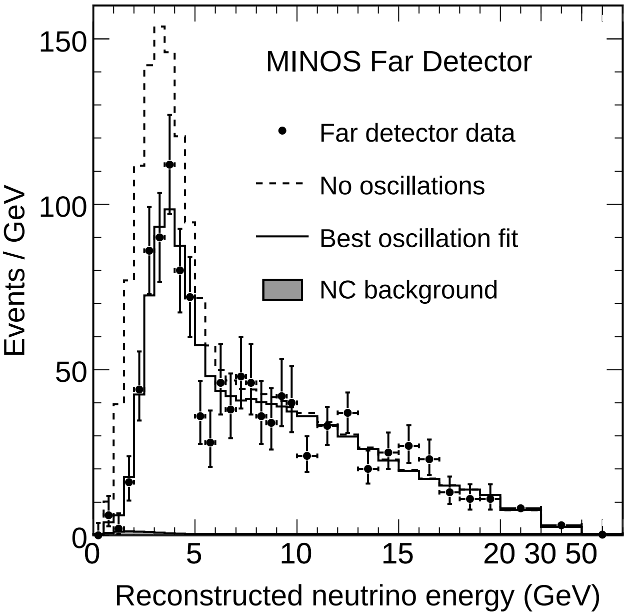

Figure 37: The reconstructed MINOS energy spectra of selected Far Detector events with the Far Detector unoscillated prediction taken from [37].

experiment very similar to the already described K2K experiment. In this case neutrinos are produced at Fermilab by the NuMI (Neutrinos at Main Injector) and then detected by two detectors, one very close to the neutrino source (the near detector ND), and another detector located 735 km away in Minnesota (the far detector FD). To produce the beam, the NuMI beam line 120 GeV Main Injector proton pulses hit a water-cooled graphite target. The resulting interactions of protons with the target material produce pions and kaons, which are focused by a system of magnetic horns. The neutrinos result from subsequent decays of pions and kaons. Most of these are muon neutrinos, with a small electron neutrino contamination. Neutrino interactions in the near detector are used to measure the initial neutrino flux and energy spectrum. The MINOS collaboration reported data [37] corresponding to two years of beam operation in which 884 ν_μ neutrino events were observed. Using observations at the near detector, in the absence of neutrino oscillations 1065 events were expected. This deficit of neutrino events is evidence of the existence of neutrino oscillation.

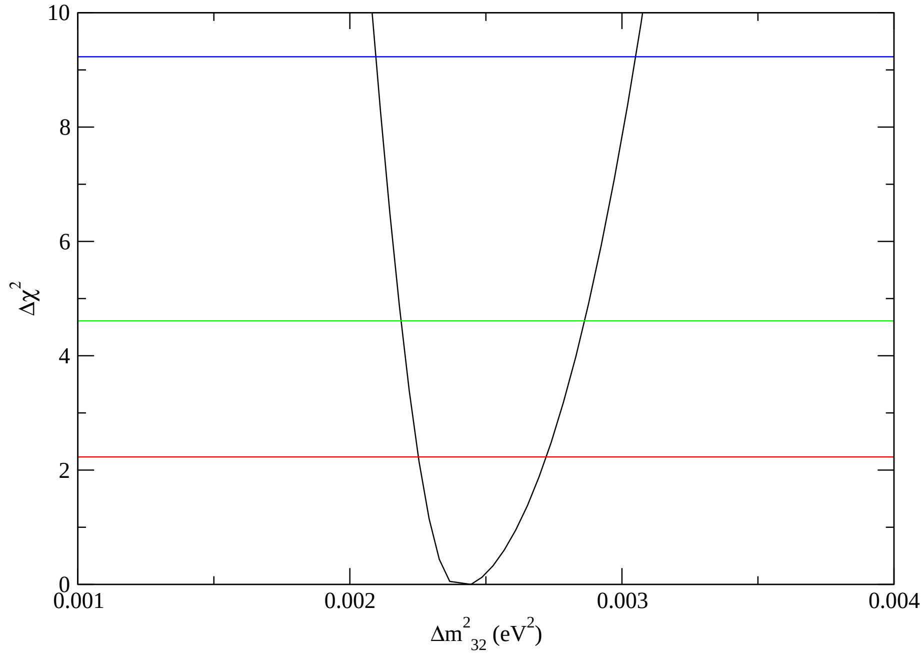

Figure 38: MINOS χ^2 vs Δm^2

6.3.1 MINOS simulation method

The procedure to simulate this experiment is very similar to the one used for the K2K experiment. The MINOS collaboration uses Monte Carlo simulations to estimate the expected neutrino spectrum at the far detector, this once again represents a great difficulty for us, given the complexity of the experiment. We use the information provided by the MINOS collaboration [37] given in figure 37. From this plot we will obtain the Monte Carlo neutrino spectrum in the absence of neutrino oscillation and then use equation 67 to calculate the expected neutrino events assuming neutrino oscillations.

6.3.2 MINOS oscillation analysis test

We again use the Poisson distribution function for our definition of χ^2 as done by the experimentalist. The data provided by the experiment [37] consist of 15 energy bins and three systematic errors; the relative normalization between the far and near detectors with a 4 % uncertainty; the absolute hadronic energy scale with a 11 % uncertainty, and a 50 %

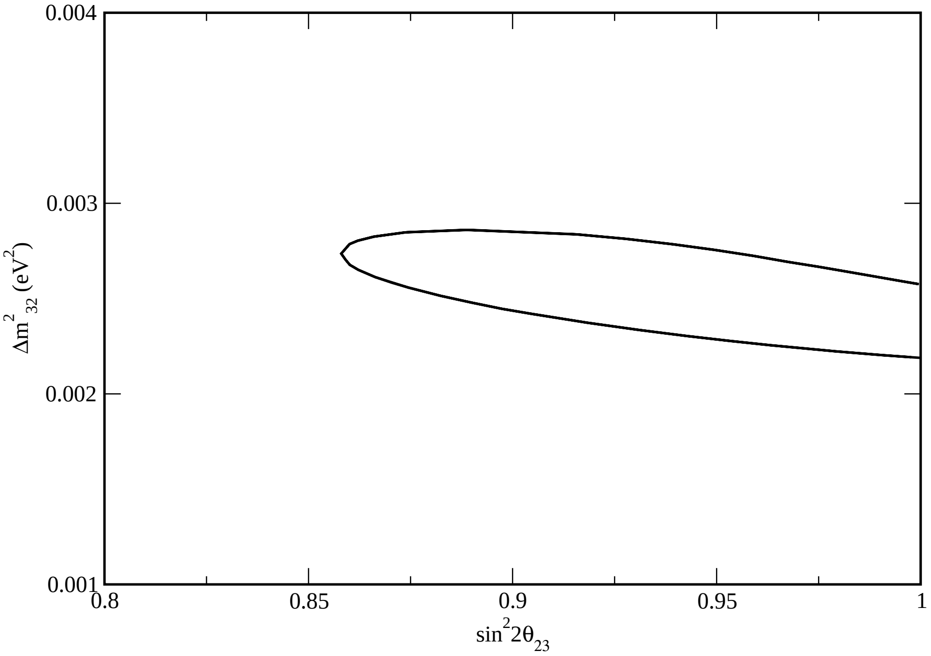

Figure 39: MINOS 90% CL. Δm^2 vs $\sin^2 2\theta_{23}$ allowed region.

uncertainty in the neutral-current background rate.The expression for the χ^2 is again given by

$$\chi^2_{\text{MINOS}} = 2\sum_{n=1}^{15}\left(\tilde{N}_n^{\text{theo}} - N_n^{\text{data}} - N_n^{\text{data}} \ln \frac{\tilde{N}_n^{\text{theo}}}{N_n^{\text{data}}}\right) + \sum_{j=1}^{3}\left(\frac{\xi_j}{\sigma_j}\right)^2, \tag{75}$$

where

$$\tilde{N}_n^{\text{theo}} = N^{\text{theo}}(n) + \sum_{j=1}^{3} C_n^k \xi_k \tag{76}$$

The meaning of these is as explained in the K2K section, and the minimization is as described for K2K.

6.3.3 MINOS results.

The analysis performed using equation 75 allows us to extract a set of oscillation parameters that minimizes χ^2_{MINOS}. The absolute minimum that corresponds to the best fit parameters is given by $\Delta m^2 = 2.41 \times 10^{-3}\text{eV}^2$ and $\sin^2 2\theta_{23} = 0.9990$. The allowed inter-

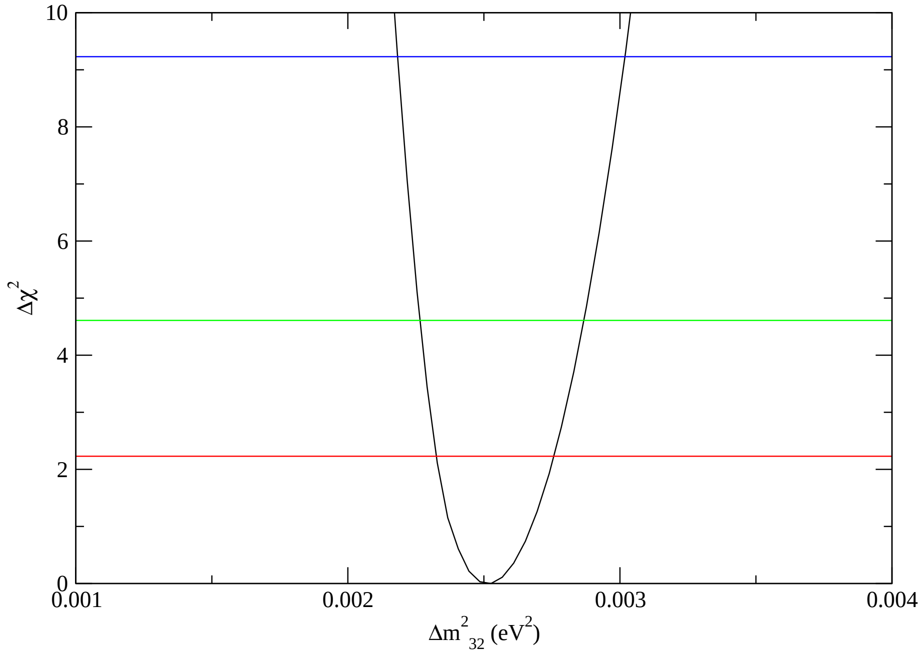

Figure 40: K2K+MINOS χ^2 vs Δm^2

vals of these parameters at 90 % C.L. are $2.25 \times 10^{-3} eV^2 < \Delta m^2 < 2.8 \times 10^{-3}\mathrm{eV}^2$ and $0.86 < \sin^2\theta_{23}$ for $\Delta\chi^2 = 4.6$. These numbers and the results shown in figure 38 and 39 are in good agreement with those given in [37], $2.2 \times 10^{-3}\mathrm{eV}^2 < \Delta m^2 < 2.7 \times 10^{-3}\mathrm{eV}^2$ and $0.85 < \sin^2\theta_{23}$, thus verifying our model.

6.4 Combined analysis of CHOOZ and long baseline experiments

The previous sections provide detailed information about the the method we used to simulate CHOOZ and the long baseline experiments, K2K and MINOS. The results that we obtained were good reproduction of the results obtained by the experimentalist themselves. Hence we can perform a combined analysis of these three neutrino experiments and study the implications and consequences that they have in determining the neutrino oscillation parameters. To do this, we need to adopt a modified version of the oscillation probability formulas that more fully takes into account the effect of all the relevant oscillation parameters for each experiment. We use here the subdominant approximation involving Δm^2, θ_{13}

and θ_{23}. Again this approximation is given by,

$$\begin{aligned}
\mathrm{P}(\nu_e \to \nu_e) &= 1 - \sin^2 2\theta_{13} \sin^2 \left(\frac{1.27 \Delta m^2 L}{E} \right) \\
\mathrm{P}(\nu_\mu \to \nu_e) &= \mathrm{P}(\nu_e \to \nu_\mu) = \sin^2 \theta_{23} \sin^2 2\theta_{13} \sin^2 \left(\frac{1.27 \Delta m^2 L}{E} \right) \\
\mathrm{P}(\nu_\mu \to \nu_\mu) &= 1 - 4\cos^2 \theta_{13} \sin^2 \theta_{23} (1 - \cos^2 \theta_{13} \sin^2 \theta_{23}) \\
&\quad \times \sin^2 \left(\frac{1.27 \Delta m^2 L}{E} \right) \qquad (77)
\end{aligned}$$

This approximation is used by the SK experimentalist and by us in chapter 5. By including the effects of θ_{13} through first order in the ratio $\alpha = \frac{\Delta m^2_{21}}{\Delta m^2_{31}}$, it goes beyond the two neutrino approximation, but is not the full three neutrino result. We call this the “2.5-flavor ”model. We start by studying the implications for the mass square difference Δm^2 when we combine the K2K and MINOS experiments. To perform this analysis we construct a χ^2 function given by $\chi^2_{\text{K2K+MINOS}} = \chi^2_{\text{K2K}} + \chi^2_{\text{MINOS}}$. Figure 40 shows $\chi^2_{\text{K2K+MINOS}}$ vs Δm^2 curve obtained by this combined analysis. As we can see, adding the two experiments reduces the size of the allowed region and moves the minimum to $\Delta m^2, \sin^2 \theta_{23} = (2.51 \times 10^{-3} eV^2, 0.980)$. For the mixing angle θ_{23}, figure 41 shows the 90% CL. allowed region, corresponding to the parameter Δm^2 and $\sin^2 2\theta_{23}$. We find a small change in the absolute minimum for the mixing angle, and a small reduction in the allowed region. Finally these two experiments have no effect on the allowed value of the angle θ_{13}. Notice that $P_{\mu\mu}$ does have a small dependence on θ_{13} through $\cos^2 \theta_{13}$ but this effect is too small in comparison to the experimental errors to even have a visible effect on the curves we are presenting. The main constraint on θ_{13} comes from the CHOOZ experiment. In figure 42 we plot $\chi^2_{\text{K2K+MINOS+CHOOZ}}$ as a function of θ_{13}, where $\chi^2_{\text{K2K+MINOS+CHOOZ}} = \chi^2_{\text{K2K}} + \chi^2_{\text{MINOS}} + \chi^2_{\text{CHOOZ}}$. Figures 42 and 32 confirm the small contribution to θ_{13} from K2K and MINOS experiment.

Discussion

The implications of this combined analysis can be seen when making a comparison of the best fit parameters with those obtained in Chapter 5 from the SK atmospheric experi-

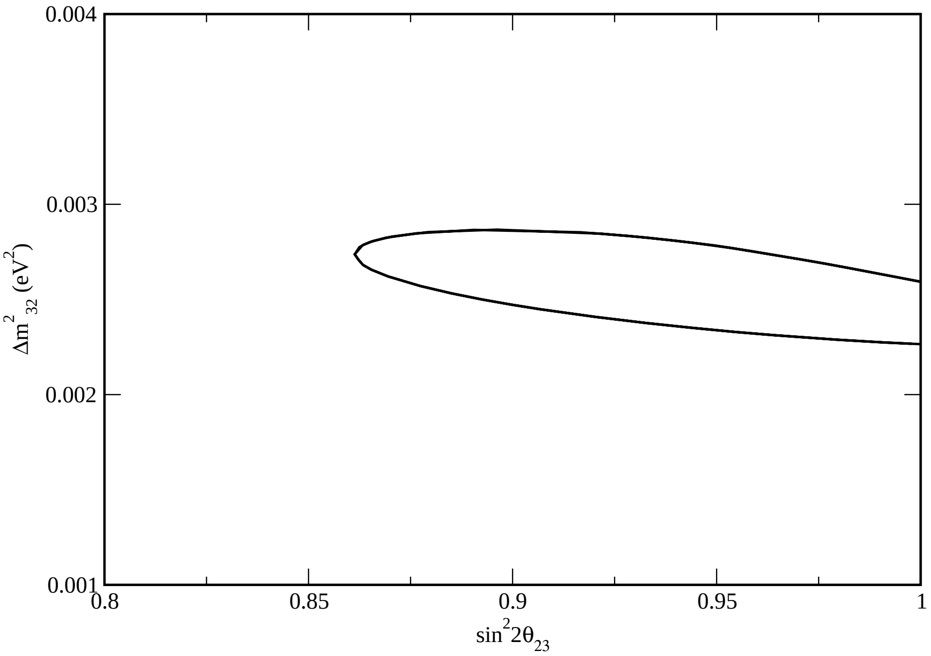

Figure 41: K2K+MINOS 90% CL. Δm^2 vs $\sin^2 2\theta_{23}$ allowed region.

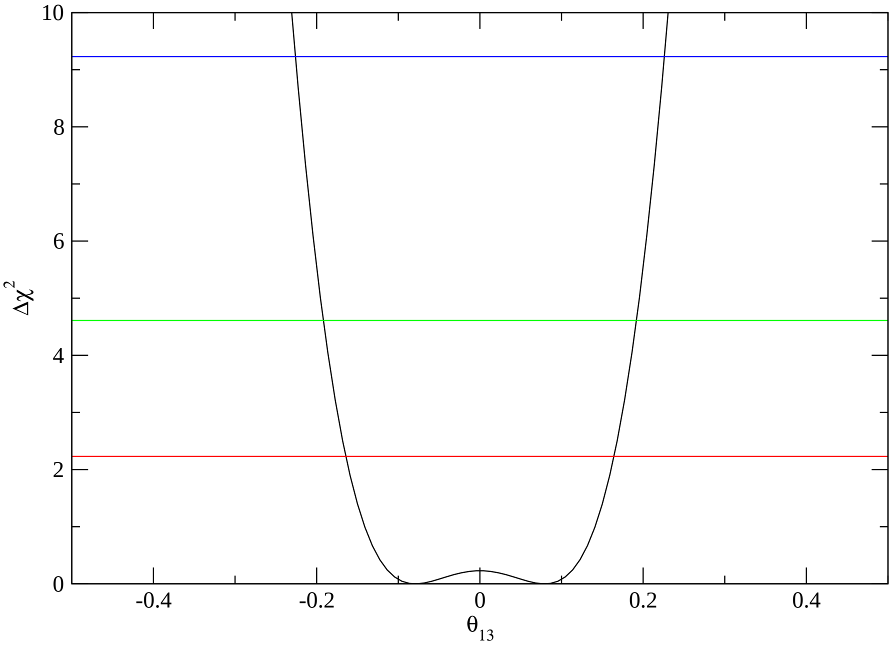

Figure 42: K2K+MINOS+CHOOZ χ^2 vs θ_{13}

ment. From Fig. 40, we can conclude that the K2K+MINOS combination provide a strong constraint for the determination of Δm^2. However, Figs. 36, 39 and 41 show that K2K and MINOS are less constraining than SK atmospheric when it comes to determining the mixing angle θ_{23}. The mixing angle θ_{13} is determined mainly by the CHOOZ experiment. Neither K2K nor MINOS, at the moment, has any effect on the determination of this parameter. SK atmospheric data does constraint θ_{13} as seen in Fig. 28. However, CHOOZ proves to be the dominant constraint in this analysis. All of these conclusions are not new. We present them to verify that our analysis is very much consistent with previous analysis in the 2.5 flavor model.

6.5 Global Analysis in the Atmospheric Neutrino Sector

We finish this chapter by showing the result of the combined analysis of all the experiments that we have described. As in previous section, we adopt the 2-5 flavor convention for the oscillation probability formulas Eqs. 77. For this analysis we construct a χ^2 function given by:

$$\chi^2_{\rm GLOBAL} = \chi^2_{\rm ATMOS} + \chi^2_{\rm K2K} + \chi^2_{\rm MINOS} + \chi^2_{\rm CHOOZ} \tag{78}$$

where each individual χ^2 has been defined in previous sections and $\chi^2_{\rm ATMOS}$ has been defined in Chapter 5. Using Eq. 78 we study the consequences of this global analysis for the determination of the oscillation parameters. We start by showing the dependence of $\chi^2_{\rm GLOBAL}$ on the mass square difference Δm^2 in Fig 43. The conclusions are what is expected from the comparison of the SK atmospheric result in Chapter 5, with the long baseline plus CHOOZ result, ie. the discussion at the end of the previous section is again verified.

We see from Figs. 42 that K2K+MINOS contributes to the determination of Δm^2, whereas SK atmospheric contributes the determination of Δm^2 and θ_{23}, and CHOOZ dominates the determination of θ_{13}, as noted earlier.

We present in Figs. 43 to 45, the χ^2 versus Δm^2, $\sin^2 2\theta_{23}$, and θ_{13} for the combined analysis, K2K, MINOS,CHOOZ and SK atmospheric for the 2.5 flavor analysis. To better understand the role of the MSW effect, we present the χ^2 versus Δm^2, $\sin^2 2\theta_{23}$, and θ_{13} for the SK

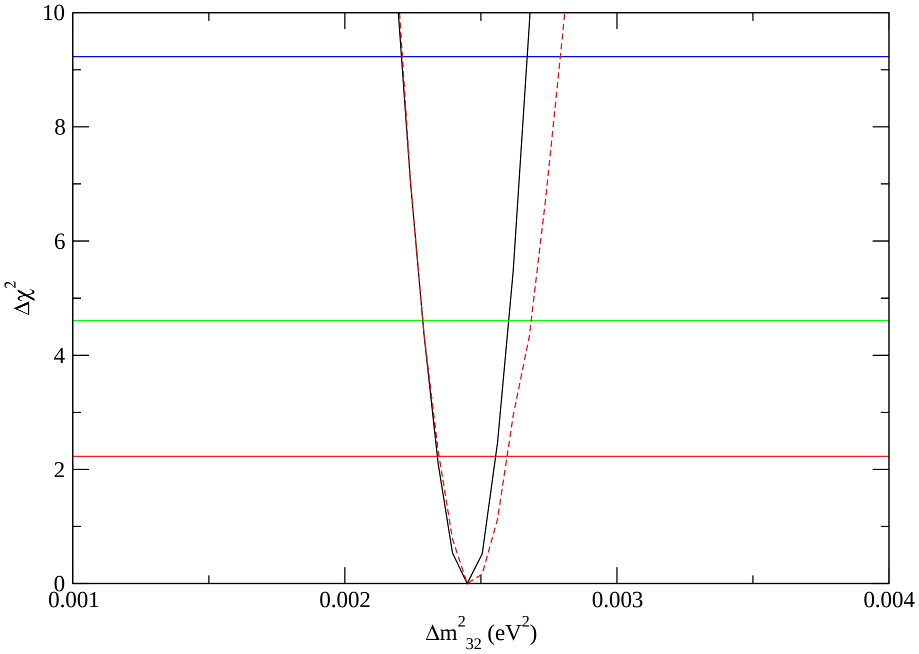

Figure 43: SK+K2K+MINOS+CHOOZ χ^2 vs Δm^2, solid and dashed lines represent the matter and vacuum case respectively.

atmospheric analysis with and without the Earth MSW effect.

We see that in the 2.5 neutrino approximation the conclusions we have reached are still valid, as the MSW effect has a small, not negligible, effect but does not alter the qualitative features of the results.

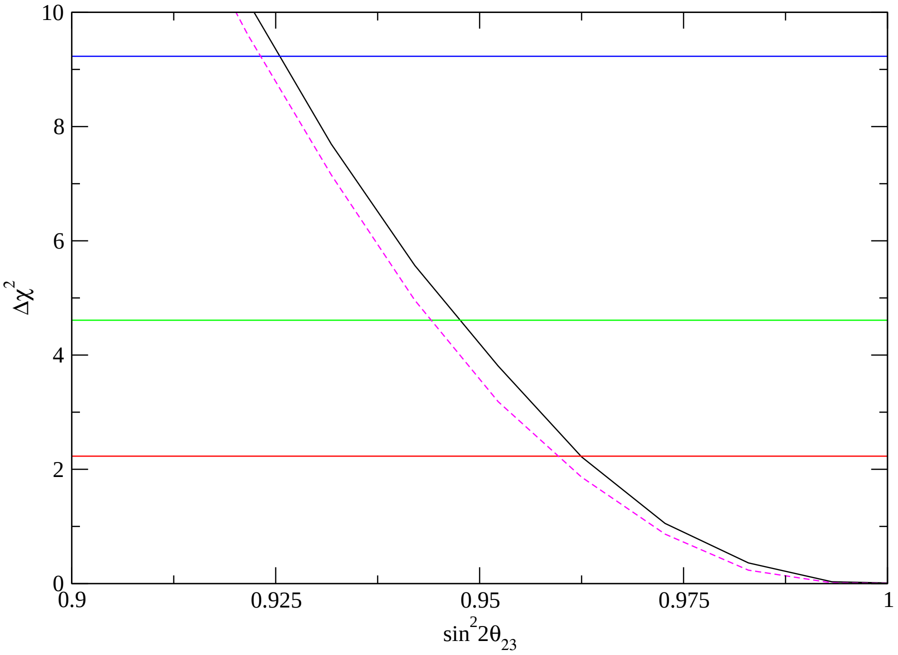

Figure 44: SK+K2K+MINOS+CHOOZ χ^2 vs $\sin^2 2\theta_{23}$, solid and dashed lines represent the matter and vacuum case respectively.

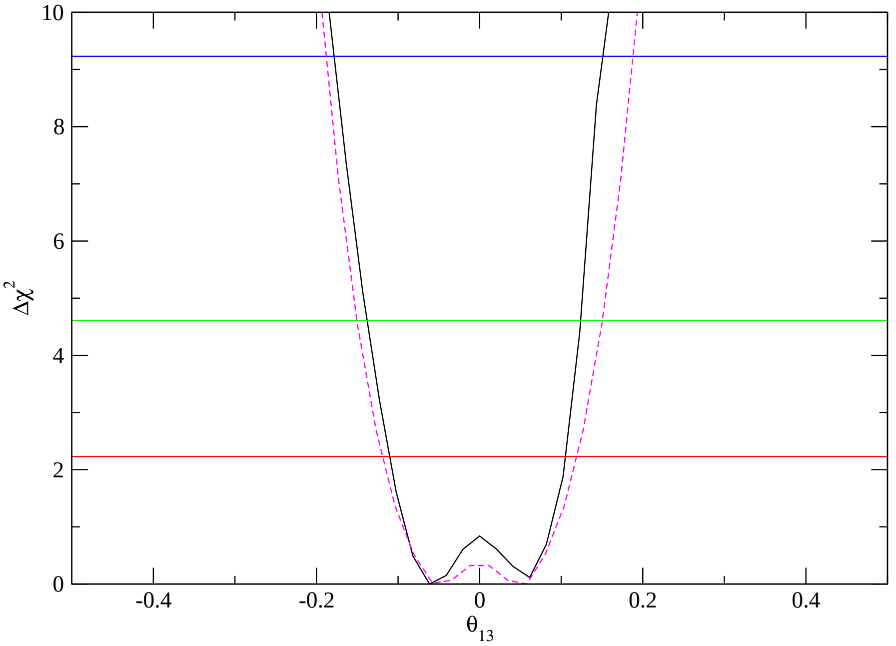

Figure 45: SK+K2K+MINOS+CHOOZ χ^2 vs θ_{13},solid and dashed lines represent the matter and vacuum case respectively.

CHAPTER VII

IMPORTANCE OF A FULL THREE NEUTRINO ANALYSIS.

This chapter studies the importance of atmospheric neutrino data in determining the oscillation parameters when a full three neutrino analysis is performed. To do this, we use the theoretical model described in previous chapters. However, unlike the analysis performed there, we use the full the full three neutrino oscillation probabilities, including matter effects, and without any approximations. We will find that there exist qualitative differences between the use of the full three neutrino probabilities and the use of the sub dominant approximation, the 2.5-flavor neutrino model. In vacuum, and in the absence of CP violation, the standard representation [51] of the mixing matrix, can be expressed in terms of the three mixing angles θ_{12}, θ_{13}, θ_{23}. The probability that a neutrino of flavor α and energy E_ν will be detected a distance L from the source as a neutrino of flavor β is then given by

$$\mathcal{P}_{\alpha\beta}(L/E_\nu) = \delta_{\alpha\beta} - 4 \sum_{\substack{k<j, \\ j,k=1}}^{3} (U_{\alpha j} U_{\alpha k} U_{\beta k}, U_{\beta j}) \sin^2 \varphi_{jk} \tag{79}$$

with $\varphi_{jk} := 1.27\,\Delta_{jk}\,L/E_\nu$, with $\Delta_{jk} = m_j^2 - m_k^2$, where L is measured in kilometers, E_ν in GeV, and the mass eigenvalues m_i in eV. Notice that there are a total of five parameters, three mixing angles, and two independent mass squared differences. Utilizing the approach developed in Ref. [114], we include the MSW effect which modifies the masses and mixing angles, of the oscillating neutrinos, changing vacuum to matter dependent quantities. We utilize a simple two density model of the earth: a mantle of density 4.5 gm/cm^3 and a core of density 11.5 gm/cm^3 and radius 3486 km. This approach allows us to efficiently incorporate the MSW effect into a three neutrino oscillation framework without approximation. All curves presented in this work include the earth's MSW effect unless otherwise specified.

7.0.1 The subdominant approximation

A common practice is to work within the "sub-dominant approximation" (or the 2.5 flavor approximation), an approximation arising from an expansion in the ratio of the mass-

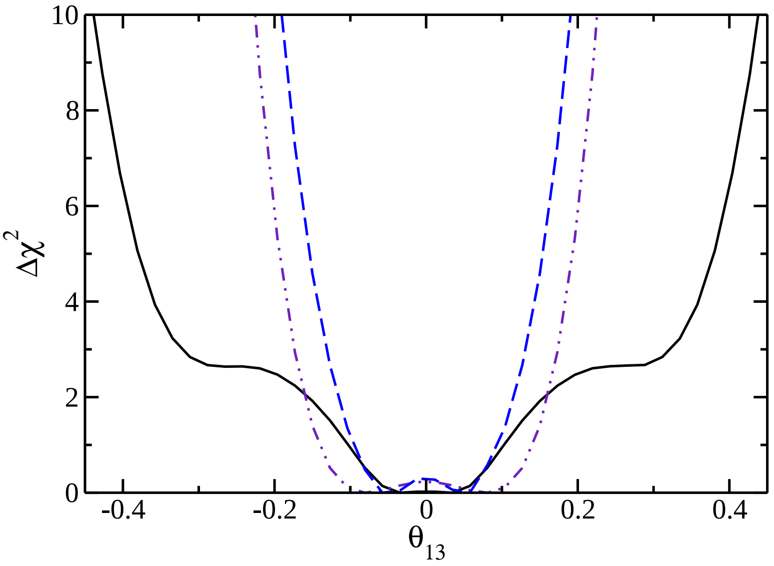

Figure 46: $\Delta\chi^2$ versus θ_{13} in the sub-dominant approximation. The solid [black] curve utilizes only atmospheric data; the dashed [blue] curve contains the LBL experiments and CHOOZ. The dot-dash [purple] curve utilizes only CHOOZ data with Δ_{32} and θ_{23} fixed.

squared differences, $\alpha \equiv \Delta m^2_{12}/\Delta m^2_{32} \approx 1/30$. This approximation uses the oscillation probabilities as expressed in Eqs. 77. Additional correction terms [109, 119] are often added to this approximation. Here we utilize the exact formula, Eq. (79).We have introduced the 2.5 neutrino approximation in order to compare our model to results found by others and to demonstrate the importance of using the full three neutrino probabilities.

7.1 The full neutrino approach.

For the full three neutrino calculation, we fix the two solar parameters at their best fit values, $\theta_{12} = 0.58$ and $\Delta m^2_{21} = 8.0\times10^{-3}\mathrm{eV}^2$. In Figs. 47 to 49, we compare the sub-dominant approximation, dashed [red] curve, with the full three-neutrino calculation, solid [blue] curve, based upon Eqs. (79). Atmospheric, long baseline (LBL), and CHOOZ data are included. In Fig 47 we present χ^2_{Global} versus the atmospheric mass square difference Δm^2_{32} for the 2.5 neutrino model and the full 3 neutrino calculation. We find that there is little effect of using the full calculation. This is not surprising as Δm^2_{32} is predominately determined by the LBL experiments. These experiments unlike the SK atmospheric experiment, do not reach into

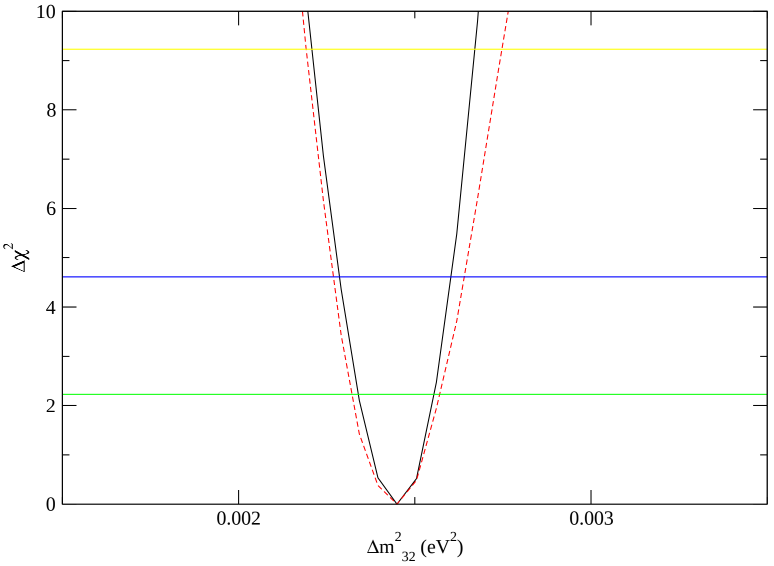

Figure 47: $\Delta\chi^2_{Global}$ versus Δm^2 for the combined analysis. Solid (dashed) line corresponds to the 2.5 flavor model (3 neutrino model)

the region, where the linear in θ_{13} terms become important and where the expansion that generates the 2.5 neutrino model is divergent.

In Fig. 48 we present χ^2_{Global} versus $\sin^2\theta_{23}$ for the 2.5 flavor model and the 3 neutrino model. Notice that the full three neutrino model is not a function of $\sin^2 2\theta_{23}$ and thus we must change to θ_{23} or $\sin^2\theta_{23}$ as independent variables. There is a larger effect of utilizing the full 3 neutrino probabilities here. This is expected as there is an approximate linear relation between θ_{23} and θ_{13} [120] with $\dfrac{d\theta_{23}}{d\theta_{13}} = \cot\theta_{12}$ in the absence of MSW effects. Since the atmospheric data reaches into the region $L/E \sim 10^4$km/GeV where linear in θ_{13} effects become significant, we expect an effect also on the value of θ_{23} as determined by the SK atmospheric data. In Fig. 49 we present χ^2_{Global} versus θ_{13} for the 2.5 neutrino model and the full 3 neutrino model.

Note that the sub-dominant results are symmetric about $\theta_{13} = 0$, as is manifest in the formulas, Eqs. (77). In Refs. [121, 120], it is shown that the neutrino oscillation probabilities were shown to contain linear (and higher order) terms in θ_{13}. The linear terms and the interference between the oscillations coming from the two different mass-squared differences have also

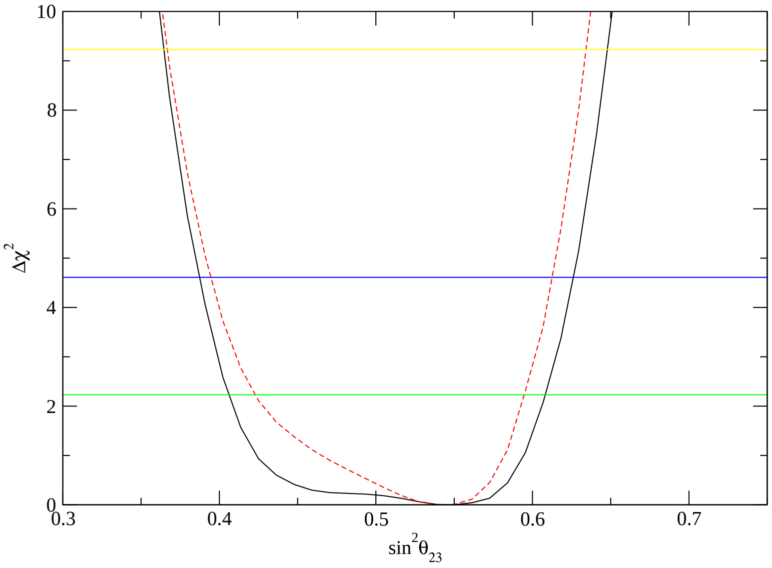

Figure 48: $\Delta\chi^2_{Global}$ versus $\sin^2\theta_{23}$ for the combined analysis. Solid (dashed) line corresponds to the 2.5 flavor model (3 neutrino model)

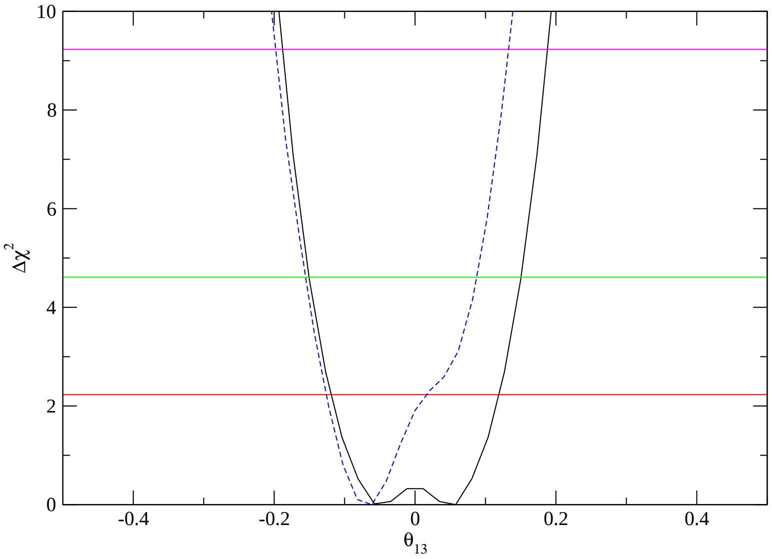

Figure 49: $\Delta\chi^2_{Global}$ versus θ_{13} for the combined analysis. Solid (dashed) line corresponds to the 2.5 flavor model (3 neutrino model)

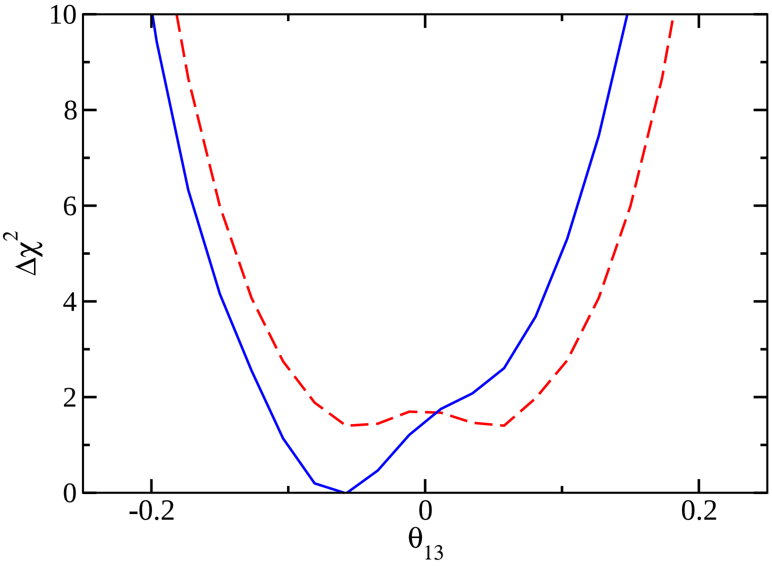

Figure 50: $\Delta\chi^2$ versus θ_{13}. The dashed [red] curve includes all data and uses the sub-dominant approximation. The solid [blue] curve incorporates the same data with a full three neutrino calculation. Here $\Delta\chi^2 = \chi^2 - \chi_0^2$ where χ_0^2 is the minimum χ^2 for the 3 neutrino analysis.

been investigated in Refs. [122, 123]. For values of $L/E_\nu \gtrsim 10^4$ km/GeV, the sub-dominant expansion was found not to be convergent and significant effects linear in θ_{13} were found, particularly at the peaks of the Δ_{21} oscillations. This region of L/E in the atmospheric data has also been noted in [124]. In Ref. [121], atmospheric oscillation data were observed to reach into this region. Fig. 50 demonstrates the truth of that statement and demonstrates that the linear in θ_{13} and higher order terms are not negligible in extracting θ_{13} from the data. Note that we have taken the bounds on the mixing angles as $\theta_{13} \in [-\pi/2, \pi/2]$ and $\theta_{12}, \theta_{23} \in [0, \pi/2]$, as first suggested in Ref. [125]. These bounds, in the absence of CP violation, produce an allowed parameter space that is a single connected region, a necessity for this work.

To further understand this result, we examine the contribution to χ^2 from the individual experiments in Fig. 51. The solid [black] curve utilizes only the atmospheric data. The atmospheric data are more restrictive than even CHOOZ for positive θ_{13}, while for negative

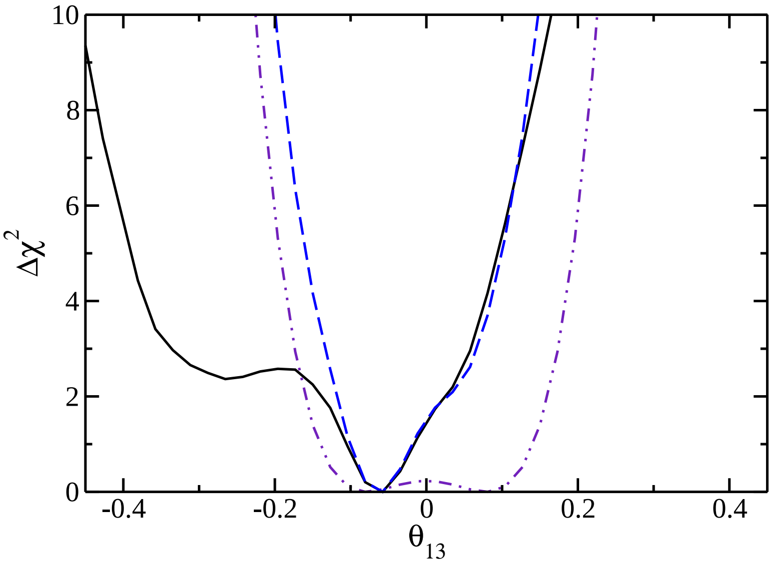

Figure 51: $\Delta\chi^2$ versus θ_{13} resulting from a full three neutrino calculation. The coding is the same as Fig. 46

θ_{13} the atmospheric data is less restrictive even than in the sub-dominant approximation. The dashed [blue] curve, the final result, adds the LBL experiments and CHOOZ. The dot-dash [purple] curve is the same as in Fig. 46. We find the allowed region for θ_{13} to be asymmetric about zero, bounded from above by atmospheric data and bounded from below by CHOOZ. The final value is $\theta_{13} = -0.07^{+0.18}_{-0.11}$, corresponding to $\Delta\chi^2 = 6.25$ for a three parameter analysis. Which subset of atmospheric data results in the strict upper bound on θ_{13} and the lack thereof from below? To answer this, we consider $\theta_{13} = 0.15$ which has $\Delta\chi^2 \sim 9$. We find that the sub-GeV fully contained events are responsible for two-thirds of this $\Delta\chi^2$. Furthermore, one-half of the total change in chi-squared (4.5) comes from the single angular bin, $-0.8 < \cos\vartheta < -0.6$, bin II, and the two lowest energy bins. This is well into the region where we expect contributions from θ_{13} linear terms. Bin I, $-1.0 < \vartheta < -0.8$, contains neutrinos which traverse the core suppressing their amplitude of oscillation.

In Fig. 52 the oscillation probabilities $\mathcal{P}_{\alpha\beta}$ are plotted as a function of E_ν^{-1}. The solid curve uses the best fit parameters, the dashed curves use $\theta_{13} = +0.15$, and the dot-dash curves $\theta_{13} = -0.15$ (if they differ from the $+0.15$ curve). For $\mathcal{P}_{ee}$, the top two curves, there is only a

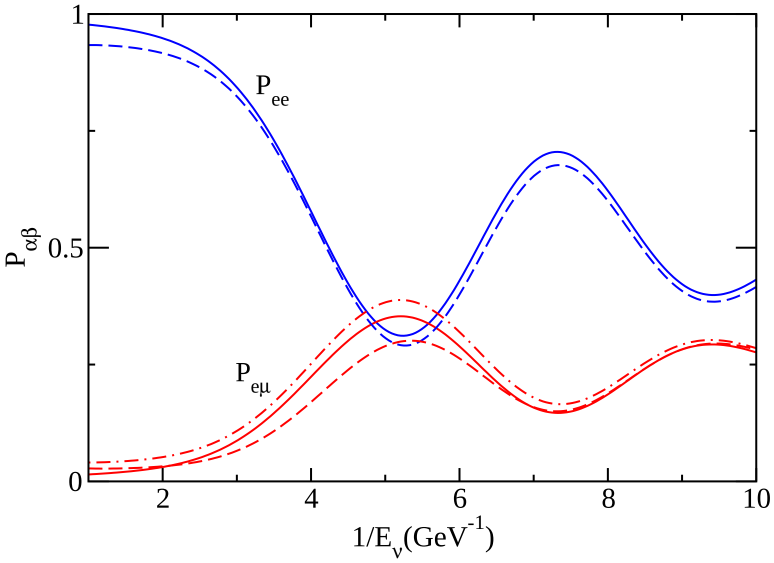

Figure 52: The oscillation probabilities $\mathcal{P}_{ee}$ and $\mathcal{P}_{e\mu}$ versus the inverse neutrino energy E_ν^{-1}. The probabilities have been averaged over the angular bin II and folded with a 6% error in the energy. The solid curves use the best fit values of the parameters. The dashed curves change θ_{13} to $+0.15$, the dot-dash curves change θ_{13} to -0.15. Note that $\mathcal{P}_{ee}$ is a function of θ_{13}^2, and the $\theta_{13} = -0.15$ curve is equal to the $+0.15$ curve.

quadratic term in θ_{13} and it lowers $\mathcal{P}_{ee}$. $\mathcal{P}_{e\mu}$ decreases (increases) with positive (negative) θ_{13}. For the expected number of e-like events in an atmospheric experiment, $R_e = \mathcal{P}_{ee} + r\mathcal{P}_{e\mu}$ with r the ratio of the ν_μ to ν_e flux, the θ_{13} effects add for positive θ_{13} and subtract for negative θ_{13}, as shown in Fig. 53. It was noted in Ref. [126] that the constancy of R_e imposes an upper bound on $|\theta_{13}|$ as well as constrains θ_{23} to be near maximal mixing. Further, the excess of e-like events at lower energies [122] results in the strict bound on positive values of θ_{13} in contrast to negative values, cf. Fig. 53. The effect is enhanced by an MSW resonance near $E_\nu = 180$ MeV for a mantle density of 4.5 gm/cm^3 and $\Delta_{21} = 8.0 \times 10^{-5}$ eV^2. In Ref. [120], it is shown that $\mathrm{d}\mathcal{P}_{e\mu}/\mathrm{d}\theta_{13}$ is proportional to $\cot 2\theta_{12}$. This relation implies the opposite sign to the linear effect for $\mathcal{P}_{e\mu}$ than is seen in Fig. 52. In matter, one must replace the mixing angle with its effective value θ_{21}^m; for $\theta_{12} = 0.58$, one has $\theta_{12}^m \approx 0.97$ at 180 MeV in the mantle giving the requisite change in sign for $\cot 2\theta_{12}^m$. Thus the bounding of θ_{13} from above by the atmospheric data depends critically on incorporating the full MSW effect.

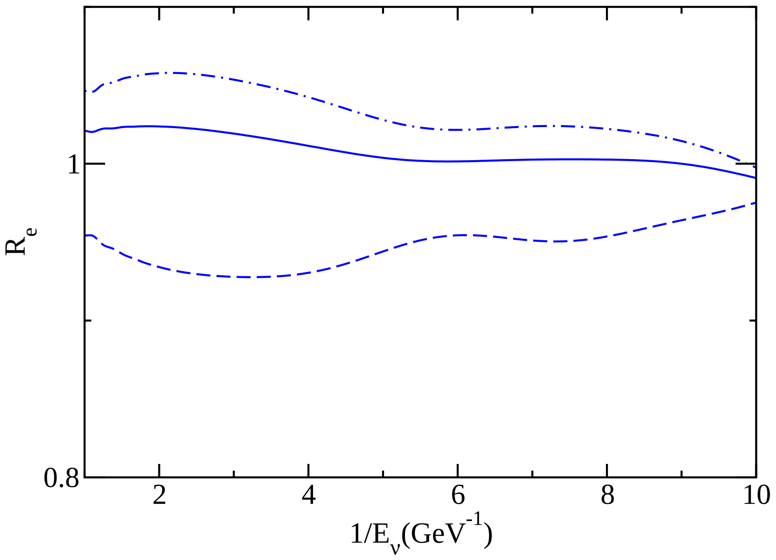

Figure 53: The measured quantity R_e versus the inverse neutrino energy E_ν^{-1}. The solid curve utilizes the best fit parameters, the dashed curve $\theta_{13} = +0.15$, the dot-dashed curve $\theta_{13} = -0.15$

7.2 MSW effect

Earlier we examined the importance of the Earth MSW effect on the SK atmospheric data, in determining the oscillation parameters in the 2.5 neutrino model. We found that the MSW effect was small and did not alter the qualitative features of the analysis. We here examine this question for the full 3 neutrino analysis. In Figs. 54, 55 and 56 we present χ^2_{Global} versus Δm^2_{32}, $\sin^2 2\theta_{23}$ and θ_{13} for the three neutrino model with and without the Earth MSW effect for the combined analysis.

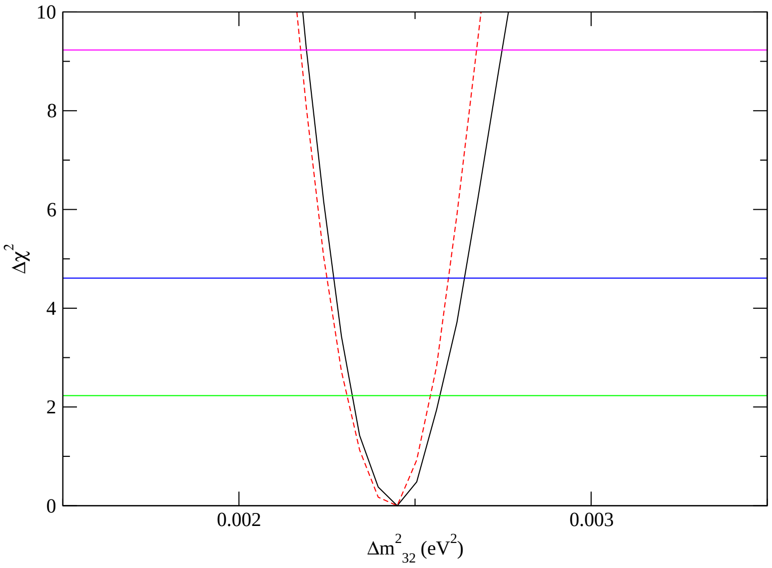

Figure 54: $\Delta\chi^2_{Global}$ versus Δm^2_{32} for the combined analysis. Solid (dashed) line corresponds to the full 3 neutrino matter case (vacuum)

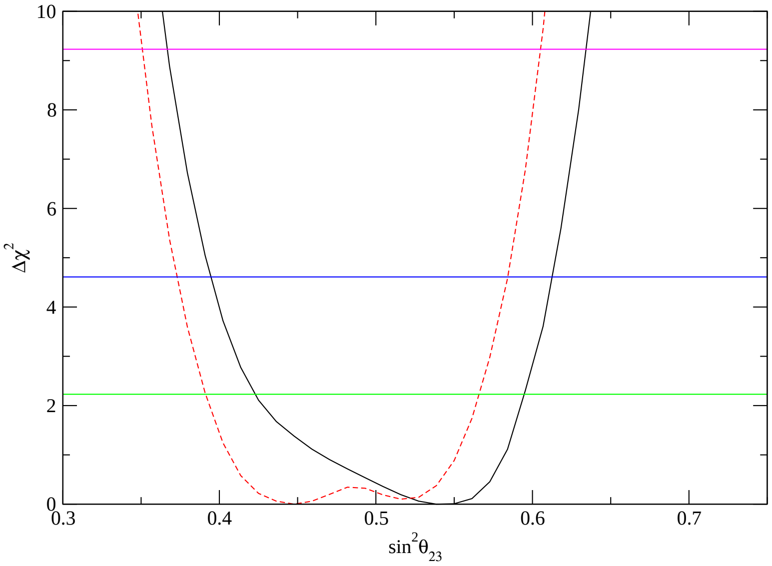

Figure 55: $\Delta\chi^2_{Global}$ versus $\sin^2\theta_{23}$ for the combined analysis. Solid (dashed) line corresponds to the full 3 neutrino matter case (vacuum)

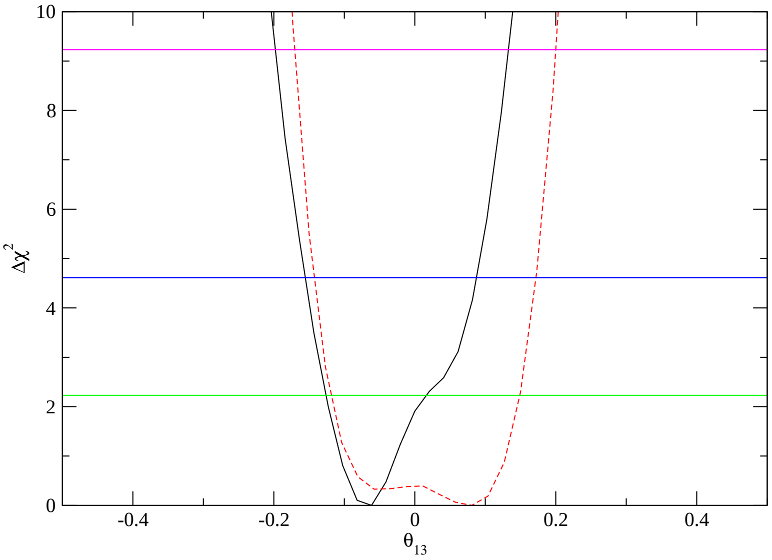

Figure 56: $\Delta\chi^2_{Global}$ versus θ_{13} for the combined analysis. Solid (dashed) line corresponds to the full 3 neutrino matter case (vacuum)

CHAPTER VIII

CONCLUSIONS

8.1 Summary of results

We have developed a computational model of the Super Kamiokande atmospheric data that is both quantitative and numerically efficient. This data is statistically the most significant data set, the one data set that covers a large variation in the important parameter L/E, and is the most difficult to analyze, both because of the complexity of the source and because the SK detector measures the angle of the particle created by the incident neutrino. To achieve our goal of computational efficiency, we utilize Monte Carlo results from the SK collaboration to replace integrals over bins by the average value of that quantity for each bin. We note that this is in the same spirit as the program provided by the Mini BooNE collaboration for the analysis of the Mini-BooNE experiment [49]. We perform an analysis in the subdominant or 2.5 flavor approximation as was done [69] by the SK experimentalists. This allows us to calibrate the accuracy of our model. We find that we are able to quantitatively reproduce those results. Particularly reproducing the results for θ_{13} is nontrivial. The effect of θ_{13} on atmospheric data is not large. Reproducing the constraints on θ_{13} means we are very close to a precise reproduction of the analysis performed by the experimentalist. We have also constructed computational models of the K2K, MINOS, and CHOOZ experiments. For these we use an approach that is the same as already put forth by others. Combining these models with the SK atmospheric model, we reproduce well existing results. The purpose of this thesis was to perform an analysis of this set of experiments using the full three neutrino oscillation probabilities. In particular, we were interested in the value of θ_{13}. Analyzes until know have been done with oscillation probabilities utilizing expansions which yield oscillation probabilities that are a function of the square of θ_{13}. The full expressions contain [121] linear in θ_{13} terms and these terms can be large [127] in the range $L/E \geq 10^4$ m/MeV. Although this value of L/E is not technically possible for an Earth bound experiment, it is reached [120] by some of the atmospheric data. We found a surprising and interesting new result. The mixing angle θ_{13} is bounded from above by the SK atmospheric data, not by CHOOZ as is found in all previous analyzes. We show how this comes about from data in the large L/E region where the subdominant expansion is not convergent. We also find that the Earth MSW effect plays a crucial role in bringing about this effect. This effect gives θ_{13} a very asymmetric error and a minimum at a (statistically insignificant) negative value. The value of θ_{13} is of particular importance as it controls both the magnitude of the CP violating effects and also the relative difference between the normal and inverted hierarchy in matter.

8.2 Future work

The immediate future is clear. Since beginning this work, new MINOS data has appeared [64]. By reducing the error in the atmospheric parameters, an analysis utilizing an expansion for the oscillation parameters [108] indicates that the new MINOS data may provide increased evidence for non-zero θ_{13}. We plan a longer paper incorporating this new data set where we explain in detail our model and expand upon the letter to examine also the role played by linear in $\epsilon = \theta_{23} - \pi/4$ terms. We have found that the relative importance of the Earth MSW effect increases when a full three neutrino model is used. We will examine this in greater detail to produce an article on the role of the Earth MSW effect. We have found that small changes, such as the incorporation of the full three neutrino oscillation probabilities, can have a relatively small effect on a small quantity such as θ_{13}. These leads to the question of what does this imply for the mass hierarchy question, a small effect, both with present data and for future experiments. Finally, SK cannot distinguish between neutrinos and anti-neutrinos. We are working on a technique to generate artificial data for the neutrinos and the anti-neutrinos separately and then utilizing this phoney data to investigate the advantages of an iron calorimeter type of detector for measuring separately atmospheric neutrinos and anti-neutrinos. The future looks most exciting. Two reactor experiments are under construction, Double CHOOZ and Daya Bay. As these are electron anti-neutrino disappearance experiments, they are sensitive only to θ_{13}^2. An upgraded SK detector is now running. How its implications and sensitivity to linear in θ_{13} terms will interplay with the reactor experiment results will be quite interesting. The field is, to some degree, on hold until we determine the magnitude of θ_{13}. This is because the next generation of experiments will address the hierarchy problem and the possible existence of CP violation and these experiments cannot be designed until we know better the size of the effects we are looking for, i.e. the size, and the sign, of θ_{13}.

REFERENCES

[1] C. D. Ellis, Proc Royal Soc **A99**, 261 (1921).

[2] L. Meitner, Phys. Zeitschr **12**, 273 (1911).

[3] E. Fermi, Z. Physik **88**, 161 (1934).

[4] C. L. Cowan, F. Reines, F. B. Harrison, H. W. Kruse, and A. D. McGuire, Science **124**, 103 (1956).

[5] G. Danby et al., Phys. Rev. Lett. **9**, 36 (1962).

[6] M. L. Perl et al., Phys. Rev. Lett. **35**, 1489 (1975).

[7] K. Kodama et al., Phys. Lett. B **504**, 218 (2001).

[8] H. R. Davis and K. C. Hoffman, Phys. Rev. Lett. **21**, 1205 (1968).

[9] K. Hirata et al., Phys. Rev. Lett. **58**, 1490 (1987).

[10] K. S. Hirata et al., Phys. Rev. D **38**, 448 (1988).

[11] R. M. Bionta et al., Phys. Rev. Lett. **58**, 1494 (1987).

[12] C. B. Bratton et al., Phys. Rev. D **37**, 3361 (1988).

[13] E. N. Alekseev, L. N. Alekseeva, V. I. Volchenko, and I. V. Krivosheina, JETP Lett. **45**, 589 (1987).

[14] C. Weinheimer et al., Phys. Lett. B **460**, 219 (1999.).

[15] K. Assamagan et al., Phys. Rev. D **53**, 6065 (1996.).

[16] J. M. Roney., Nucl. Phys. Proc. Suppl. **91**, 287292 (2001).

[17] U. Seljak et al., Physical Review D (Particles, Fields, Gravitation, and Cosmology) **71**, 103515 (2005).

[18] E. K. Akhmedov, Neutrino physics, hep-ph/0001264, 1999.

[19] T. Araki et al., Nature **436**, 499 (2005).

[20] S. M. Bilenky, W. Grimus, and H. Neufeld, Phys.Lett. B **252**, 119 (1990).

[21] S. Glashow and S. Weinberg, Phys. Rev. Lett **20**, 224 (1968).

[22] A. Salam, Nuc. Phys. **5**, 447 (1958).

[23] L. Wolfenstein, Phys. Rev. **D17**, 2369 (1978).

[24] S. P. Mikheev and A. Y. Smirnov, Sov. J. Nucl. Phys. **42**, 913 (1985).

[25] G. Zacek et al., Phys. Rev. **D34**, 2621 (1986).

[26] Y. Declais et al., Nucl. Phys. **B434**, 503 (1995).

[27] M. Apollonio et al., Phys. Lett. **B466**, 415 (1999).

[28] T. Araki et al., Phys. Rev. Lett. **94**, 081801 (2005).

[29] B. Armbruster et al., Phys. Rev. **D65**, 112001 (2002).

[30] A. Aguilar et al., Phys. Rev. **D64**, 112007 (2001).

[31] E. D. Church, K. Eitel, G. B. Mills, and M. Steidl, Phys. Rev. D **66**, 013001 (2002).

[32] N. Ushida et al., Phys. Rev. Lett. **57**, 2897 (1986).

[33] E. Eskut et al., Nucl. Phys. **B793**, 326 (2008).

[34] P. Astier et al., Phys. Lett. **B570**, 19 (2003).

[35] F. Dydak et al., Phys. Lett. **B134**, 281 (1984).

[36] E. Aliu et al., Phys. Rev. Lett. **94**, 081802 (2005).

[37] P. Adamson et al., hep-ph/0806.2237.

[38] B. T. Cleveland et al., Astrophys. J. **496**, 505 (1998).

[39] Y. Fukuda et al., Phys. Rev. Lett. **77**, 1683 (1996).

[40] J. N. Abdurashitov et al., J. Exp. Theor. Phys. **95**, 181 (2002).

[41] W. Hampel et al., Phys. Lett. **B447**, 127 (1999).

[42] M. B. Smy et al., Phys. Rev. **D69**, 011104 (2004).

[43] S. N. Ahmed et al., Phys. Rev. Lett. **92**, 181301 (2004).

[44] M. Aglietta et al., Europhys. Lett. **15**, 559 (1991).

[45] K. Daum et al., Z. Phys. **C66**, 417 (1995).

[46] S. Hatakeyama et al., Phys. Rev. Lett. **81**, 2016 (1998).

[47] W. W. M. Allison et al., Phys. Rev. **D72**, 052005 (2005).

[48] Y. Ashie et al., Phys. Rev. Lett. **93**, 101801 (2004).

[49] A. A. Aguilar-Arevalo et al., Phys. Rev. Lett. **98**, 231801 (2007).

[50] F. Boehm and P. Vogel, Cambridge University Press, 2nd edition (2003).

[51] K. Hagiwara et al., Phys. Rev. **D66**, 010001 (2002).

[52] A. Osipowicz et al., KATRIN: A next generation tritium beta decay experiment with sub-eV sensitivity for the electron neutrino mass, hep-ex/0109033, 2001.

[53] C. Weinheimer, Nucl. Phys. Proc. Suppl. **118**, 279 (2003).

[54] K. Assamagan et al., Phys. Rev. **D53**, 6065 (1996).

[55] M. Roney, Nucl.Phys.Proc.Suppl. **91**, 287 (2001).

[56] H. V. Klapdor-Kleingrothaus et al., Eur. Phys. J. **A12**, 147 (2001).

[57] S. R. Elliott and P. Vogel, Ann. Rev. Nucl. Part. Sci. **52**, 115 (2002).

[58] V. F. Hess, Phys. Z. **13**, 1804 (1912).

[59] J. A. Simpson, Ann. Rev. Nucl. Part. Sci. **33**, 323 (1983).

[60] T. K. Gaisser and T. Stanev, Phys. Rev. **D66**, 010001 (2002).

[61] T. K. Gaisser and M. Honda, Ann. Rev. Nucl. Part. Sci. **52**, 153 (2002).

[62] J. G. Learned, S. Pakvasa, and T. J. Weiler, Phys. Lett. **B207**, 79 (1988).

[63] M. Ambrosio et al., Phys. Lett. **B566**, 35 (2003).

[64] P. Adamson et al., Phys. Rev. **D77**, 072002 (2008).

[65] Y. Fukuda et al., Phys. Lett. **B388**, 397 (1996).

[66] M. Ambrosio et al., Phys. Lett. **B517**, 59 (2001).

[67] M. C. Sanchez et al., Phys. Rev. **D68**, 113004 (2003).

[68] Y. Fukuda et al., Phys. Rev. Lett. **81**, 1562 (1998).

[69] J. Hosaka et al., Phys. Rev. **D74**, 032002 (2006).

[70] S. Fukuda et al., Phys. Rev. Lett. **85**, 3999 (2000).

[71] M. Koshiba, Nuovo Cim. **C9**, 141 (1986).

[72] Y. Ashie et al., Phys. Rev. **D71**, 112005 (2005).

[73] K. Sato and H. Suzuki, Phys. Rev. Lett. **58**, 2722 (1987).

[74] M. Honda, T. Kajita, K. Kasahara, and S. Midorikawa, Phys. Rev. **D70**, 043008 (2004).

[75] W. R. Webber, Golden, R. L., and S. A. Stephens, in *20th International Cosmic Ray Conference,Moscow, USSR* , volume 1, page 325, 1987.

[76] G. Basini et al., *Ground Level Observation of Electrons, Positrons and Protons*, in *23rd Internat. Cosmic Ray Conf.* , volume 1, page 579, 1993.

[77] E. S. Seo et al., Astrophysical Journal **378**, 763 (1991).

[78] W. Menn et al., Astrophysical Journal **533**, 281 (2000).

[79] M. Boezio et al., Astrophys. J. **518**, 457 (1999).

[80] M. Boezio et al., Astropart. Phys. **19**, 583 (2003).

[81] T. Sanuki et al., Astrophys. J. **545**, 1135 (2000).

[82] J. Alcaraz et al., Phys. Lett. **B490**, 27 (2000).

[83] S. Haino et al., Phys. Lett. **B594**, 35 (2004).

[84] V. B. M. Ryan, J.F. Ormes, Phys. Rev. Lett. **28**, 985 (1972).

[85] K. Asakimori et al., The Astrophysical Journal **502**, 278 (1998).

[86] A. V. Apanasenko et al., Astroparticle Physics **16**, 13 (2001).

[87] I. Ivanenko et al., Proc. 23rd Int. Cosmic Ray Conf. **2**, 17 (1993).

[88] Y. Kawamura et al., Phys. Rev. D **40**, 729 (1989).

[89] V. Agrawal, T. K. Gaisser, P. Lipari, and T. Stanev, Phys. Rev. **D53**, 1314 (1996).

[90] M. Honda, T. Kajita, K. Kasahara, and S. Midorikawa, Phys. Rev. **D52**, 4985 (1995).

[91] G. Battistoni, A. Ferrari, T. Montaruli, and P. R. Sala, Astropart. Phys. **19**, 269 (2003).

[92] S. K. Singh and E. Oset, Phys. Rev. **C48**, 1246 (1993).

[93] C. H. Llewellyn Smith, Phys. Rept. **3**, 261 (1972).

[94] R. Gran et al., Phys. Rev. **D74**, 052002 (2006).

[95] A. V. Butkevich and S. A. Kulagin, Phys. Rev. **C76**, 045502 (2007).

[96] C. H. Albright, C. Quigg, R. E. Shrock, and J. Smith, Phys. Rev. D **14**, 1780 (1976).

[97] K. Abe et al., Phys. Rev. Lett. **56**, 1107 (1986).

[98] E. A. Paschos, L. Pasquali, and J. Y. Yu, Nucl. Phys. **B588**, 263 (2000).

[99] D. Rein, Z. Phys. **C35**, 43 (1987).

[100] D. Rein and L. M. Sehgal, Ann. of Phys. **133**, 1780 (1981).

[101] R. P. Feynman, M. Kislinger, and F. Ravndal, Phys. Rev. D **3**, 2706 (1971).

[102] M. Gluck, E. Reya, and A. Vogt, Eur. Phys. J. **C5**, 461 (1998).

[103] C. H. Albright and C. Jarlskog, Nucl. Phys. **B84**, 467 (1975).

[104] NEUGEN, http://minos.phy.tufts.edu/gallag/neugen/.

[105] E. A. Paschos and J. Y. Yu, Phys. Rev. **D65**, 033002 (2002).

[106] T. K. Gaisser, Nucl. Phys. Proc. Suppl. **87**, 145 (2000).

[107] T. K. Gaisser and T. Stanev, Phys. Rev. D **57**, 1977 (1998).

[108] G. L. Fogli, E. Lisi, A. Marrone, and A. Palazzo, Prog. Part. Nucl. Phys. **57**, 742 (2006).

[109] M. C. Gonzalez-Garcia and M. Maltoni, Phys. Rept. **460**, 1 (2008).

[110] M. Ishitsuka, PhD Thesis, University of Tokyo (2004).

[111] M. D. Messier, PhD Thesis, Boston University (1999).

[112] R. M. Sternheimer and R. F. Peierls, Phys. Rev. **B3**, 3681 (1971).

[113] R. K. W. Lohmann and R. Voss, CERN (1985).

[114] T. Ohlsson and H. Snellman, Phys. Lett. **B474**, 153 (2000).

[115] V. Barger, K. Whisnant, S. Pakvasa, and R. J. N. Phillips, Phys. Rev. D **22**, 2718 (1980).

[116] G. L. Fogli, E. Lisi, A. Marrone, D. Montanino, and A. Palazzo, Phys. Rev. D **66**, 053010 (2002).

[117] M. H. Ahn et al., Phys. Rev. **D74**, 072003 (2006).

[118] M. Hasegawa, PhD Thesis, Kyoto University, (January 2006).

[119] E. K. Akhmedov, R. Johansson, M. Lindner, T. Ohlsson, and T. Schwetz, JHEP **04**, 078 (2004).

[120] D. C. Latimer and D. J. Ernst, Phys. Rev. **C72**, 045502 (2005).

[121] D. C. Latimer and D. J. Ernst, Phys. Rev. **C71**, 062501 (2005).

[122] O. L. G. Peres and A. Y. Smirnov, Nucl. Phys. **B680**, 479 (2004).

[123] S. Choubey and P. Roy, Phys. Rev. **D73**, 013006 (2006).

[124] R. Gandhi, P. Ghoshal, S. Goswami, and S. U. Sankar, hep-ph/0805.3474, 2008.

[125] D. C. Latimer and D. J. Ernst, Phys. Rev. **D71**, 017301 (2005).

[126] D. V. Ahluwalia, Mod. Phys. Lett. **A13**, 2249 (1998).

[127] J. Escamilla, D. C. Latimer, and D. J. Ernst, (2008).